A STUDY OF THE GEOSPACE RESPONSE TO DYNAMIC SOLAR WIND USING THE LYON-FEDDER-MOBARRY GLOBAL MHD SIMULATION

by

RICHARD EDWARD FREDERICK BONDE

Presented to the Faculty of the Graduate School of

The University of Texas at Arlington in Partial Fulfillment

of the Requirements

for the Degree of

DOCTOR OF PHILOSOPHY

THE UNIVERSITY OF TEXAS AT ARLINGTON

May 2018

Acknowledgements

First and foremost, I wish to thank my supervising professor, Ramon E. Lopez. It has been an honor and a privilege to work with him and be introduced to the broader space physics community. The amount of knowledge I have attained has been incredible. My only regret is that I wasn't with the group longer.

I wish to express my gratitude to my dissertation committee: Alex Weiss, Yue Deng, Zdzislaw Musielak, and Wei Chen. I appreciate the opportunity to share my research with them and the helpful discussions that followed.

I would like to also thank the following people: Robert Bruntz and Mike Wiltberger for their helpful discussions; Jiangyan Wang for her help and discussions during her time at UT Arlington – it was an honor to work with you; and a special thanks goes to Kevin Pham for all of his help and support through my endless questions. I appreciate it.

It has been great experience to work with undergraduates on their research during my time here. I would like to acknowledge their hard work. Our magnetopause group did well and I appreciate it.

The funding for this research was supported by NASA grant NNX15AJ03G. I also wish to thank the Texas Space Grant Consortium for awarding me a fellowship that supported my work.

OMNI solar wind data was provided by J.H. King and N. Papatashvilli (AdnetSystems, NASA GSFC) through CDAWeb. THEMIS FGM data was provided by V. Angelopoulos, U. Auster, and K.H. Glassmeier & W. Baumjohann (UCB, TUBS, & IWF) through CDAWeb (NASA NAS5-02099). THEMIS orbit information was provided by NASA SSC.

My path in physics started with my undergraduate thesis advisor at Wichita State University, Professor Elizabeth Behrman. Thank you for allowing me the opportunity to do research with you and your encouragement to go to graduate school.

I wish to thank my family and friends who supported me along the way, especially Sarah Young. Your encouragement and late night discussions helped me more than you could know.

Finally, I wish to thank my parents. To my mother, who sacrificed everything so that I may have every opportunity to do what I wanted to do. I'm sorry that you couldn't be here to see this. And to my father for his unwavering support in everything I do. I am so proud that you decided to go back and get a Bachelor of Arts in history. It is an honor to graduate the same day as you.

April 25, 2018

Abstract

A STUDY OF THE GEOSPACE RESPONSE TO DYNAMIC SOLAR WIND USING THE LYON-FEDDER-MOBARRY GLOBAL MHD SIMULATION

Richard Bonde, PhD

The University of Texas at Arlington, 2018

Supervising Professor: Ramon E. Lopez

As the wind from the Sun advances towards Earth, it interacts with Earth's magnetic field. This solar wind carries with it a magnetic field, called the interplanetary magnetic field (IMF). Energy and momentum are transferred from the solar wind to the geospace environment through two mechanisms: magnetic reconnection between the IMF and Earth's magnetic field and a viscous-like interaction. While magnetic reconnection is the dominant mechanism, there are times when the viscous interaction has a significant contribution. Previous studies using magnetohydrodynamic (MHD) simulations to study the viscous interaction have done so using steady state solar wind conditions. The solar wind is highly dynamic and can have considerable changes on the order of minutes. We use the Lyon-Fedder-Mobarry global MHD simulation to test the effect the viscous interaction has on the transpolar potential (TPP) with solar wind velocity fluctuations. The TPP is used as a proxy for the amount of coupling between the solar wind and Earth's magnetosphere. While fluctuations in the equatorial plane seem to have little or no effect on the TPP, fluctuations in the meridional plane cause variations in the TPP, even creating an asymmetry between the hemispheres. The response the TPP was proportional to the amplitude of the velocity oscillation but appears not to be affected by the frequency of oscillation. There is also a strong flow asymmetry in the

magnetotail, which is flapping like a wind sock, in response to these solar wind variations. This creates a large sunward flow in one of the two tail lobes. The effect of solar wind fluctuations can also be tested on the response to the dayside magnetopause. The dayside magnetopause position, regarded as a critical space weather metric, is of great importance to satellite operators. Large-scale fluctuations in the solar wind can compress the magnetopause inward over satellites, exposing them to the hazardous conditions in the magnetosheath. Again, previous studies on the magnetopause position were conducted with steady state solar wind conditions. We ran LFM to gauge the response of the subsolar magnetopause during conditions similar to a high-speed stream (HSS), where there are large Alfvénic fluctuations and the dynamic pressure is relatively constant. The dayside magnetopause responds to these IMF variations in a type of "breathing" mode. The subsolar magnetopause exhibits a hysteresis-like effect, having a roughly constant response time to an IMF perturbation with constantly changing IMF conditions. In certain situations, the subsolar magnetopause position never relaxes to steady state values. This shows that when running MHD simulations, the time history of the solar wind must be taken into account. A HSS from 14-19 September, 2017 was simulated in LFM to see the response of the dayside magnetopause. To verify the actual position of the dayside magnetopause during this event, a series of THEMIS magnetopause crossings were used. The THEMIS crossings, along with the LFM results, were compared to empirical models of the magnetopause. These empirical models use instantaneous solar wind parameters to predict the position of the magnetopause and at times were predicted to over 1 R_E from the actual magnetopause position. The work presented in this dissertation shows that to improve the accuracy of empirical models, the time history of the solar wind cannot be overlooked.

Table of Contents

List of Illustrations

List of Tables

Chapter 1

Introduction

1.1 The Sun

By galactic and universal standards, the Sun is extremely ordinary. It is middle-aged: about 5 billion years old (with roughly a 10 billion year lifespan). It is relatively small and cool compared to the immense number of stars in the universe. To most people, the Sun is an unchanging object that treks across the sky each day giving us light and warmth. In reality, the Sun is a lively, giant ball of plasma that has a tremendous effect on everything in the solar system.

1.1.1 Anatomy of the Sun

The source of the Sun's power starts at the inner core where hydrogen is converted to helium through nuclear fusion. The core heats up to over 15 million Kelvin (27 million degrees Fahrenheit) [Ryden & Peterson, 2010]. This process releases an incredible amount of energy every second. This energy is transported through the rest of the interior of the Sun: the radiative and convective zones. The interior structure of the Sun is shown in figure 1-1.

The Sun, being in a plasma state, has no hard surface. The "surface" of the Sun refers to the photosphere – the visible surface. It is the deepest layer of the Sun we can see. It is more of a transition layer than a surface. The photosphere has a temperature of 6 000 Kelvin, is 400 km thick, and is the layer of the Sun's atmosphere in which nearly all observed photons escape [Ryden & Peterson, 2010]. One solar radius is defined to be R_S = 696 000 km and is the distance from the center of the Sun to the base of the photosphere [Ryden & Peterson, 2010].

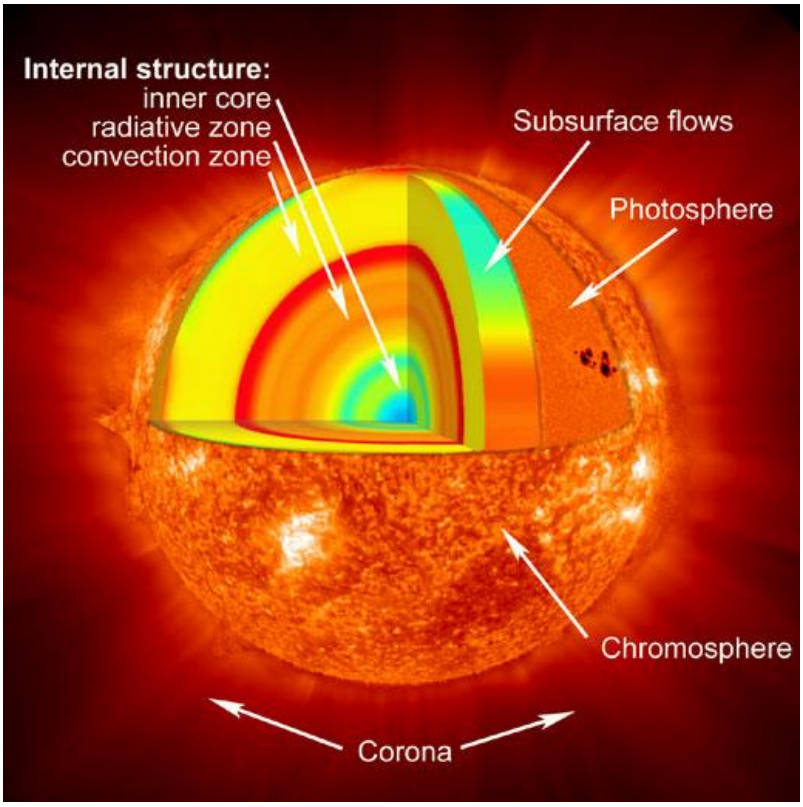

Figure 1-1 The anatomy of the Sun [NASA].

The next layer of the Sun is the chromosphere, so named because of its red color visible during solar eclipses. The base of the chromosphere has a temperature of 4 000 Kelvin [Ryden & Peterson, 2010]. The chromosphere extends to a height of 2 500 km above the photosphere where the temperature increases to about 9 000 Kelvin. The area between the chromosphere and the Sun's outer most layer is referred to as the solar transition region. There is a sharp temperature increase through this region to the outer most layer which can reach over two million Kelvin [Kivelson & Russell, 1995].

The outer most layer of the Sun is the corona; this is the atmosphere of the Sun. The corona, most visible during solar eclipses, is shown in figure 1-1. It is in the solar corona that storms from the Sun originate [Carlowicz & Lopez, 2002].

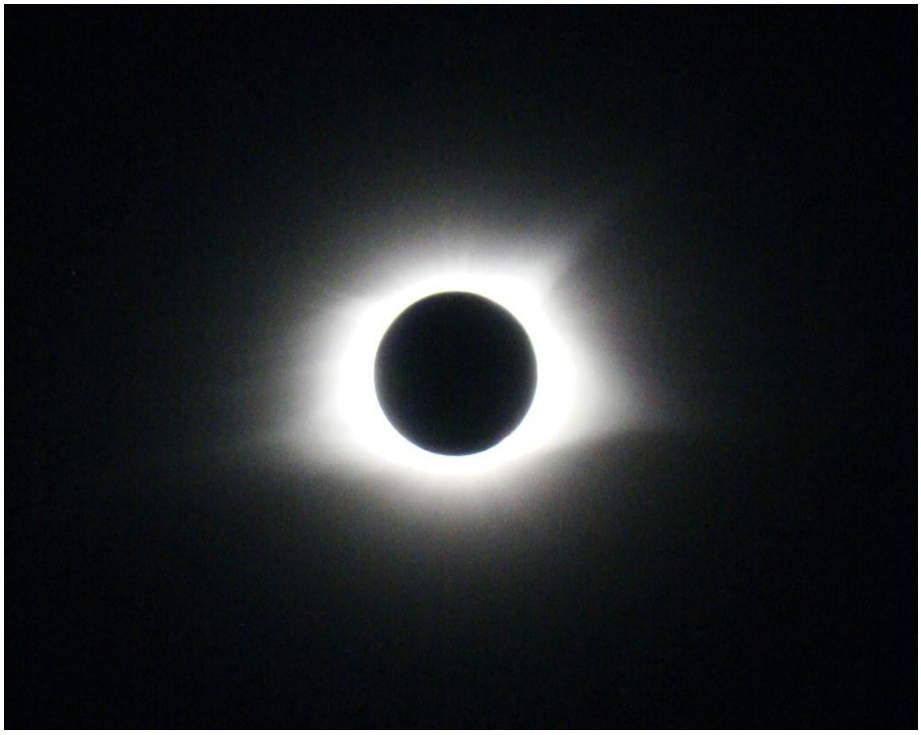

Figure 1-2 August 21, 2017 solar eclipse from Nashville, TN [Credit: Richard Bonde].

Figure 1-2 shows the most recent solar eclipse in 2017. The corona is the white area surrounding the eclipsed Sun. While the plasma visible in this picture suggests that the corona is restricted near the Sun, the corona extends out into interplanetary space. All the planets of the solar system live within the Sun's outer atmosphere [Carlowicz & Lopez, 2002].

The plasma present in the solar corona is very tenuous: less than 10^5 particles/cm^{-3}, compared to 10^{14} particles/cm^{-3} at the photosphere (for additional comparison, the number density at the surface of Earth is 10^{19} particles/cm^{-3}) [Tascione, 2010]. The temperature in the solar corona is so hot that the pressure blows away the outer plasma into interplanetary space. This plasma is referred to as the solar wind and it is essentially the plasma that has been boiled away from the Sun's outer atmosphere.

1.2 Solar Wind

The solar wind is a sustained yet nonuniform stream of particles from the Sun's outer atmosphere. It carries away one billion kg/s of material [Tascione, 2010]. At 1 AU (astronomical unit, the average distance from the Sun to Earth, about 150 million km), the solar wind has an average speed of 400 km/s, a number density of 5 particles/cm^{-3}, and consists of roughly 95% hydrogen and 5% helium [Kivelson & Russell, 1995].

Due to the extreme temperatures of the corona, the solar wind is fully ionized. When it is ejected out into planetary space, the solar wind is considered quasineutral. This assumption is called the plasma approximation and it states that there are an equal number of ions as there are electrons (i.e. $n = n_e = n_i$). If this were not the case, very large electric fields would result. A consequence of this is that no space charge can accumulate (i.e. $\nabla \cdot \boldsymbol{J} = 0$). Fully ionized, quasineutral plasmas have unique electrical properties.

1.2.1 Alfvén's Theorem & Plasma Beta

Plasmas are considered infinitely conducting. If an infinitely conducting magnetized fluid (plasma) were kept in a uniform magnetic field, any lateral motion of the plasma would give rise to infinite currents – this would produce an infinite induced magnetic field and in turn, magnetic forces which "fasten" the plasma onto the magnetic field. The plasma is essentially "frozen" into the magnetic field. Hannes Alfvén was the first to recognize this property – he alluded to it in *Alfvén* (1942) and fully described it in a subsequent paper the same year. This "frozen-in" theorem bears his name for this discovery.

Figure 1-3 shows an example of the frozen-in theorem. The red lines are magnetic field lines and the blue squares represent plasma particles. The magnetic field

line on the left carries five plasma particles on it a time $t = t_0$. The line on the right is the same magnetic field line and plasma particles, only at time $t = t_1$, where the magnetic field line has become bent. The plasma particles are forced to move with the magnetic field line due to Alfvén's theorem.

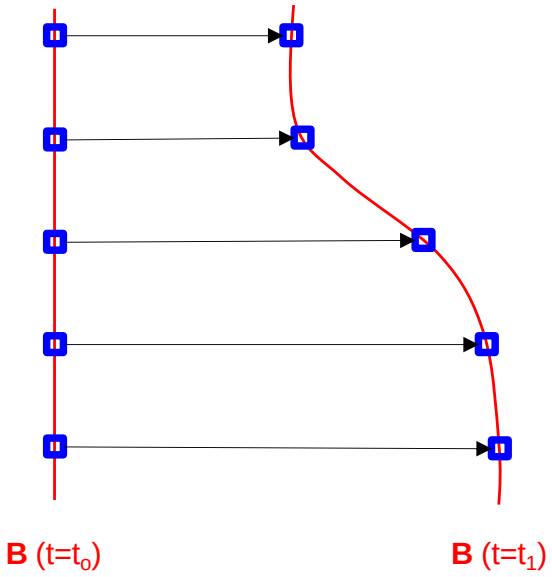

Figure 1-3 An illustration of frozen-in flux. The blue squares represent plasma particles and the red lines are magnetic field lines (or magnetic flux tubes).

It should be noted that a field line is a conceptual tool to visualize part of a vector field and is not a real object. However, charged particles orbit an area enclosed by the radius of their gyromotion. A magnetic field line could be visualized through the center of this area. Since the particles are frozen in to this area, a magnetic field "line" starts to become a real object. In this sense, we can consider this area not as a line, but as a tube of magnetic flux. This certainly is a physical characteristic of a magnetic vector field.

All references to physical magnetic flux tubes are generally referred to as magnetic field lines.

In looking at figure 1-3, one might ask: “Why doesn’t the plasma carry the magnetic field line rather than the field line carrying the plasma?” This could also be the case, but it depends on the pressure. A useful parameter in plasma physics is the ratio of thermal gas pressure to magnetic pressure, called plasma beta,

$$\beta = \frac{N k_B T}{B^2/2\mu_0} \tag{1.1}$$

Where N is the number density of the plasma, k_B is the Boltzmann constant, T is the plasma temperature, B is the magnitude of the plasma’s magnetic field, and μ_0 is the permeability of free space. If $\beta >> 1$, the plasma will drag the magnetic field lines. If $\beta << 1$, the magnetic pressure will restrict the plasma along the magnetic field lines.

Figure 1-4 shows approximate values of plasma beta for the outer three layers of the Sun. In the photosphere and the first half of the chromosphere, $\beta > 1$, which means that the plasma pressure dominates and the plasma will drag the magnetic field along with it. In the second half of the chromosphere and most of the corona, $\beta < 1$, meaning the magnetic pressure is much greater and the magnetic field lines restrict the plasma. Just above 10^6 km, $\beta > 1$ and this is referred to as the solar wind accelerated region. It is here that the temperature is hot enough that the plasma pressure overcomes the magnetic pressure and the plasma is blown out into interplanetary space.

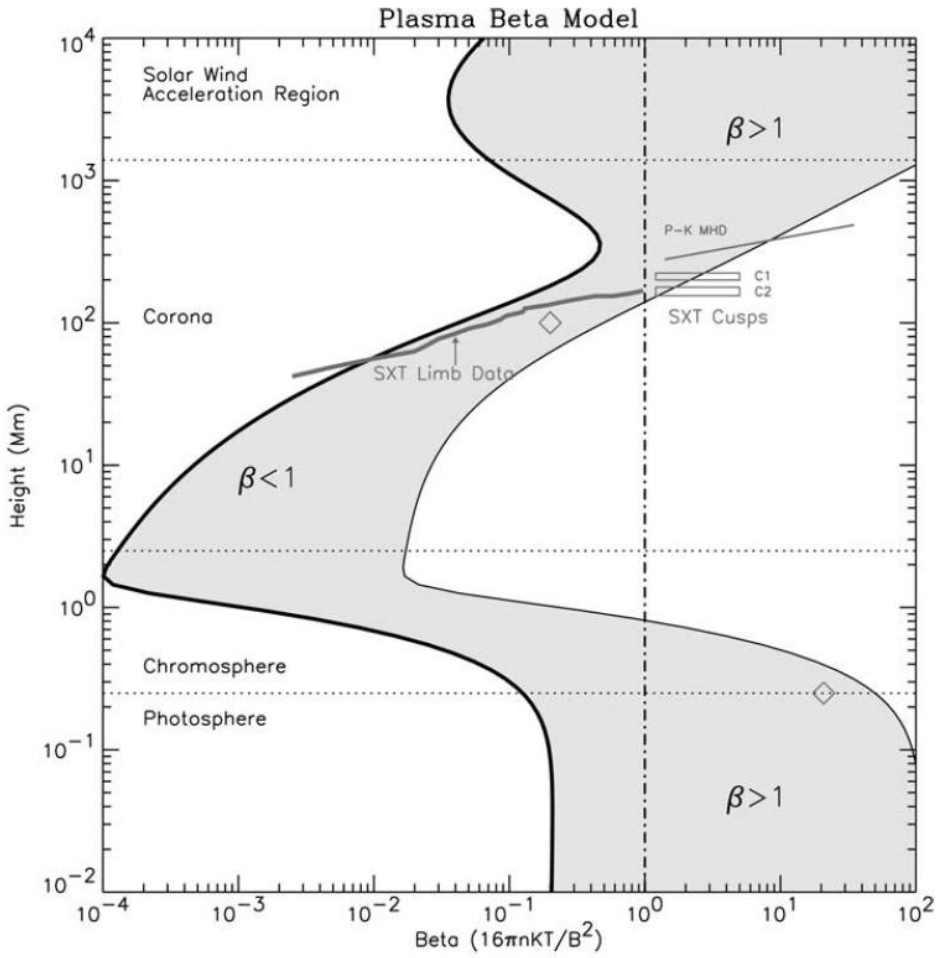

Figure 1-4 Plasma beta approximations for the outer three layers of the Sun [figure 3 from *Gary* (2001)].

1.2.2 Interplanetary Magnetic Field

As stated earlier, the magnetic field can restrict the plasma, or the plasma can drag the magnetic field along with it, depending on the value of the plasma beta. Figure 1-4 shows that in the solar wind accelerated region, the plasma will drag the magnetic field along with it since β> 1. This field is the Sun's magnetic field and once the plasma has dragged it out into interplanetary space, it becomes known as the IMF (interplanetary

magnetic field). The embedded IMF is a crucial part of how the solar wind interacts with Earth.

1.2.3 Solar Rotation

The Sun's rotation has an effect on the solar wind, namely a rotating garden sprinkler effect. Although the solar wind outflow is radial, the solar rotation causes a spiral-like pattern seen in figure 1-5. This spiral pattern is known as the Parker spiral, after Eugene N. Parker, who developed the prevailing theory of the solar wind [Parker, 1958]. Figure 1-5 shows the Parker spiral for 400 km/s (red) and for 2 000 km/s (yellow). The spiral structure of the solar wind diminishes with increasing solar wind speed.

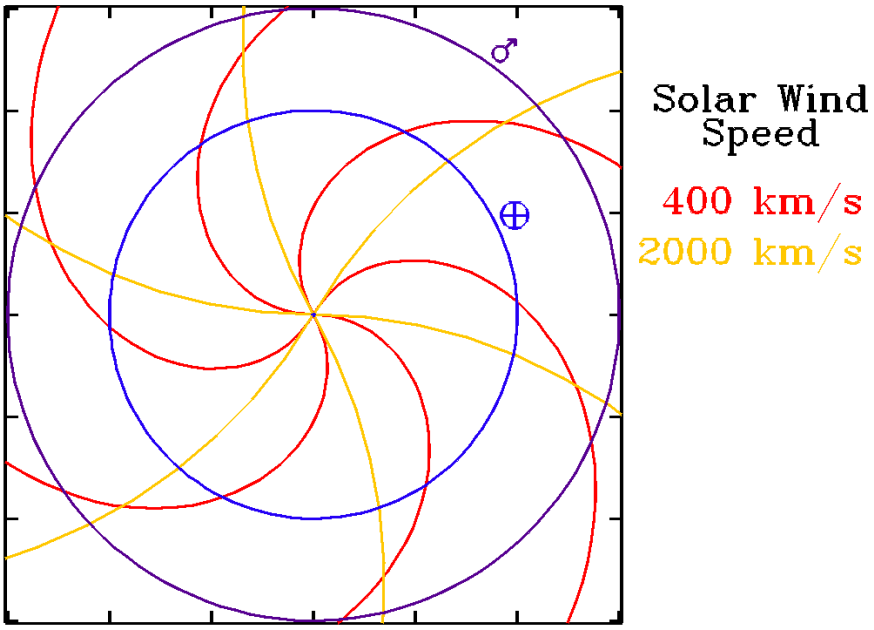

Figure 1-5 The Parker spiral solar wind pattern. Earth's orbit is seen in blue and Mars' orbit in purple [Wikimedia Commons].

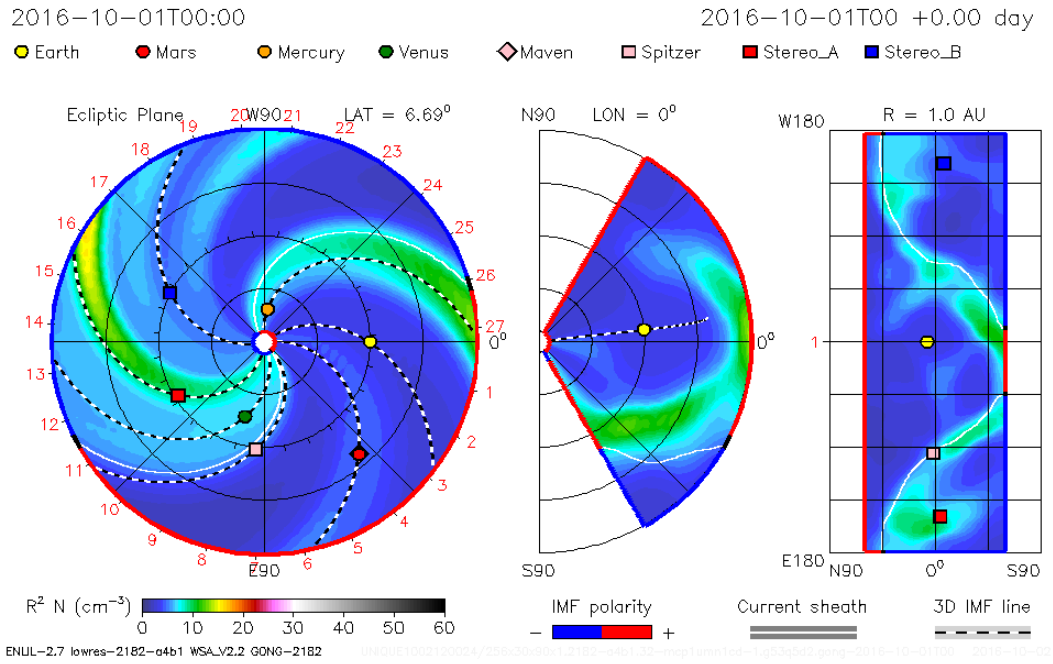

Figure 1-6 WSA-Enlil solar wind model color-coded for density [NOAA/NGDC].

Figure 1-6 shows a model output from the WSA-Enlil solar wind model. The ecliptic plane cut on the left, color-coded for density, shows the spiral nature of the solar wind.

The solar rotation is unlike the rigid rotation of the terrestrial planets as the Sun is in a plasma (fluid) state – the equatorial regions of the Sun rotate faster than the poles. The poles rotate about once every 35 days and the equator rotates about once every 25 days, an effect known as differential rotation.

It is not convenient to have different rotation periods when tracking solar features that return over multiple solar rotations, such as sunspots. The most commonly used rotation period is the Carrington rotation, named after Richard Carrington, who tracked sunspots across the Sun, observing differential rotation [Carrington, 1859]. The Carrington rotation is the mean synodic rotation period of the Sun – roughly 27 days.

Carrington rotations have been tracked since Richard Carrington's work in the 1860s. We are currently, as of the writing of this work, entering Carrington rotation 2200.

1.2.3.1 Heliospheric Current Sheet

If we take the solar magnetic field to be roughly dipolar, there is magnetic field emanating from each of the solar poles, in opposite directions. These field lines extend out into interplanetary space. In interplanetary space, where the field lines change direction, there must be a current sheet, as per Ampère's law. This current sheet is the heliospheric current sheet. A schematic of the heliospheric current sheet is shown in figure 1-7. The magnetic axis, *M*, is offset from the rotation axis, *Ω*. This gives an azimuthal tilt to the IMF and thus, the heliospheric current sheet. The combination of the azimuthal tilt and the solar rotation gives the current sheet a shape like that of a ballerina skirt (an artist's rendition is shown in figure 1-8).

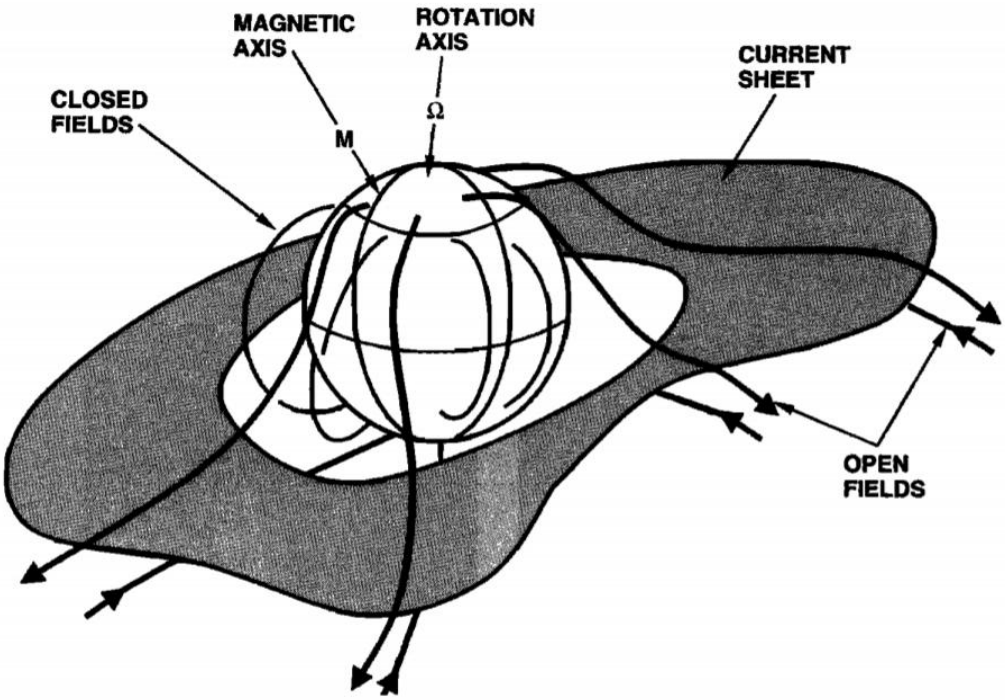

Figure 1-7 Schematic of the heliospheric current sheet [figure 1 from *Smith* (2001)].

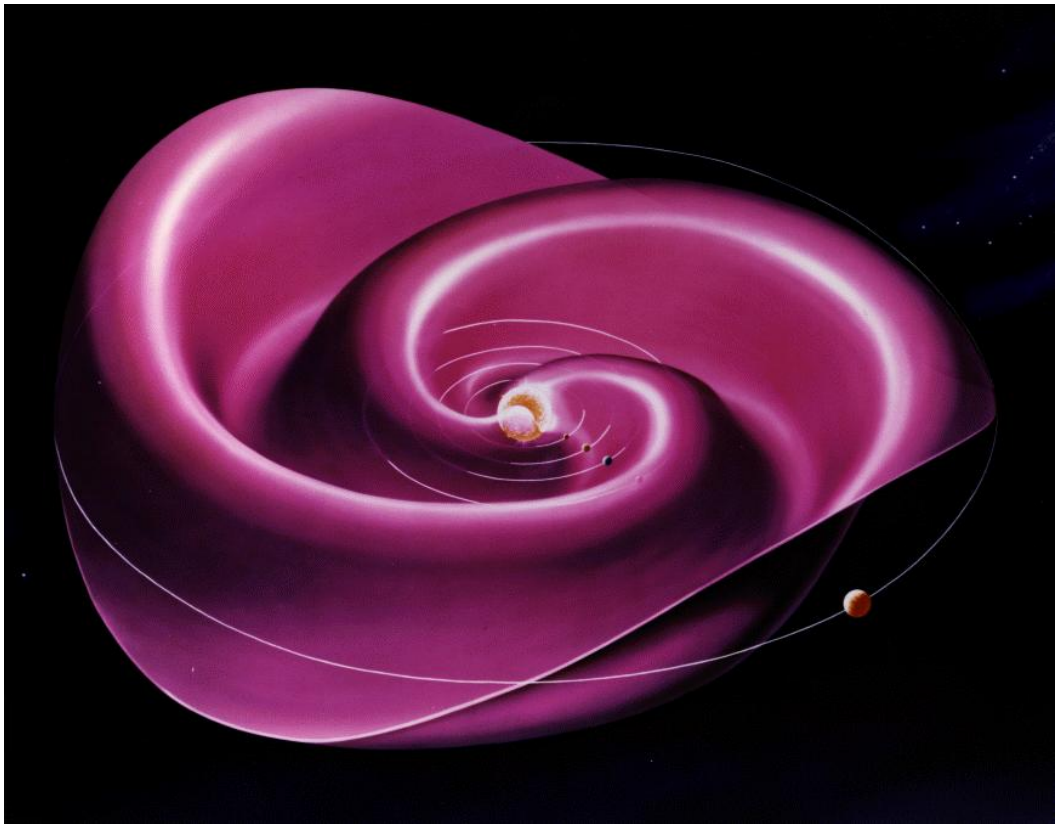

Figure 1-8 Artist's rendition of the heliospheric current sheet. The orbit up till Jupiter is shown [Heil & Wilcox/Stanford/WSO].

1.2.4 Magnetohydrodynamic Waves

The solar wind falls under the territory of magnetohydrodynamics (MHD) since it is a highly conductive fluid. In describing a fluid theory, we can discuss wave propagation. This is important because in the solar wind acceleration region, the solar wind is accelerated to supersonic speeds. In air, disturbances are transmitted through pressure waves (sound) and travel at the speed of sound. The restoring force in this instance is the pressure. In air, the density is large enough that these transmissions are being propagated due to collisions.

In plasma so rarefied as the solar wind, the collisional mean free path is over 1 AU [Kivelson & Russell, 1995]. Therefore, collisions do not play a role in the solar wind plasma; however, there are wave-particle interactions on the microscopic level that allow for similar behavior as collisions. A longitudinal, compressional sound wave can still exist in space plasmas. Furthermore, there are many different types of interactions in magnetized plasmas that give rise to many different types of waves. One of the most important waves in MHD is the Alfvén wave. This wave propagates as a shear wave (perpendicular to the magnetic field direction) and it is due to magnetic disturbances. One can imagine these waves as a guitar string being plucked. In the case of the guitar string, the restoring force is the tension whereas the restoring force in Alfvén waves is the magnetic force.

Of the MHD waves, there are three that are of importance to this study and their speeds are given as follows:

$$C_S = \sqrt{\frac{\gamma P_{SW}}{\rho_{SW}}} \qquad (Sound\ Speed) \tag{1.2}$$

$$V_A = \frac{B_{SW}}{\sqrt{\mu_0 \rho_{SW}}} \qquad (Alfvén\ Speed) \tag{1.3}$$

$$V_{MS} = \sqrt{V_A^2 + C_S^2} \qquad (Fast\ Magnetosonic\ Speed) \tag{1.4}$$

where P_{SW} is the solar wind plasma pressure, ρ_{SW} is the solar wind proton density, B_{SW} is the magnitude of the IMF, μ_0 is the permeability of free space, and γ is the ratio of specific heats. The typical values of the sound and Alfvén speeds are 40 km/s and 50 km/s, respectively. The associated typical Mach numbers for the sound and Alfvén speeds are, M_S = 10 and M_A = 8. The third MHD wave, described in equation 1.4, is the fast magnetosonic wave.

1.2.5 High-Speed Streams

Solar wind speed is generally broken up into two categories: slow solar wind and fast solar wind. Solar wind with speeds less than 450 km/s are generally considered as slow wind and above 450 km/s it is considered fast wind. The typical speeds (at 1 AU) of the solar wind fall into the slow wind category. There are regions on the Sun with open magnetic field lines. These areas, called coronal holes, have relatively cool and less dense plasma. This allows the plasma to be accelerated at higher speeds than average – these are called high-speed streams (HSS) [Krieger et al., 1973; Sheeley et al., 1976]. Coronal holes can last several Carrington rotations.

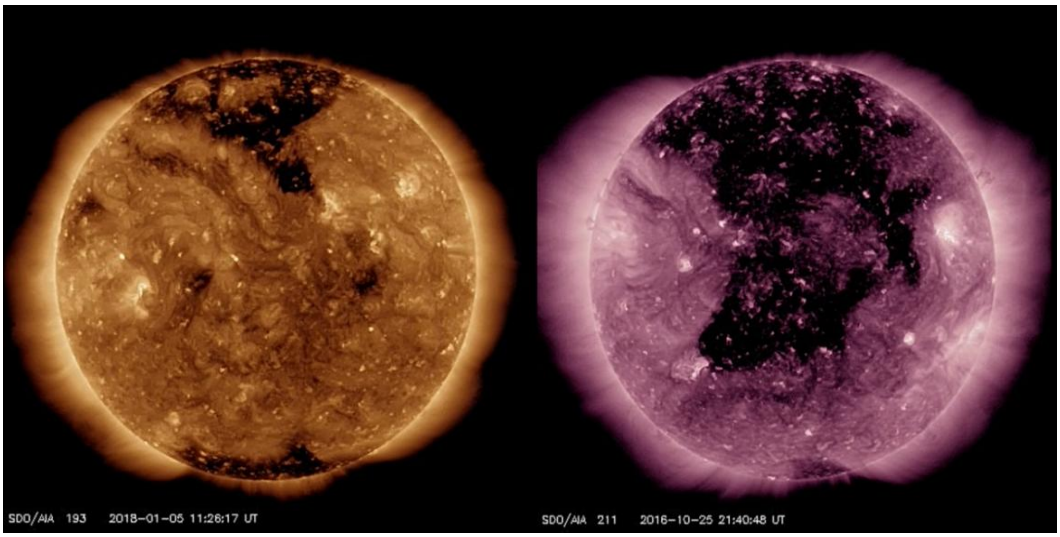

Figure 1-9 The Sun in Extreme Ultraviolet (EUV): 193 Å (left) and 211 Å (right) [NASA/GSFC/SDO/AIA].

Figure 1-9 (left) shows the Sun in extreme ultraviolet (EUV) on January 5, 2018. The dark regions near the poles are coronal holes. The Sun's magnetic is somewhat dipolar near solar minimum and the open polar regions will often have coronal holes.

Coronal holes can often dip towards the equatorial regions, sending higher velocity solar wind towards Earth. Figure 1-9 (right) shows the Sun on October 25, 2016, again in EUV but at a different wavelength. The coronal hole can be seen extending down from the northern polar region to the equatorial region. This sent a HSS towards Earth with solar wind speeds in excess of 600 km/s.

Slow solar wind is characterized mostly by compressional fluctuations whereas HSS are mostly Alfvénic fluctuations and have an average speed of 700 km/s to 800 km/s [Kivelson & Russell, 1995].

1.2.6 Co-rotating Interaction Regions

When solar wind from a HSS is ejected out into interplanetary space, it will be moving faster than the ambient solar wind speed. This will compress the solar wind in front of the HSS. The compression affects both density and the magnetic field. This region is known as a co-rotating interaction region (CIR), or stream-stream interaction.

Figure 1-10 shows a cartoon of what a co-rotating interaction region would look like. The blue-shaded region is the HSS. The red-shaded region in front of the HSS is the compressed solar wind. A shock front may develop in front of the compressed region. The area just behind the HSS is rarefied solar wind. The spiral shape of the CIR again comes from the solar rotation. Since CIR contains a HSS, they also have large Alfvénic fluctuations.

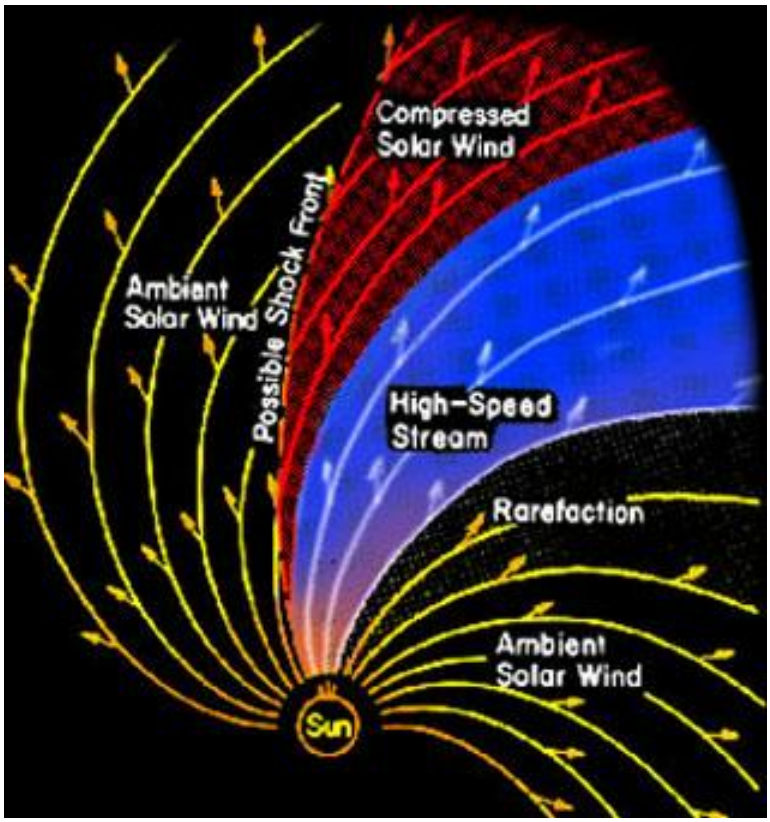

Figure 1-10 Cartoon showing the interaction of a high-speed stream with the ambient solar wind [UC Riverside/IGPP].

1.3 Solar Activity

1.3.1 Solar Cycle

The Sun goes through a myriad of changes from year-to-year, day-to-day, and even hour-to-hour. All of these changes affect Earth in a number of different ways.

The solar cycle refers to a periodic cycle of the Sun's magnetic activity – this period is roughly 11 years. At present (2018), we are in solar cycle 24. Cycle 24 started in 2008 and will end approximately in 2019. The 24th cycle is referenced from what is considered the first solar cycle starting in 1755. This is when the most extensive sunspot records were traced back to.

The solar cycles end and begin with a solar minimum, defined by a minimum of sunspots and the location of those sunspots being the farthest away from the solar equator. As the cycle progresses, magnetic activity increases and the sunspots move towards the solar equator. Solar maximum refers to a maximum of magnetic activity and a time period of maximum sunspot numbers; however, the sunspots still migrate towards the solar equator. The new cycle is defined when the new sunspots start appearing at higher magnetic latitudes and the solar magnetic field changes direction [Harvey & White, 1999].

The migration of sunspots is directly related to the Sun's magnetic field. During solar minimum, the solar magnetic field is ordered and somewhat dipolar (see figure 1-11 left). The closed magnetic field lines are more stretched than a tradition dipole field. HSS are more common during solar minimum [Bame et al., 1976; Babcock, 1959]. As the solar cycle progresses, the field becomes twisted, disordered, and complex (see figure 1-11 right). This increases the chance for magnetic activity, such as flares and coronal mass ejections. Although the frequency of solar events increases during solar maximum, the largest events usually take place during the declining phase of the maximum [Jang et al., 2016].

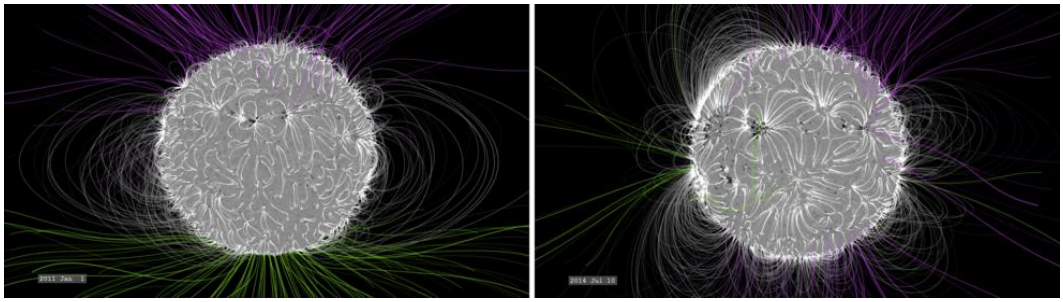

Figure 1-11 Model of the solar magnetic field during solar minimum (left) and during solar maximum (right) [Bridgeman/NASA/GSFC].

1.3.2 Solar Flares

A solar flare is a sudden explosion of energy from the solar surface. It is in a sense, an intense brightening of the Sun. Although the energy released during a solar flare covers a wide spectrum, it is most concentrated in the EUV and x-ray frequencies. Figure 1-12 shows the Sun in EUV at two different wavelengths during one of the largest solar flares in the past decade (and certainly the largest during the current solar cycle, 24). The flare occurred on the bottom right of the visible disk. It is clearer in the 131 Å picture on the left of figure 1-12 that the flare has occurred.

Since a solar flare is an intense brightening of mostly EUV and x-rays, the particles released during a solar flare are photons. This mostly has consequences in Earth's upper atmosphere. Sometimes a flare can create a shock which could accelerate solar protons.

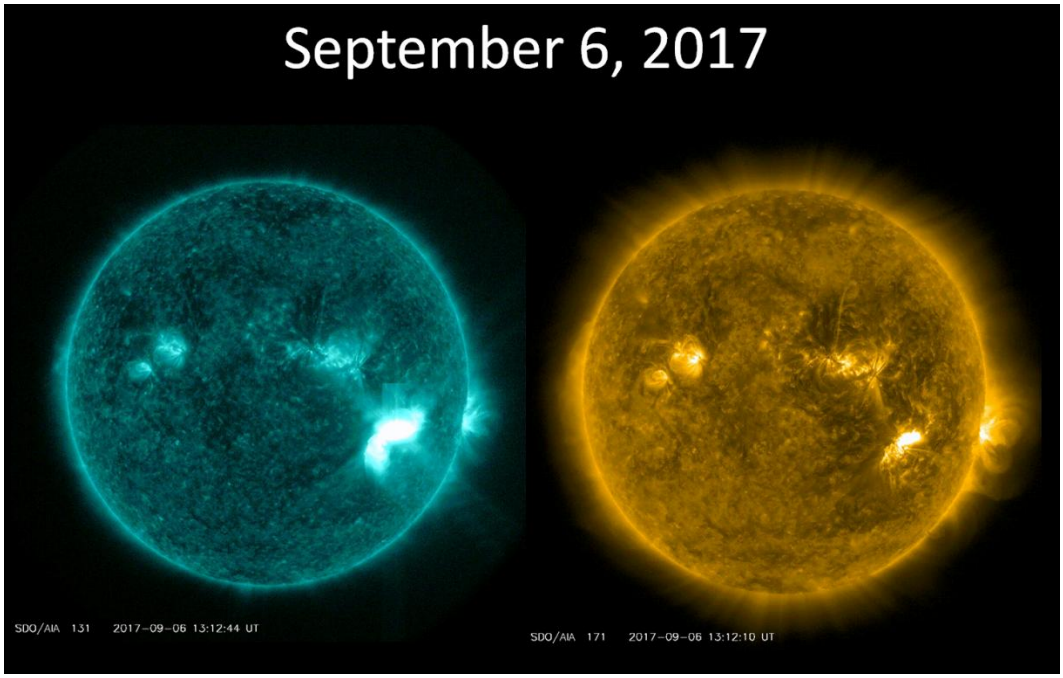

Figure 1-12 The Sun in EUV: 131 Å (left) and 171 Å (right) [NASA/SDO/GSFC].

1.3.3 Coronal Mass Ejections

Another aspect of solar activity that is often confused with solar flares is the coronal mass ejection (CME). A CME is a large eruption of plasma from the surface of the Sun. Although both flares and CMEs are triggered by similar magnetic processes, they are completely different events. Figure 1-13 shows a CME captured by the STEREO B (Solar Terrestrial Relations Observatory Behind) spacecraft on 23 July 2012. CMEs expand very quickly and sometimes reach speeds in excess of 2 000 km/s. The CME on 23 July 2012 shown in figure 1-13 was initiated roughly an hour before this picture was taken and it is already several times larger than the solar diameter (white circle).

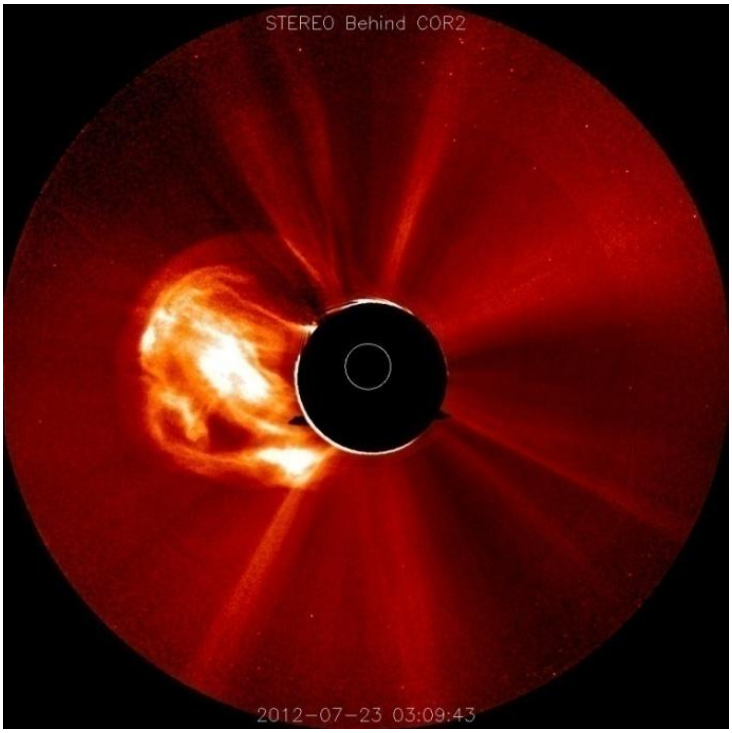

Figure 1-13 CME on 23 July 2012 from the STEREO B spacecraft. The white disk in the center of the black occulting disk is the approximate position and size of the Sun [NASA/GSFC/STEREO].

The impact of CMEs on Earth is not just the dynamic pressure it exerts on Earth's magnetic field, but what's embedded inside a CME: magnetic field. This magnetic field can interact with Earth in a number of different ways.

CMEs and solar flares are not associated with each other, although sometimes large flares can trigger CMEs and vice versa.

1.3.4 Solar Filaments (Prominence)

It has hopefully been demonstrated thus far that the Sun is a highly dynamic object and that solar activity covers many aspects of the Sun with the most important ones to this study being presented here. The last aspect of solar activity that has an impact on this work is the solar filament. A solar filament is a loop of slightly cooler and denser (compared to the solar corona) plasma that has been lifted off the Sun's surface into the corona due to magnetic buoyancy, with the ends of the loop anchored to the photosphere.

The difference between a solar filament and a prominence is where they occur. If the loop occurs against the visible disk of the Sun, it is referred to as a filament. If it occurs against the backdrop of space, it is referred to as a prominence – these are visually more striking. They are both one in the same object however. Figure 1-14 shows a solar prominence with Earth superimposed to show the scale of how large a prominence can be.

Even though the ends of a filament are anchored to the photosphere, sometimes a filament can erupt and be shot out into interplanetary space. While filaments will not travel as fast as CMEs, the important characteristic of a filament, like a CME, is the embedded magnetic field.

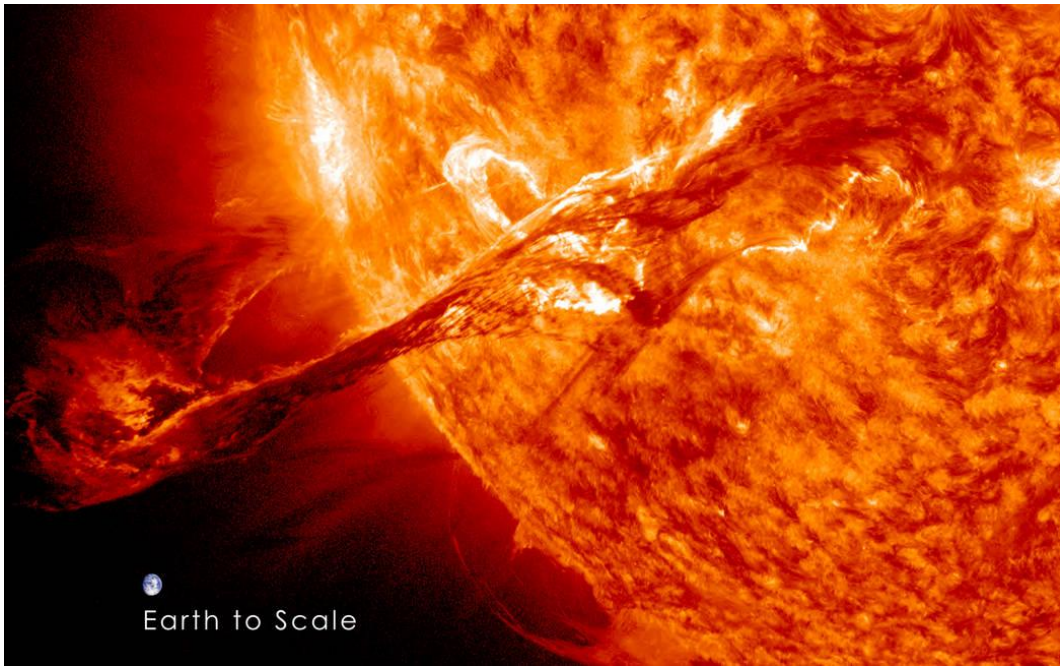

Figure 1-14 Close-up of a solar prominence/filament captured by Solar Dynamics Observatory (SDO) with Earth superimposed on the image [NASA/GSFC/SDO/AIA].

1.4 Coordinate System

It is at this point that we must introduce a coordinate system. The most convenient coordinate system to use for this work is the geocentric solar magnetic (GSM) coordinate system. The line connecting the Sun and Earth is defined as the X-axis: the Sun-Earth line. Earth's magnetic dipole axis is contained in the X-Z plane and the Y-axis is perpendicular to Earth's magnetic dipole axis and thus, the X-Z plane. On the next page, figure 1-15 shows a side view and figure 1-16 shows a perspective view of the GSM coordinate system. In the coordinate system used, the solar wind speed in the *X* direction is negative.

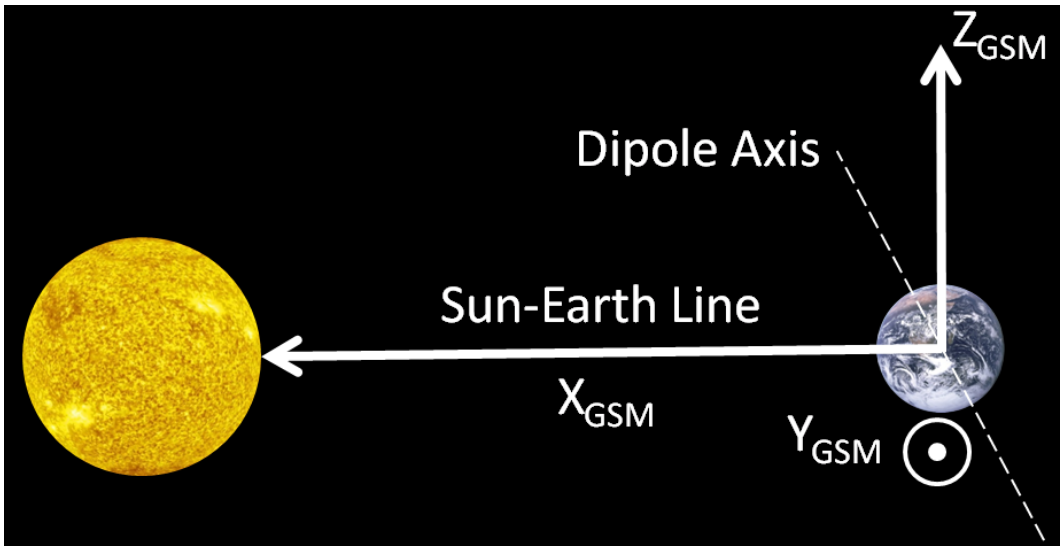

Figure 1-15 GSM coordinate system (side view – from positive *Y*).

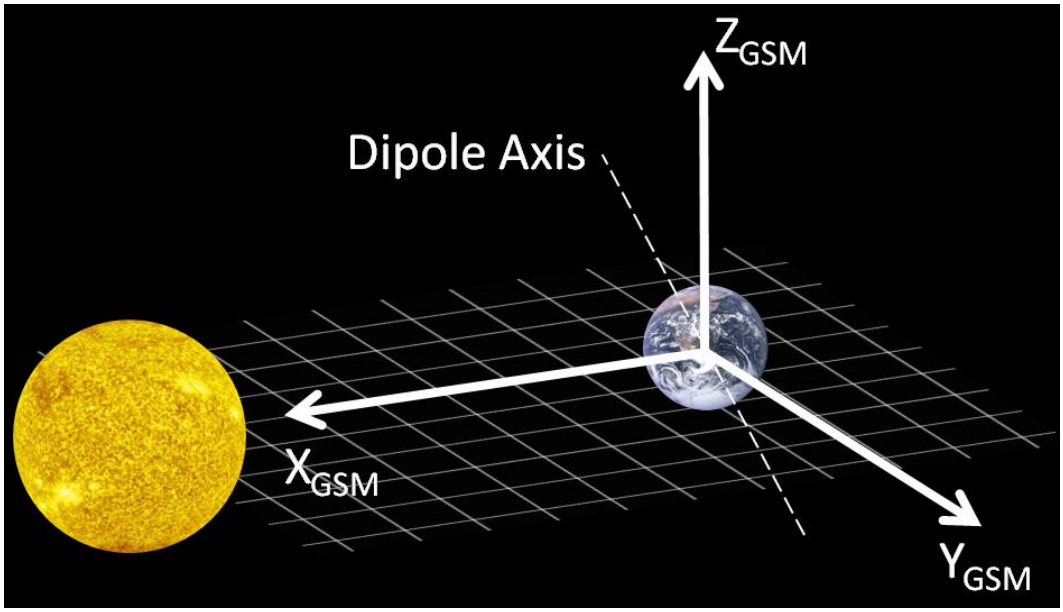

Figure 1-16 GSM coordinate system (perspective).

1.5 The Geospace Environment

The geospace environment refers to the area near Earth in outer space all the way down to the upper levels of the atmosphere.

1.5.1 Bow Shock

The first part of geospace that the solar wind and IMF encounters is a detached shock wave in front of Earth. This shock wave, referred to as a bow shock, is due to the supersonic and super-Alfvnic solar wind that encounters Earth's magnetic field, which the solar wind sees as a blunt body. The solar wind velocity reduces to subsonic and sub-Alfvénic speeds. This shock wave heats and compresses the plasma. The IMF is also compresses, increasing in magnitude.

The region just after the bow shock, but before the magnetosphere, is called the magnetosheath. The magnetosheath is the yellow-shaded region in figure 1-17 and the bow shock can be seen in front of the magnetosphere. During quiet times, the bow shock stands roughly 14 R_E in front of Earth.

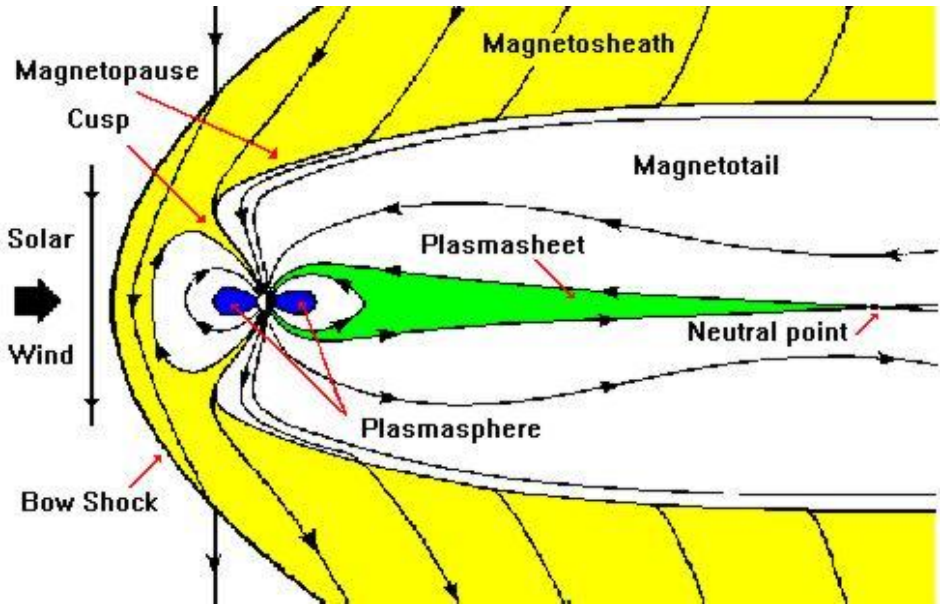

Figure 1-17 Schematic of Earth's magnetosphere in the meridional plane [NASA/GSFC].

1.5.2 Magnetosphere

The entire section in white (figure 1-17), enclosed by the yellow-shaded magnetosheath region, is called the magnetosphere. The magnetosphere contains Earth's dipole magnetic field, as well as plasma originated from Earth. The distinct comet-like shape of Earth's magnetosphere comes from a magnetic draping effect due to the embedded IMF in the solar wind. Earth's dipole field is compressed on the dayside and stretched out on the nightside to several hundred R_E. The stretched portion of the magnetosphere is called the magnetotail (see figure 1-17). The shape of the magnetosphere is highly dynamic.

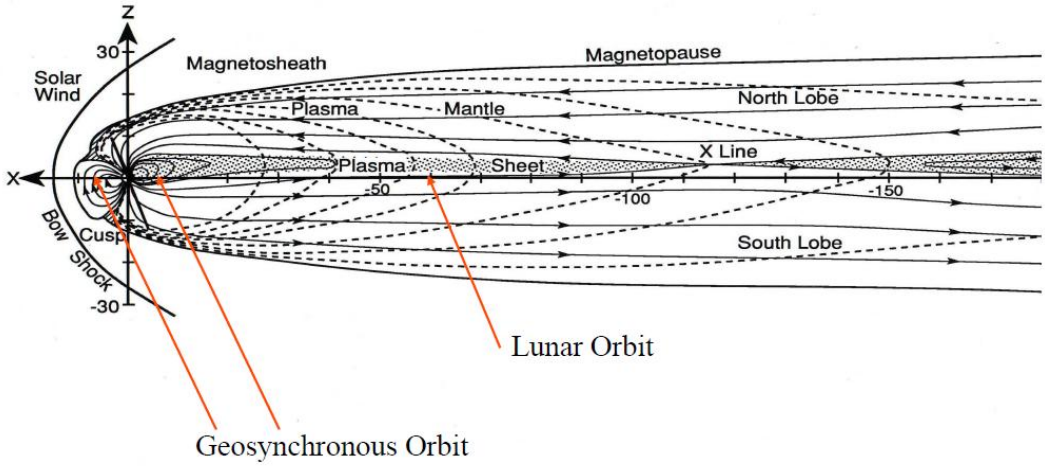

Figure 1-18 Earth's magnetosphere (drawn to scale) in the meridional plane [*Hughes* (2016)].

Earth's magnetosphere is drawn to scale in figure 1-18, showing only a portion of the magnetotail. As was the case for the heliospheric current sheet, Earth's dipole field changes direction near the equatorial region, creating a current sheet. The plasma in this area is hotter and the magnetic field is weaker. This area surrounding the current sheet is called the plasma sheet (green-shaded region in figure 1-17). The areas just above and below the plasma sheet are the tail lobes (northern and southern tail lobes,

respectively; see figure 1-18). This is area of extremely tenuous plasma and stronger magnetic field than the plasma sheet.

The inner portion of the magnetosphere is referred to as the plasmasphere (blue-shaded region in figure 1-17). The plasmasphere is filled with relatively cold plasma which co-rotates with Earth. The inner and part of the outer Van Allen radiation belts are within the plasmasphere.

1.5.2.1 Magnetopause

A particular feature of the magnetosphere that is of considerable significance to this work is the magnetopause (see figure 1-17). This is the boundary between Earth's dipole field containing Earth-dominated plasma and the shocked solar wind plasma of the magnetosheath. To a good approximation, the magnetopause location is determined by the pressure balance between the solar wind dynamic pressure and Earth's dipole magnetic pressure [e.g. Kivelson & Russell, 1995]. The magnetopause location lies at the locus of points where magnetosheath and magnetospheric thermal and magnetic pressures balance [Sibeck et al., 1991]. As can be seen in figure 1-18, the magnetopause is the outer boundary of the entire teardrop-shaped magnetosphere. Of even more particular interest to this research is the location of the subsolar magnetopause position – this is the position of the magnetopause closest to the Sun, which occurs along the Sun-Earth line (the farthest left white-shaded region of figure 1-17).

If we equate the solar wind dynamic pressure and Earth's magnetic field pressure, we get the force balance equation,

$$\rho_{SW} V^2 = \frac{B^2}{2\mu_0} \tag{1.5}$$

where *V* is the solar wind speed and *B* is the value of Earth's magnetic field. If we take Earth's magnetic field to scale as a dipole field, the magnetic field scaling would be,

$$B = \frac{B_0}{r^3} \tag{1.6}$$

where B_0 is the strength of Earth's magnetic field at the surface (roughly 31 000 nT) and *r* is the distance in R_E. Substituting equation 1.6 into equation 1.5 leads to,

$$r = \left(\frac{2B_0^2}{\mu_0 \rho_{SW} V^2}\right)^{1/6} \tag{1.7}$$

This equation will estimate the stand-off distance: the distance to the subsolar magnetopause location. The magnetopause location is highly dynamic and changes with changing solar wind and IMF conditions. The single most important factor in determining the magnetopause location is the solar wind dynamic pressure [Martyn, 1951].

1.6 Solar Wind-Magnetosphere Coupling

The solar wind transfers energy and momentum into the magnetosphere. In 1961, a couple of papers were published that provided theories on the mechanisms of how energy and momentum are transferred to the magnetosphere [Dungey, 1961; Axford & Hines, 1961]. These papers set apart the area of space physics from other research areas.

1.6.1 Magnetic Reconnection

Earth's magnetic dipole points northward (positive Z using GSM coordinates). In figure 1-17, an IMF line (just in front of the bow shock) is shown with a southward orientation (negative Z). In interesting question would be: what would happen if two oppositely directed filed lines, like a southward IMF line and a northward dipole line, were to come together? The answer is a predominant process in space physics called magnetic reconnection (also referred to as magnetic merging).

Figure 1-19 shows a three-panel sequence of a magnetic reconnection event. In figure 1-19A, two antiparallel magnetic field lines move towards the orange box (referred to as the electron diffuse region). The coordinate system at the top of figure 1-19A is reflective of the GSM coordinate system. The field line on the left could represent a southward IMF field line and the field line on the right could represent a field line from Earth's magnetic dipole.

In figure 1-19B, both of these field lines merge in the electron diffuse region. The result of this merging is a breakdown of Alfvén's theorem (frozen-in flux). Figure 1-19C shows that the magnetic field lines from the IMF and Earth's magnetic dipole have now merged into one magnetic field line. These "new" field lines exit in the electron diffuse region perpendicularly to the direction in which they merged.

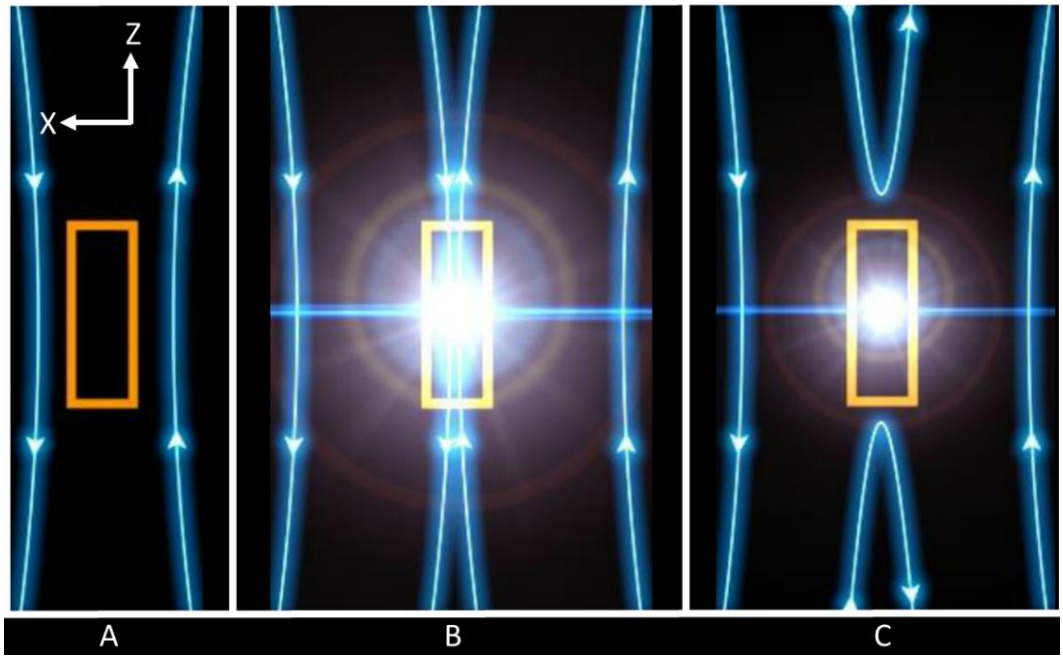

Figure 1-19 Three-panel sequence of a magnetic reconnection event [adapted from The Comet Program ©, NCAR/HAO].

The result of magnetic reconnection is a rearrangement of magnetic topology and a conversion of magnetic energy to kinetic energy, as the plasma is accelerated out of the electron diffuse region in the direction of the newly merged field lines. Magnetic reconnection is theorized as the underlying process that triggers solar flares and CMEs.

1.6.1.1 Southward IMF – The Dungey Cycle

When the IMF is directed southward ($B_z < 0$), magnetic merging occurs near the subsolar magnetopause. IMF field lines merge with earth's dipole field lines and are then draped over the magnetosphere. This can be seen in figure 1-17. The red arrow marking the magnetopause is pointing to a dipole field line from Earth that has been merged with an IMF field line, shown in the magnetosheath. These lines continue down the magnetotail, draping over the magnetopause, until they meet at the neutral point in the magnetotail (see figure 1-17). At the neutral point, these oppositely directed field lines reconnect (hence the term magnetic reconnection). The plasma is accelerated out of the neutral point either towards Earth along dipole field lines, or back into the outer magnetotail. The reconnected dipole field lines are accelerated towards Earth and the reconnected IMF lines are accelerated back into interplanetary space.

This cycle of dayside merging and nightside reconnection is the most dominant mechanism for transferring energy and momentum in the magnetosphere – the cycle was first proposed by Jim Dungey in 1961 and is now referred to as the Dungey cycle [Dungey, 1961].

As a consequence of magnetic reconnection for southward IMF, there is a gap between the most outward closed dipole field line and the first dipole field line reconnected to the IMF – this gap is called the cusp and is shown in figure 1-17 (one cusp for each hemisphere). The cusp is an area where the solar wind plasma has direct access to Earth's upper atmosphere.

1.6.1.2 Northward IMF

When the IMF is directed northward, magnetic reconnection does not happen near the subsolar magnetopause since the IMF and Earth's dipole field are in the same direction. At high latitudes, Earth's dipole field is directed into the polar region and therefore oppositely directed from the IMF. Magnetic reconnection happens at these higher latitudes, poleward of the cusp regions, marked at the reconnection site figure 1-20.

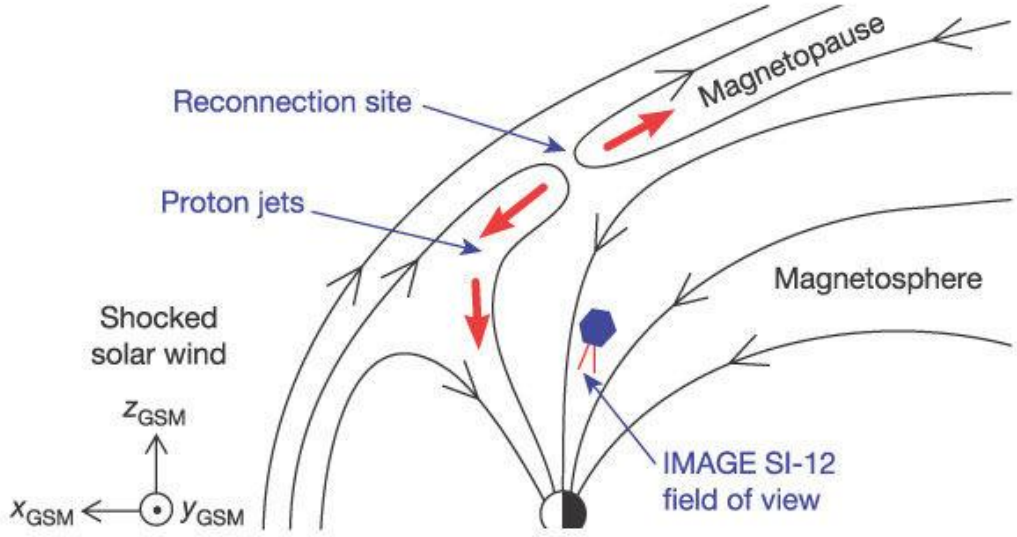

Figure 1-20 Magnetic reconnection diagram for northward IMF (meridional plane) [Figure 1 from *Frey et al.* (2003)].

1.6.1.3 East-West IMF

The third and last IMF direction to consider is East-West IMF (IMF B_y). The IMF direction in this configuration puts it perpendicular to Earth's magnetic dipole field lines. Reconnection will still happen near the subsolar magnetopause, albeit with less energy and momentum than with pure southward directed IMF.

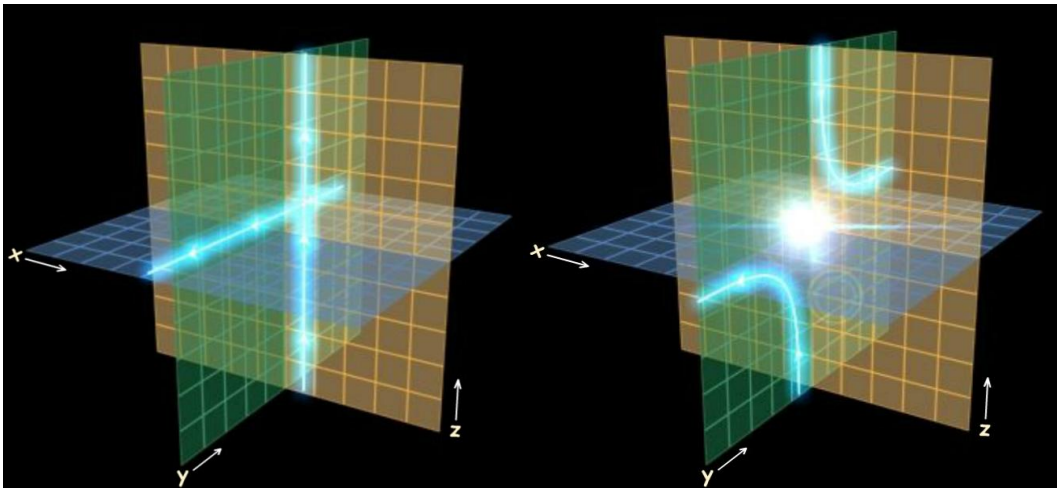

Figure 1-21 Sequence of an East-West IMF reconnection event [adapted from The Comet Program ©, NCAR/HAO].

In figure 1-21 (left) an IMF directed in the –*Y* direction approaches a dipole field line directed in the +*Z* direction. They merge at the center and the newly merged field lines exit the region in the *Y*-*Z* plane as shown in figure 1-21 (right). For southward IMF, the merged field lines left the region in the *X*-*Z* plane. Southward IMF reconnection is by far the most dominate reconnection process in the magnetosphere [Dungey, 1961]. Northward IMF is the second-most dominate reconnection process and East-West IMF direction transfers the least amount of energy and momentum to the magnetosphere.

1.6.2 Viscous Interaction

The shocked solar wind of the magnetosheath is deflected around the magnetosphere – better than 90% is diverted [Hughes, 2016]. The solar wind is then dragged down all around the magnetosphere. The northern and southern tail lobes have extremely tenuous plasma and do not really interact with the solar wind. Recall that the plasma sheet (see figure 1-17) has a higher plasma density than the lobes. The plasma sheet is mostly contained within the equatorial plane and extends to the flanks of the

magnetosphere. The boundary where the plasma sheet extends to the flanks at the magnetopause is called the low latitude boundary layer (LLBL).

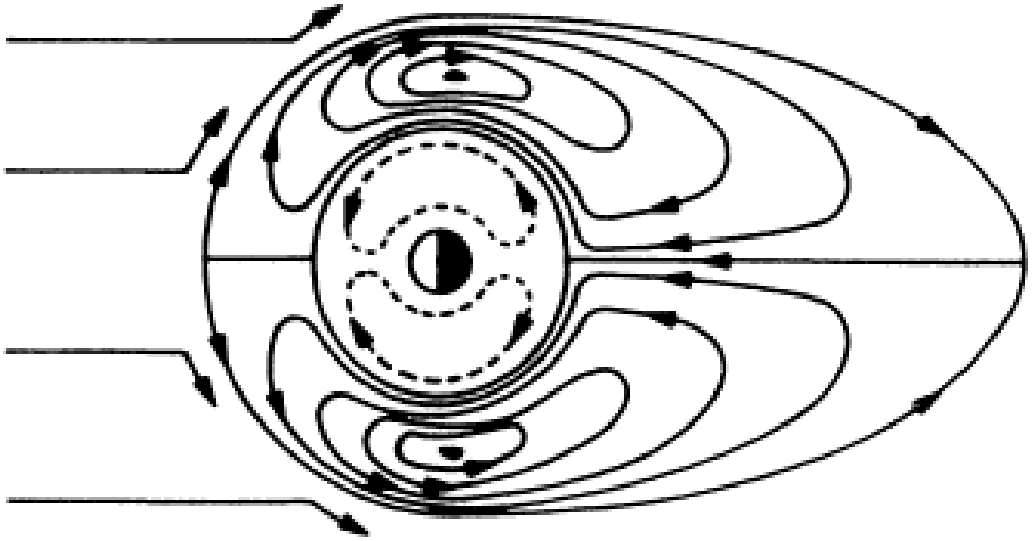

Figure 1-22 Schematic of the viscous interaction [figure 4 from *Axford & Hines* (1961)].

The solar wind that has been deflected to this region drags along the magnetopause, transmitting shear stress across the magnetopause. This shear stress transfers momentum to the plasma just inside the magnetopause (part of the plasma sheet). This plasma is then dragged down the magnetotail until it encounters the back edge of the magnetotail, where it is turned around and convected back up the center of the magnetotail towards Earth. Figure 1-22 shows the plasma flows associated with this pattern. This method of dragging the plasma along the boundary was first theorized in 1961 by W.I. Axford and C.O. Hines. They described this type of momentum transfer as a viscous-like interaction [Axford & Hines, 1961].

Figure 1-23 shows an MHD simulation in the equatorial plane. The black line is the magnetopause. Just outside in the magnetosheath and just inside the

magnetosphere, the arrows indicate an anti-sunward flow. The arrows further in the magnetosphere show the return flow, completing the set of viscous cells (shown in figure 1-23).

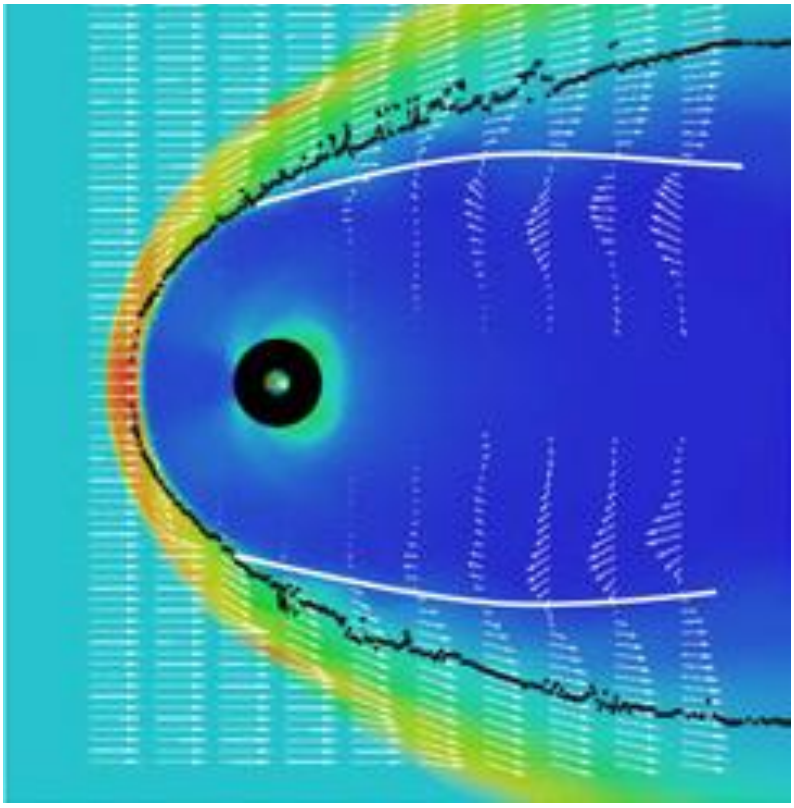

Figure 1-23 LFM global MHD simulation in the equatorial plane, color-coded for density, showing the LLBL flow associated with the viscous interaction [figure 6 from *Bhattarai & Lopez* (2013)].

Due to the rarefied nature of the plasma populations involved, it cannot possibly be attributed to viscosity; however, the interaction exhibits a similar nature to a viscous interaction. The dynamics of slowly evolving flows may change suddenly which eventually destroy the flow patter – this process is usually attributed to an instability (a disturbance imposed on a stationary state that grows exponentially) [Biskamp, 2003].

Since this viscous-like interaction is driven by a velocity shear (the shocked solar wind of the magnetosheath dragging past the stationary plasma in the LLBL), the instability responsible is the Kelvin-Helmholtz instability. MHD simulations have confirmed that the Kelvin-Helmholtz instability is the responsible mechanism [Claudepierre et al., 2008].

Of the two mechanisms, magnetic merging and the viscous interaction, the former is the more dominant mechanism. Yet, there are situations where the viscous interaction could be a greater contribution to the transfer of energy and momentum. This happens when the IMF is directed more in the east-west direction.

1.7 Current Systems in the Magnetosphere

1.7.1 Chapman-Ferraro Current

The first of three main current systems in the magnetosphere is the magnetopause current. As the magnetopause separates regions of different plasma populations and different magnetic fields, there must be a current system along the magnetopause, as per Ampère's law. Figure 1-24 shows a meridional plane of the magnetosphere with the currents drawn. On the dayside magnetosphere, the current flows in the *+Y* direction (out of the page). Just above outside the cusp regions, there is a neutral point where the currents change direction before the magnetotail is reached.

This magnetopause current system is known as the Chapman-Ferraro current. The Chapman-Ferraro current provides the $\boldsymbol{J} \times \boldsymbol{B}$ force that balances the solar wind dynamic pressure. As such, the Chapman-Ferraro current shapes the magnetosphere.

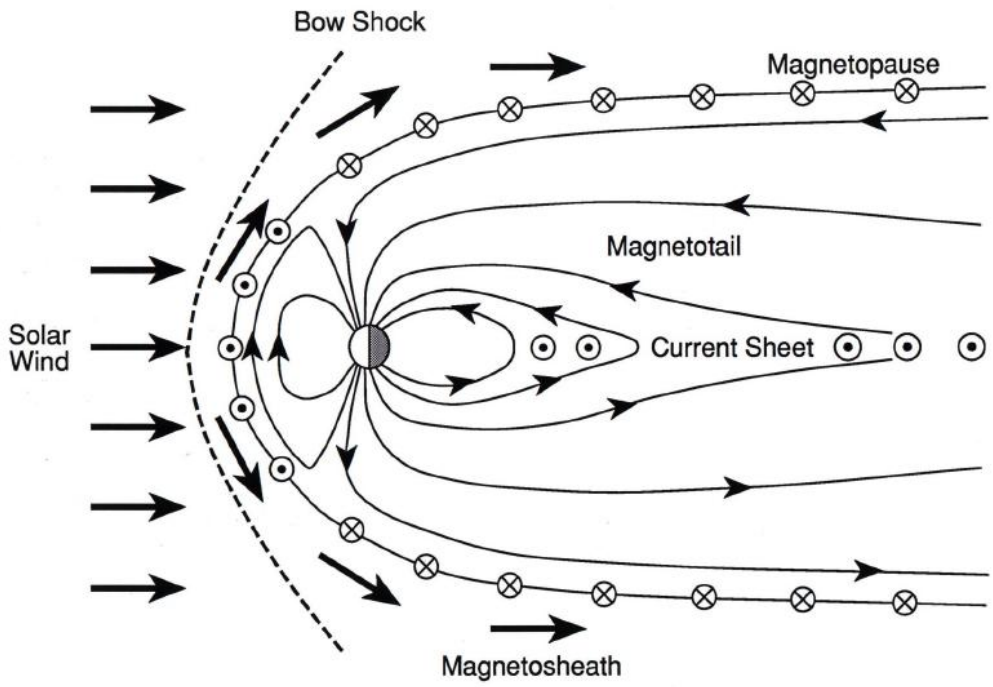

Figure 1-24 Meridional plane of the magnetosphere with current systems [*Hughes* (2016)].

1.7.2 Cross-tail Current

In keeping with the theme of Ampére's law, recall that the neutral sheet (from figure 1-17) is the roughly equatorial area in the magnetotail that separates the magnetotail lobes, and the lobes contain Earth's open dipole field lines – each lobe with oppositely directed field lines. If the lobes contain oppositely directed field lines, there must also be a current through this area. This current is the cross-tail current, and it flows from the dawn side to the dusk side and connects with the magnetopause currents at the LLBL. Figure 1-24 shows this current in the current sheet.

Figure 1-25 has a better perspective of the currents in the magnetosphere. The dayside magnetopause shows the eastward Chapman-Ferraro currents, which extend towards both magnetotail lobes.

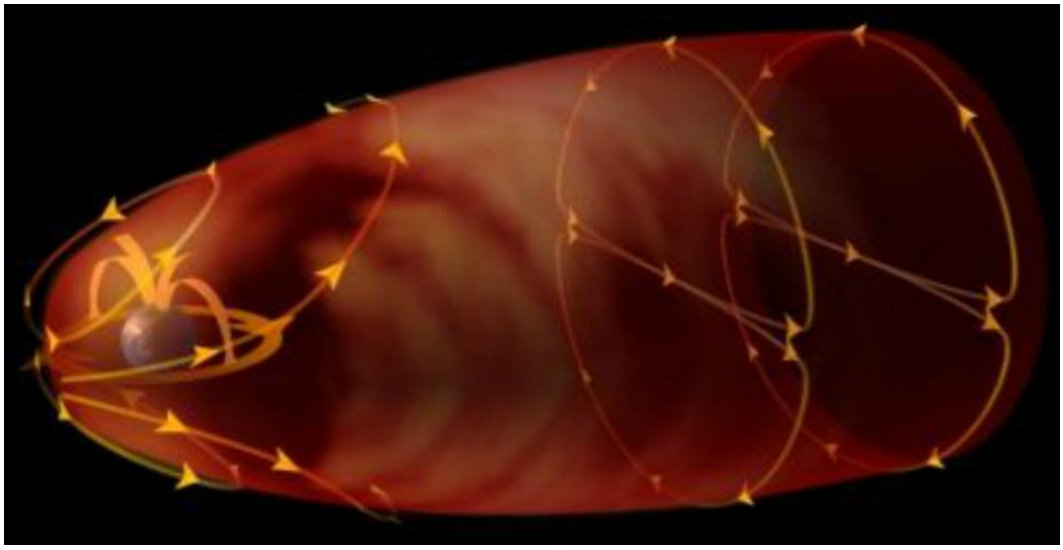

Figure 1-25 Illustration of currents in the magnetopshere [adapted from The Comet Program ©, NCAR/HAO].

1.7.3 Ring Current

A third current system in the magnetosphere is the ring current. As plasma convects towards Earth, the presence of electric and magnetic fields cause charge-dependent drifts. These drifts separate out the electrons and ions. Near Earth, the ions move westward (clockwise as viewed from the North Pole) and the electrons move eastward. This creates a net current encircling Earth known as the ring current. Figure 1-26 gives a perspective view of the terrestrial magnetosphere with the associated currents. The ring current is shown in the equatorial region near Earth's plasmasphere (pink shaded region). A better view of the Chapman-Ferraro and cross-tail currents are also shown in the figure.

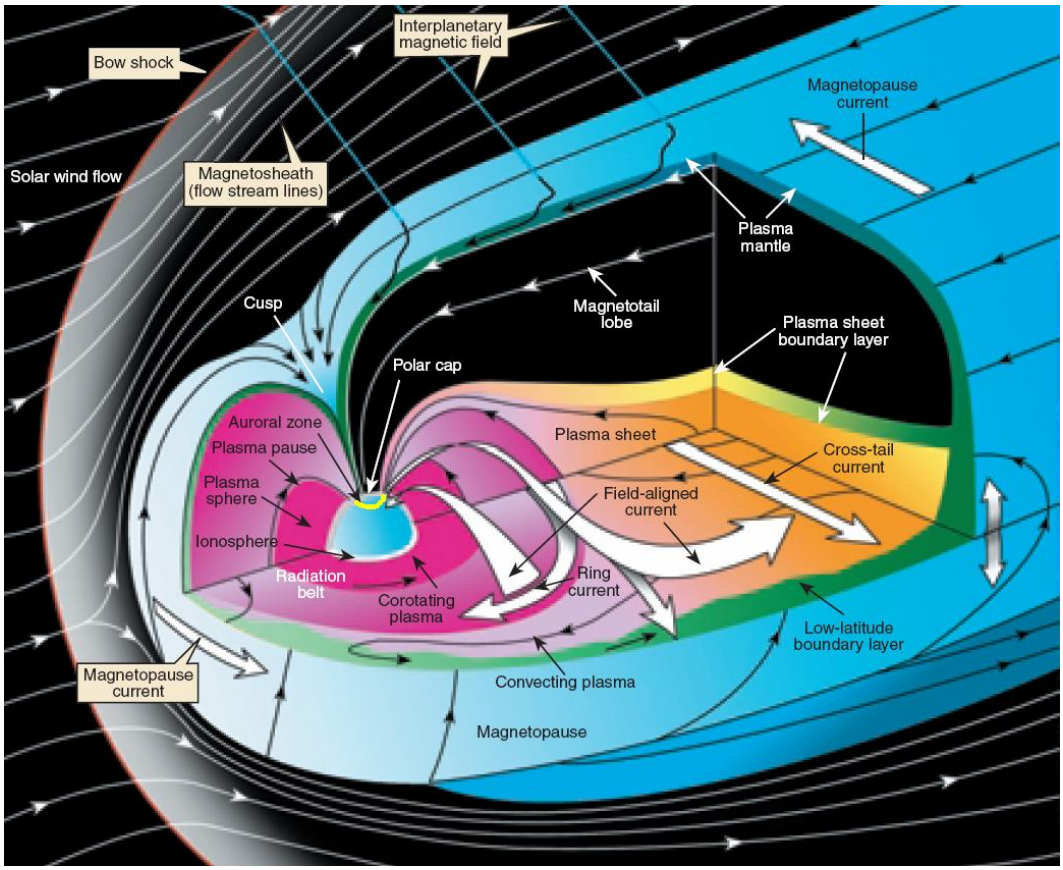

Figure 1-26 Perspective view of Earth's magnetosphere with associated currents [Figure 1 from *Brandt et al*. (2005)].

1.8 Ionosphere

The ionosphere is a region of the upper atmosphere (embedded mostly in the thermosphere) in which ionized gas plays a significant role. Its lower limits, about 70 km above Earth's surface, is in the upper mesosphere, and it extends to about 1 500 km up in the lower limits of the exosphere. The area is ionized by solar radiation which leaves an abundance of electrons that makes the region electrically conducting. The ionosphere is coupled to both the neutral atmosphere and the magnetosphere. The aurora, the only visible manifestation of space weather, occurs in the ionosphere.

1.8.1 Currents in the Ionosphere

1.8.1.1 Birkeland Currents

The way that the ionosphere couples to the magnetosphere is through the current systems. The first of these currents are the field-aligned currents. These are currents that flow along Earth's magnetic dipole field lines into the ionosphere. The field-aligned currents are referred to as Birkeland currents and are broken into two regions with opposing polarities: Region 1 and Region 2 (see figure 1-27).

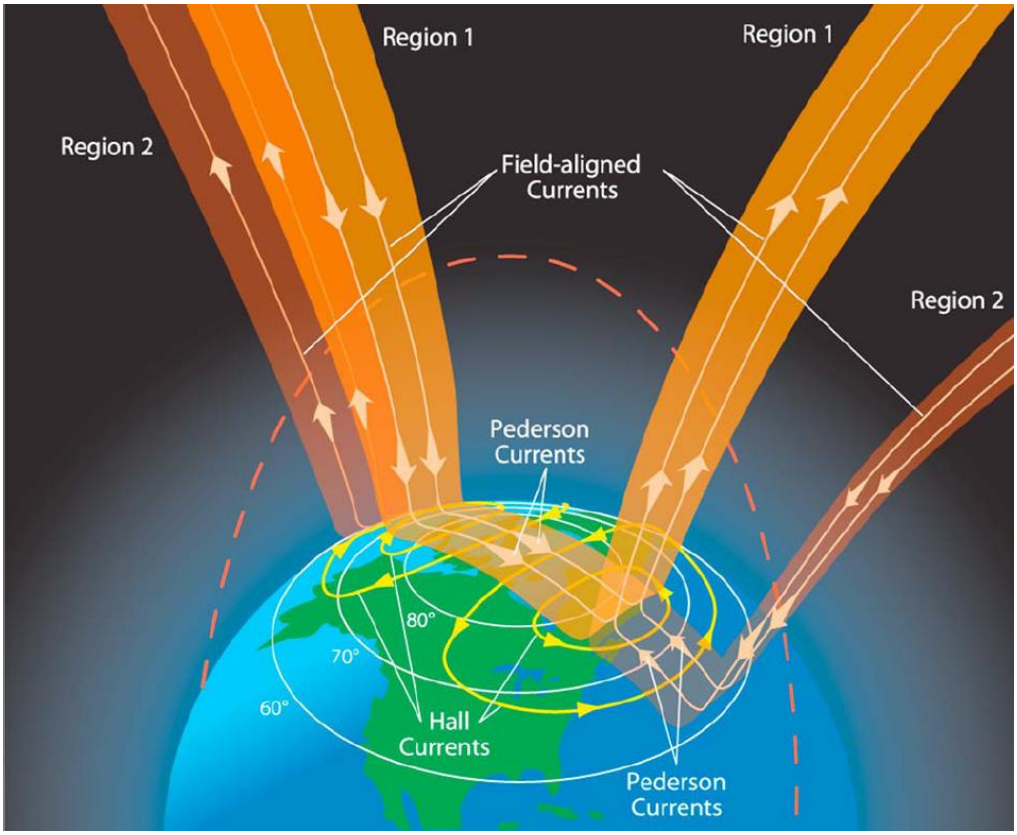

Figure 1-27 Diagram of the ionospheric current systems [figure 1 from *Le et al.* (2010)].

The Region 1 Birkeland currents occur at high latitudes and flow into the dawn and out of the dusk. Region 1 currents are driven mostly by southward IMF merging and the viscous interaction. Region 2 Birkeland currents occur at lower latitudes and have opposite polarity to Region 1 currents: into the dusk and out of the dawn. The Region 2 currents are driven by plasma pressure gradients in the inner magnetosphere [Vasyliunas, 1970].

The Chapman-Ferraro currents and the cross-tail currents map to and close through the ionosphere via the Region 1 Birkeland currents. Magnetic stress is delivered to the ionosphere which causes plasma to move and thus producing an electric field, in the frame of reference of Earth [Vasyliunas, 2001].

1.8.1.2 Pedersen Currents

Pedersen currents are carried by ions in the direction of the ionospheric electric field and are perpendicular to the Birkeland (field-aligned) currents. The Pedersen currents connect the Region 1 and Region 2 Birkeland currents that are mapped to the ionosphere. The Pedersen currents are shown in figure 1-27.

1.8.1.3 Hall Currents

Hall currents, also shown in figure 1-27, are perpendicular to both the ionospheric electric field (aligned with the Pedersen currents) and the (field-aligned) Birkeland currents. The two-cell convection pattern shown in figure 1-27, with anti-sunward flow at very high latitudes, is characteristic of southward IMF merging or due to the viscous interaction. Plasma in the ionosphere will circulate along the direction of the Hall currents. For northward IMF merging, the Hall currents take on a four-cell convection pattern, shown below in figure 1-28.

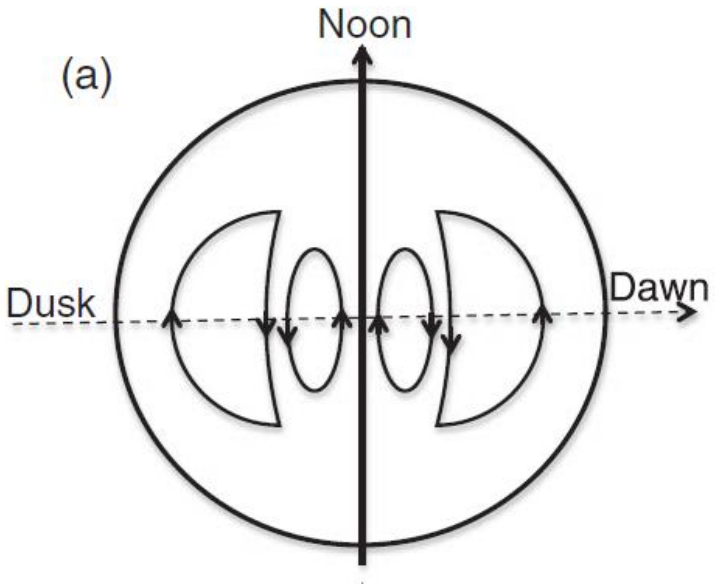

Figure 1-28 Schematic of the four cell Hall current convection pattern [figure 2a from *Bhattarai & Lopez* (2013)].

1.8.2 Transpolar Potential

Integrating the aforementioned ionospheric electric field will produce an associated ionospheric potential – this potential is referred to as the transpolar potential (TPP). It is defined as the difference between the maximum ionospheric potential and the minimum ionospheric potential ($\Phi_{\mathrm{TPP}} = \Phi_{\mathrm{MAX}} - \Phi_{\mathrm{MIN}}$). The TPP is also referred to as the polar cap potential (PCP) or sometimes, the cross-polar cap potential (CPCP). It is a combination of the effects of both magnetic reconnection and the viscous interaction.

Figure 1-29 shows an ionospheric model output for the northern hemisphere (Weimer model) on November 30, 2016. The red shows the maximum ionospheric potential and the blue is the minimum. In this case, the TPP would be $\Phi_{\mathrm{TPP}} = 42.6\ kV$. The TPP is often used as a proxy for convection in the magnetosphere and is therefore an important part to the research presented here.

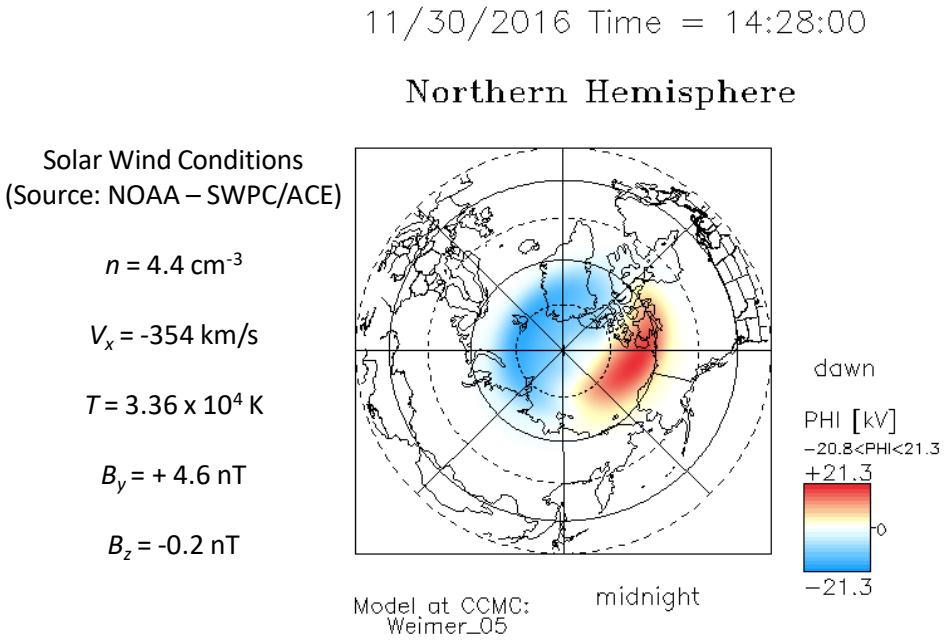

Figure 1-29 Weimer ionospheric model output [NASA/CCMC].

1.9 Motivation for Research

The more our society advances technologically, the more our infrastructure will extend into the geospace environment. A caveat to this is that our space-based infrastructure becomes susceptible to space weather. Just as terrestrial weather is the state of the conditions in the troposphere, space weather refers to the state of the conditions in the geospace environment. Nowadays, an extreme space weather event could have drastic consequences on any industry that uses GPS or any kind of satellite data. The aviation industry is especially susceptible.

Extreme space weather events can have destructive impacts not just on our space-based infrastructure, but ground induced currents can cripple power systems. This was the case on Easter Sunday, 1940, when a magnetic storm disrupted power in the regions

of New England, Pennsylvania, Minnesota, Ontario, and Quebec [Carlowicz & Lopez, 2002].

In October of 2015, The National Science and Technology Council released two reports that highlighted the effects space weather could potentially have on our infrastructure and economy [National Science, 2015a,b]. The next year, President Obama signed *Executive Order No. 13,744, 81 FR 71573* (2016) to coordinate efforts to prepare the United States for space weather events. This was in conjunction with the aforementioned reports by the National Science and Technology Council.

The goal of this research is to further our ability to predict the geospace response to atypical conditions. Using models to run simulations is a primary way this is done. As Michael J. Carlowicz and Ramon E. Lopez (2002) put it, “Models have changed the way physicists see the invisible realm of the magnetosphere.” Model development and accuracy is crucial for forecasting space weather because forecasting requires a greater reliance on models [Freeman, 2001].

Previous work using MHD modeling has mostly concentrated on steady state conditions for the model predictions; however, solar wind conditions and the geospace response are highly dynamic. Figure 1-30 shows solar wind data from June 5, 2012 (Z components for the magnetic field, B_z, on the top panel and velocity, V_z, on the bottom panel).

It can be seen that solar wind conditions are not constant for very long, thus the motivation to include fluctuations into the MHD simulations. The research focused on two main effects: the response of the viscous interacton to velocity fluctuations and the response of the subsolar magnetopause to IMF fluctuations.

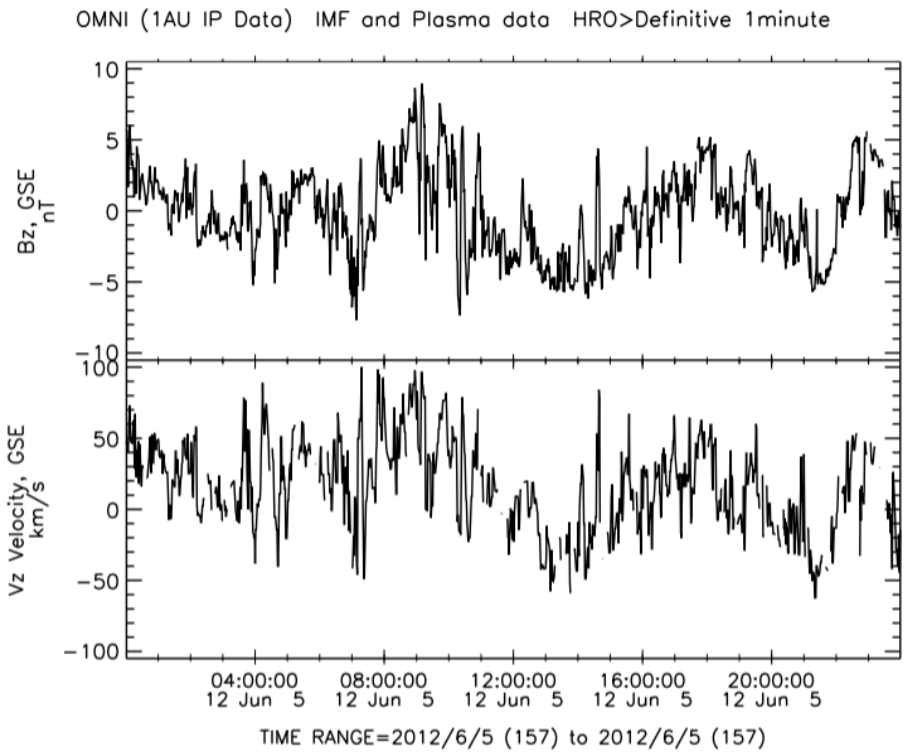

Figure 1-30 Solar wind data from OMNI for June 5, 2012 [NASA/GSFC/CDAWeb/OMNI].

1.10 Preview for the Rest of This Dissertation

Chapter 2 will cover in detail the Lyon-Fedder-Mobarry global MHD simulation used for this research. Chapter 3 covers the viscous interacton's response to velocity fluctuations in the *Y* and *Z* planes. Chapter 4 will switch to how fluctuations, particularly in the IMF, effect the subsolar magnetopause position. Due to the difficult nature in finding the magnetopause position for nowrthward IMF, chapter 4 is devoted to solely southward IMF conditions. Chapter 5 is the culmination of the work on the previous two chapters: the simulation of a high-speed stream. Chapter 6 summarizes this work and discusses the possible directions this research could take.

Chapter 2

The Lyon-Fedder-Mobarry Global MHD Simulation

While there is increasingly more discussion of how crowded space is, be it satellites or space junk, the fact of the matter is that near-Earth space is vast. It is exceptionally impractical to have enough satellites in the near-Earth environment from which to extract data. While there are a few satellites that have enough eccentricity to traverse the dayside magnetopause and bow shock regions [e.g. MMS, THEMIS], they only cover a diminutive amount of the magnetosphere. Consequently, there is a substantial need for global MHD simulations that can provide a global picture of the magnetosphere.

The MHD simulation used in this work is the LFM (Lyon-Fedder-Mobarry) global MHD simulation [Lyon et al., 2004]. LFM was developed in 1985 and has proved to be one of the most successful MHD codes since then. It has successfully modeled geomagnetic storms (e.g. Goodrich et al., 1998; Lopez et al., 2007), geomagnetic substorms (e.g. Wiltberger et al., 2000), and has the ability to successfully predict other magnetospheric events (e.g. Lopez et al., 1999; Bruntz et al., 2012b; Wiltberger et al., 2012).

2.1 The Ideal MHD Equations

LFM solves the three-dimensional, time-dependent, collisionless single-fluid ideal MHD equations. The ideal MHD equations take the following form [Chen, 2006]:

$$\frac{\partial \rho}{\partial t} + \nabla \cdot (\rho \boldsymbol{u}) = 0 \tag{2.1}$$

$$\rho\left(\frac{\partial \boldsymbol{u}}{\partial t}+\boldsymbol{u}\cdot\nabla\mathbf{u}\right)=-\nabla\cdot\boldsymbol{p}+\boldsymbol{J}\times\boldsymbol{B} \tag{2.2}$$

$$\nabla\times\mathbf{B}=\mu_0\mathbf{J} \tag{2.3}$$

$$\frac{\partial \boldsymbol{B}}{\partial t}=-\nabla\times\boldsymbol{E} \tag{2.4}$$

$$\boldsymbol{E}+\boldsymbol{u}\times\boldsymbol{B}=0 \tag{2.5}$$

where ρ is the plasma proton density, $\boldsymbol{u}$ is the plasma velocity, $\boldsymbol{P}$ is the plasma pressure, μ_0 is the permeability of free space, $\boldsymbol{E}$ is the electric field, and $\boldsymbol{B}$ is the magnetic field. These equation represent the standard hydrodynamic equations modified by Maxwell's equations.

Equation 2.1 is the continuity equation; equation 2.2 is the momentum equation; equation 2.3 is Ampère's Law; equation 2.4 is Faraday's Law; and equation 2.5 is the ideal Ohm's Law, which is also the frozen-in flux condition.

The ideal Ohm's Law comes about from assumptions made about the generalized Ohm's Law [Baumjohann & Treumann, 1997],

$$\boldsymbol{E}+\boldsymbol{u}\times\boldsymbol{B}=\eta\boldsymbol{J}+\frac{1}{ne}\boldsymbol{J}\times\boldsymbol{B}-\nabla\cdot\boldsymbol{P_e}+\frac{m_e}{ne^2}\frac{\partial \boldsymbol{J}}{\partial t} \tag{2.6}$$

where η is the resistivity, e is the elementary charge, m_e is the electron mass, $\boldsymbol{P_e}$ is the electron pressure, and n is the number density. For spatial and time scales in an MHD

grid, the last three terms on the right-hand side of equation 2.6 can be neglected. The generalized Ohm's law is then reduced to,

$$\sigma(\boldsymbol{E} + \boldsymbol{u} \times \boldsymbol{B}) = \boldsymbol{J} \tag{2.7}$$

However, we consider the plasma to be infinitely conducting and therefore Ohm's law reduces to equation 2.5 (known as the hydromagnetic approximation).

In addition to the ideal MHD equations, it is necessary to introduce an equation of state. The equation of state used for LFM is the adiabatic approximation,

$$\frac{d}{dt}(p\rho^{-\gamma}) = 0 \tag{2.8}$$

where γ is the ratio of specific heats.

2.2 LFM Simulation Boundary and Grid

The details of how the LFM code solves the MHD equations, including items like the conservative form of the MHD equations, the use of the *Boris* (1970) correction in regions of large Alfvén speeds, and other numerical techniques like the partial donor method of *Hain* (1987) to suppress oscillations in the 8th order finite difference scheme used by the LFM code, are all discussed in detail in *Lyon et al*. (2004) and are not directly germane to this dissertation. The grid used by LFM is a different matter that deserves some attention here.

LFM solves the ideal MHD equations on a logically orthogonal, non-adaptive, distorted spherical meshed grid. The choice of the LFM grid space allows finer grid points in areas of specific interest (e.g. bow shock, magnetopause, near Earth space)

and more spaced out grid points in areas that doesn't require a higher density of grid points (e.g. upstream solar wind and magnetotail). This spacing of grid points can be seen in figure 2-1, which shows an equatorial cut plane of the LFM grid.

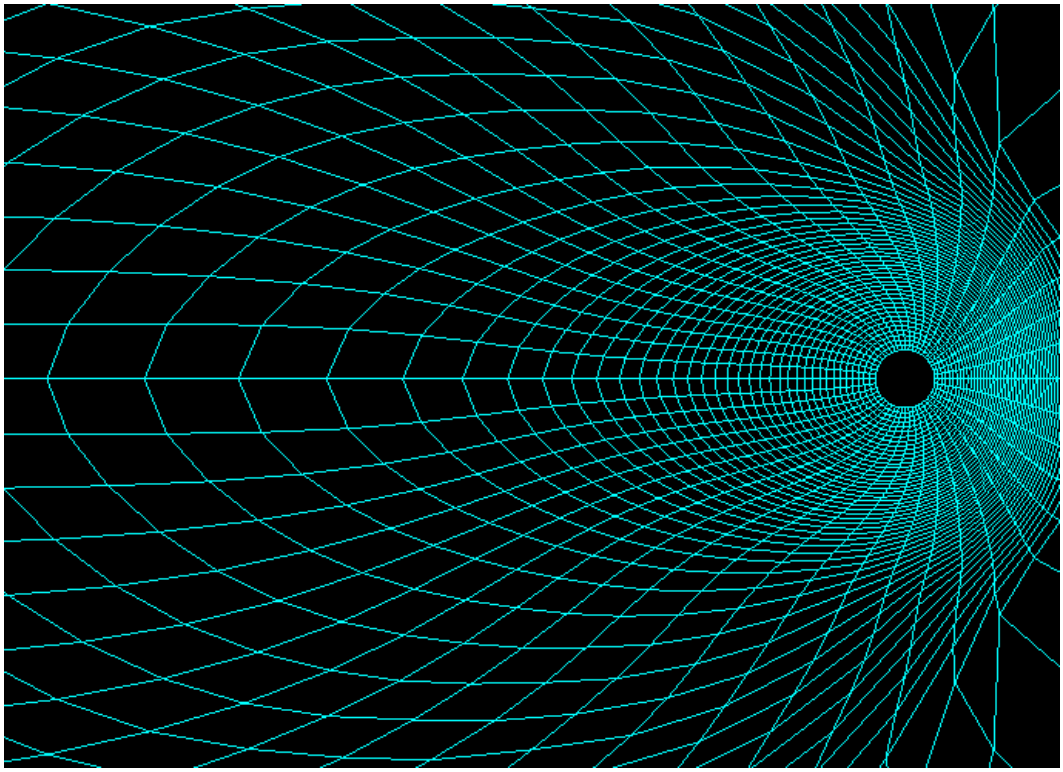

Figure 2-1 Equatorial cutplane of the LFM grid [*Wiltberger* (2016)].

The grid spacing in the areas of interest listed above is roughly 0.25 R_E and the grid spacing outside of this is anywhere from 1.0 to 1.5 R_E.

The LFM grid space starts at 30 R_E upsteam and extends to -350 R_E down the magnetotail, in the *X* direction. The grid space is then cylindrically wrapped around the *X* axis with a radius of *Y*, *Z* < 130 R_E. The three-dimensional LFM cylinder grid space is

presented in figure 2-2. Additional pictures of the LFM grid space can be seen in figures 2-3 & 2-4 at the end of the chapter.

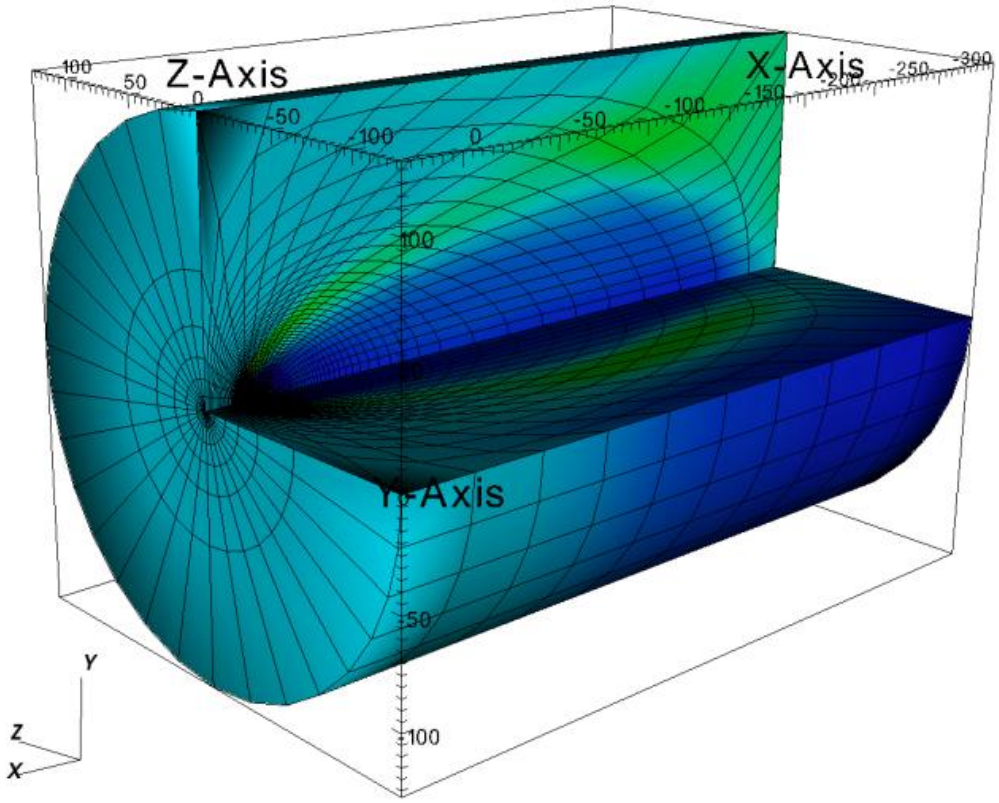

Figure 2-2 Three-dimensional LFM Grid Space [UCAR].

The origin of the grid space is at the center of a geocentric sphere with a radius of about 2.5 R_E. The inner boundary of the LFM simulation is at the radius of this geocentric sphere. Below about 2-3 R_E, there is a rapid increase in the Alfvén speed as the altitude decreases [Raeder, 2003; Lyon et al., 2004]. The simulation time step is restricted to the speed of the fastest wave in the simulation such that the wave does not travel to the adjacent cell during that time step. Therefore, an inner boundary less than 2-3 R_E would lead to very short and unfeasible time steps. The outflow condition at the back of the boundary (magnetotail) is supersonic. It is far enough downstream that the

flow is super-Alfvénic and thus it is impossible for the downstream boundary to affect the upstream plasma.

The lowest possible grid resolution (named “single resolution”) is 53 grid points in the radial direction, 24 grid points in the latitudinal direction, and 32 grid points in the azimuthal direction. This version can be run on 8 processors. Most of the work presented here was done with “double resolution”, which is 53x48x64 and requires 24 processors. Due to the time step restriction mentioned before, the time step also needs to be reduced by 4. This leads to a computational penalty of 16 times that of “single resolution.”

Another aspect that is specifically addressed in the LFM simulation is $\boldsymbol{\nabla} \cdot \boldsymbol{B} = 0$. Due to numerical error, there are instances when there will be a finite $\boldsymbol{\nabla} \cdot \boldsymbol{B}$. *Powell et al.* (1999) dealt with this problem by adding a $-\boldsymbol{\nabla} \cdot \boldsymbol{B}$ term to equations 2.2 and 2.4. This cancels out the effects in MHD equations but was still left with non-physical forces arising along magnetic field lines [Lyon et al., 2004]. The LFM code addresses this problem by using a TVD (total variation diminishing) algorithm with cell-centered quantities for the propagation of the plasma. This, along with the use of the *Yee* (1966) grid, is considered the best approach to keeping $\boldsymbol{\nabla} \cdot \boldsymbol{B} = 0$ to within roundoff error.

2.3 Ionosphere Simulation

Another aspect of the LFM simulation is the ionosphere. The ionosphere is biggest recipient of magnetospheric energy and must be included [Lyon et al., 2004]. The LFM simulation is really two linked simulations in one: the magnetosphere and the ionosphere. At the inner boundary of the magnetospheric simulation described above, the field aligned currents (Birkeland currents) are mapped instantaneously along dipole field lines into the ionosphere. The ionosphere is considered to be a thin, conducting

spherical shell (such that $E_{\parallel} = 0$). From here, these currents, and the ionospheric conductivity, are used in a two-dimensional ionospheric simulation.

Once the currents are mapped to the ionosphere, the transpolar potential (TPP) is obtained by solving the height integrated current continuity equation (the divergence of the horizontal current given by Ohm's Law is equal to the Birkeland current coming into or out of the ionosphere), which is the basis for magnetosphere/ionosphere coupling [Wolf, 1983; Goodman, 1995]:

$$\nabla \cdot (\Sigma \cdot \nabla \Phi) = j_{\parallel} \sin\delta \tag{2.9}$$

where Φ is the TPP (to be solved for) and δ is the dip angle. For uniform conductance, this reduces to a simple Poisson equation. The conductivity tensor, Σ, is given by:

$$\Sigma = \begin{pmatrix} \frac{\Sigma_P}{\cos^2 \delta} & -\frac{\Sigma_H}{\cos \delta} \\ \frac{\Sigma_H}{\cos \delta} & \Sigma_P \end{pmatrix} \tag{2.10}$$

where Σ_P is the Pedersen conductivity and Σ_H is the Hall conductivity. The Pedersen conductivity and associated currents are perpendicular to the magnetic field but parallel to the electric field, while the Hall conductivity and associated currents are perpendicular to both the electric and magnetic fields (see figure 1-27).

Once a solution for the TPP (and thus, the electric field) is found, it is mapped back to the inner boundary and used to define the boundary conditions for the plasma velocity [Wiltberger et al., 2000]. The plasma velocity is found through the following equation:

$$\boldsymbol{V} = \frac{-\boldsymbol{\nabla}\Phi \times \mathbf{B}}{B^2} \tag{2.11}$$

The two-dimensional ionospheric simulation in LFM has two components:

1. Idealized (constant and uniform) conductance
2. Semi-empirical model that uses the $F_{10.7}$ value.

The $F_{10.7}$ value is a measure of the Sun's total emission at a wavelength of 10.7 cm. It is taken at the center of the epoch, which is one hour [Tapping, 2013]. It is measured in SFU (solar flux units). 1 SFU = 10^{-22} W m^{-2} Hz^{-1}. The ionosphere model in either case can cover co-latitudes of 30^o, 44^o, or 60^o. It has been found that there is little to no difference between 44^o or 60^o, so the results presented in this work were all done at 44^o.

The ionspheric conductance is extremely difficult to measure. Estimations using models put the ionospheric conductance anywhere from 2 S to 8 S [Vickrey et al., 1981; Lilensten et al., 1996; Aksnes et al., 2005; Aikio & Selkälä, 2009]. This averages out to 5 S. The average 5 S is considered to be the standard condition for Pedersen conductance in ionospheric models [e.g. Kamide & Richmond, 1982]. However, when a constant 5 S Pedersen conductance is used in LFM, the resulting TPP is higher than realistic values [e.g. Merkine et al., 2003; Lopez et al., 2010; Bruntz et al., 2012a,b]. *Lopez et al.* (2010) found that a constant Pedersen conductance of 10 S was more in agreement with realistic TPP values. Even the empirical ionosphere model in LFM was predicting TPP values too high [e.g. Wiltberger et al., 2012]. This problem of inflated TPP values is not isolated to the LFM simulation as others have found a similar problem [e.g. Raeder et al., 1998].

LFM is a non-dissipative simulation, which means that magnetic reconnection is not explicitly built into the code; however, the effects of finite cell size allow for an equivalent of magnetic reconnection to take place. When oppositely directed magnetic fields are convected into a computational cell, the numerical averaging in the cell results in the annihilation of the magnetic flux [Wiltberger et al., 2000]. This "forced reconnection" happens only in areas where numerical resistivity is important (e.g. magnetopause or the reconnection point in the magnetotail plasmasheet). *Fedder and Lyon* (1987) and *Fedder et al.* (1995) found that the reconnection rate was controlled by the physical boundary conditions rather than the numerical method. The TPP, which is an indirect measure of the global reconnection rate, had little variation with grid size, meaning that the grid resolution does not affect the reconnection rate [Wiltberger et al., 2000].

2.4 LFM Inputs and Initialization

The LFM simulation takes the solar wind parameters shown in table 2-1. All magnetic field values inputted to LFM are the IMF values and B_x does have some restrictions on it [Wiltberger et al., 2000].

Time Step (min)	n (cm^{-3})	V_x (km/s)	V_y (km/s)	V_z (km/s)	C_s (km/s)	B_x (nT)	B_y (nT)	B_z (nT)	B (nT)	Tilt (deg)

Table 2-1 LFM solar wind parameters.

The solar wind parameters can either be idealized and used with the uniform Pedersen conductance model or *in situ* observations (e.g. from ACE or DSCVR) and used with the empirical ionosphere. The LFM input must be done in the SM (Solar

Magnetic) coordinate system. This is the same coordinate system as described in section 1.4, albeit with the dipole axis aligned with the *Z* axis (see figures 1-15 & 1-16). A dipole tilt may be added as the last parameter in table 2-1 but most studies done with LFM do not include a dipole tilt [e.g. Lopez et al., 2007; Wiltberger et al., 2000; Wiltberger et al., 2003]. Therefore, the results presented here were done with a zero degree dipole tilt. Furthermore, the sound speed was held constant at 40 km/s.

LFM requires a 50 minute spin-up time to precondition the magnetosphere before the user's solar wind conditions are injected into the grid. This is done with the following solar wind conditions: V_x = -400 km/s, n = 5.8 cm-3, C_s = 35 km/s, and zero IMF. After the 50 minute spin-up time, there is a four hour initialization period to inject plasma into the LFM magnetosphere. The initialization period starts with 2 hours of the following solar wind conditions: V_x = -400 km/s, n = 5 cm-3, C_s = 40 km/s, and IMF B_z = -5 nT. It is followed by another 2 hours of the same conditions, except the IMF is changed to B_z = 5 nT. The initialization must be built into the solar wind file whereas the spin-up condition is automatically configured when submitting a run. Therefore, the user's solar wind conditions start at minute 241. When using *in situ* solar wind conditions from satellite data, there is no initialization. It is therefore recommended to run LFM 12 hours before the event you wish to model.

The user's solar wind conditions enter the LFM grid such that these conditions propagate and reach the center of Earth (X = 0) at the start of the user's solar wind conditions (minute 241). The output in LFM of cell-centered quantities are: proton density, plasma velocity, sounds speed, and magnetic field. The magnetic flux is along the face of the cell and the other edge quantities are the electric field and the grid coordinates.

Since LFM has been in development since the 1980s, there have been several updates to LFM. The most current version of LFM, and the one used in this work, is LFM-MIX (LFM-Magnetopshere/Ionosphere Coupler/Solver). This incorporates the same LFM simulation with a more realistic model for the ionosphere. The details of which can be found in *Merkin and Lyon* (2010).

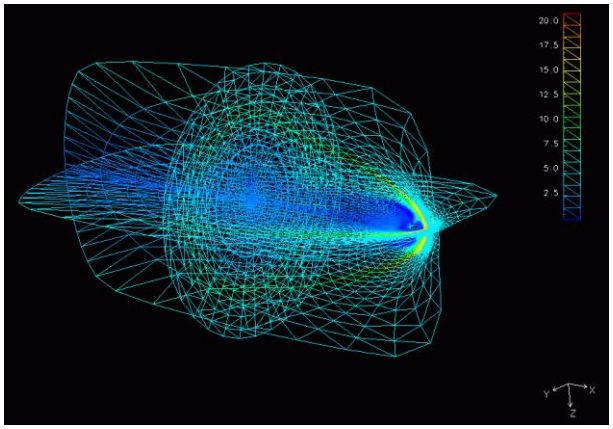

Figure 2-3 Three cutplane view of the LFM grid color-coded for density. The grid points are connected by lines.

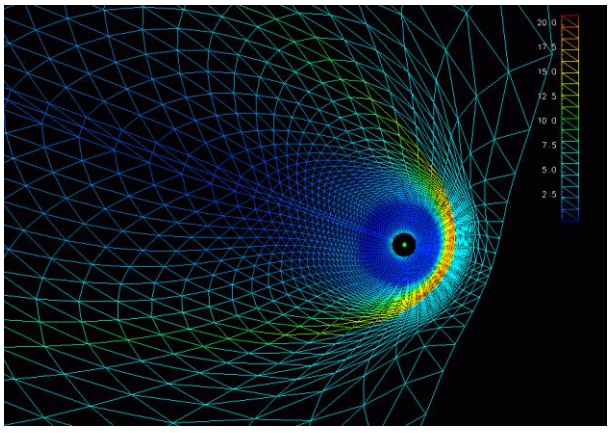

Figure 2-4 Equatorial cutplane view of the LFM grid color-coded for density. The grid points are connected by lines.

Chapter 3

The Effect of Velocity Fluctuations on the Viscous Interaction

3.1 Transpolar Potential

The first part of this study was to examine how solar wind velocity fluctuations impact the viscous potential (described in chapter 1.6.2) and thus, the transpolar potential. The TPP is an indicator of the coupling strength between the solar wind and the magnetopause [Shepherd, 2007, and references therein]. As described in chapter 1.8.2, the TPP is a combination of the contributions to both magnetic reconnection and the viscous interaction.

Reiff et al. (1981) tested various models to try and explain the TPP in terms of solar wind parameters. The study found that magnetic reconnection could not account for (35 ± 10) kV of the TPP. The TPP can be linearly separated, for small driving, into the contributions of both reconnection and the viscous interaction: $\Phi_{TPP} = \Phi_R + \Phi_V$ [Lopez et al., 2014]. The unaccounted value of the TPP found by *Reiff et* al. (1981) could come from the viscous interaction. A study by *Boyle et al*. (1997) found a functional dependence of Φ_V on the solar wind bulk flow velocity in the form, $10^{-4} V^2$. A subsequent study by *Newell et al*. (2008) found that a viscous term also depends on the plasma density and that the functional form $n^{1/2} V^2$ provided the best fit of the functions tested, but this formula was not a functional fit to the data.

There have been several studies that have confirmed a potential due to the viscous interaction and have put a value on it anywhere from 15 kV to 35 kV [e.g. Burke et al., 1999; Shepherd et al., 2003;]. Global MHD models have also confirmed the existence of this potential [e.g. Watanabe et al., 2010], although the effect was never studied in detail until *Lopez et al.* (2010) and especially *Bruntz et al*. (2012a,b).

There are empirical methods for measuring the TPP: low-altitude satellite passes [e.g. Hairston et al., 1998], backscattering radar signals such as SuperDARN [e.g. Shepherd & Ruohoniemi, 2000], and assimilative mapping from data sources such as the AMIE model [Ridley & Kihn, 2004]. The problem with measuring the TPP is that it contains both contributions from magnetic reconnection and the viscous interaction. The contribution due to magnetic reconnection is significantly larger than the contribution due to the viscous interaction. The IMF is never small enough, for long enough, to really study the viscous interaction independently. This is where global MHD models can greatly aid in our understanding of the viscous interaction as we can control the input solar wind parameters.

3.2 The *Bruntz et al.* (2012a,b) Study on the Viscous Interaction using LFM

A study conducted by *Bruntz et al*. (2012a,b) explored the viscous interaction in detail using LFM. This study found a functional dependence that worked the best for the viscous potential as a function of the solar wind density and bulk flow velocity: $\Phi_{\mathrm{V}} = (0.00431)\, n^{0.439}\, V^{1.33}\, kV$, which is very close to the *Newell et al*. (2008) formula. The *Bruntz et al*. (2012a) formula was tested over the Whole Heliosphere Interval (WHI). This interval was Carrington rotation 2068 (20 March – 16 April 2008) and it was selected by a team of scientists to coordinate modeling and observation efforts [Echer et al., 2011]. The *Bruntz et al*. (2012a) formula did very well predicting the value of the TPP for the WHI (to within 10%) [Bruntz et al., 2012b].

The *Bruntz et al*. (2012a) study used two methods for determining the TPP solely due to the viscous interaction. The first method was called the “extrapolation method.” This involved running LFM for a series of southward IMF values, fitting a linear regression, and taking the intercept to be the viscous potential. This method is sufficient

since the viscous interaction occurs concurrently and independently of magnetic reconnection [Bruntz et al., 2012a and references therein] and therefore the viscous potential will not be affected by the southward IMF.

The results for n = 5 cm^{-3} and V_x = -400 km/s in the *Bruntz et al*. (2012a) study are presented in figure 3-1. LFM was run from 0 nT to -5 nT and then fit with a linear regression. The intercept, interpreted as the contribution to the TPP from the viscous interaction, is shown to be about 26 kV. This puts it in the range of values that were previously discussed.

The second method used by *Bruntz et al*. (2012a) was the “zero IMF method”, in which LFM was run with zero IMF conditions. With zero IMF, the TPP due to magnetic reconnection would be zero and the value of the TPP output would be solely due to the viscous interaction. This method produced a TPP of about 27 kV for the same solar wind parameters as in figure 3-1. The study took a range of solar wind densities and bulk flow velocities and found that both the “extrapolation method” and the “zero IMF method” were consistent.

The study completed by *Bruntz et al*. (2012a) used steady state conditions over a range of plasma densities and bulk flow velocities to extract the formula shown above. But, as shown in figure 1-30, the solar conditions are never steady for very long. The work presented in this dissertation was to extend the study done by *Bruntz et al*. (2012a) to include the effects of velocity fluctuations

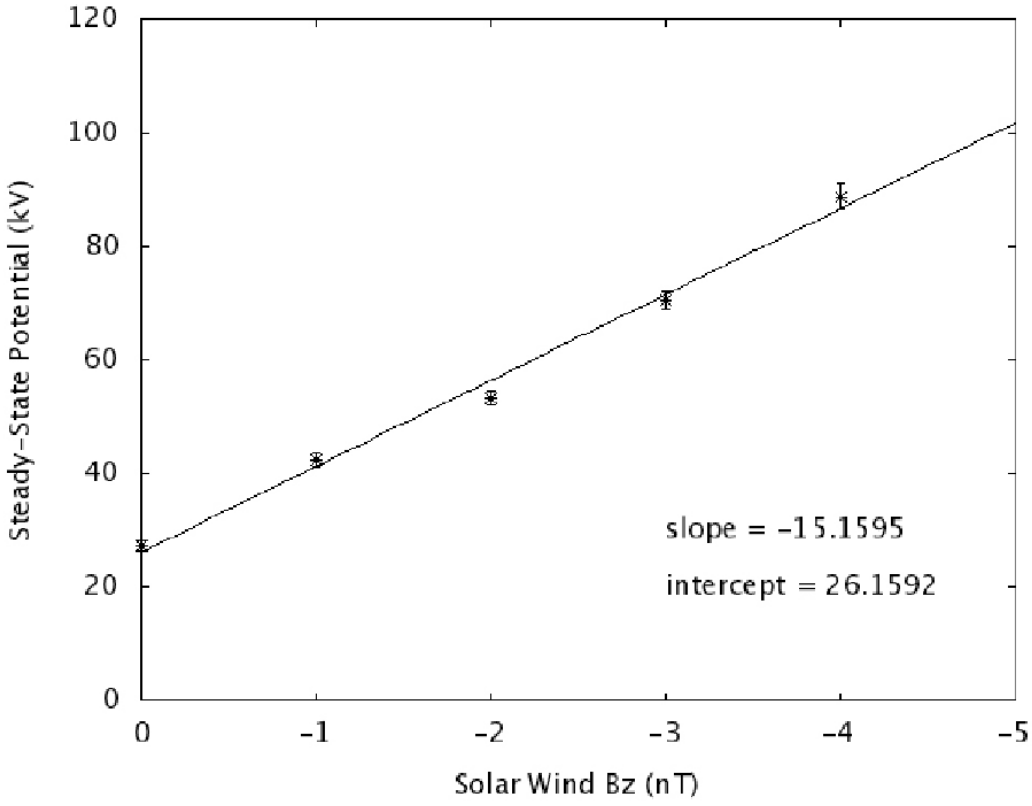

Figure 3-1 TPP as a function of IMF B_z, results from LFM with n = 5 cm^{-3}, V_x = -400 km/s, and 10 S for the uniform ionospheric conductivity [figure 4 from *Bruntz et al*. (2012a)].

3.3 The Addition of Velocity Fluctuations to the *Bruntz et al.* (2012a,b) Study

The velocity fluctuations were concentrated in the *Y* and *Z* directions as the *Bruntz et al*. (2012a,b) study simulated a range of velocities in the *X* direction. The initialization was the same as described in chapter 2. For simplicity, the fluctuations in the *Y* and *Z* directions took the form of a sine wave. At 04:01 ST (simulation time), the following solar wind velocity conditions started,

$$\vec{V} = -400\frac{km}{s}\hat{x} + V_{Y/Z}\sin\left(\frac{2\pi}{T}\,[t - 241\,min]\right)\hat{y}/\hat{z} \qquad (3.1)$$

where T is the period of oscillation and t is the time step in the simulation (in minutes). At minute 241, the user's solar wind conditions start in the simulation. The subtraction of 241 minutes from the t value in the sine wave was to ensure that at minute 241, V_z = 0 km/s. If the V_z amplitude (maximum displacement from the average value) was for example 30 km/s, with a period of 60 minutes, then V_z would reach a maximum value of 30 km/s at minute 271. The baseline (average value of the sine wave) was 0 km/s for all LFM runs. A reverse sine wave ($-V_z$) where the velocity would decrease after initialization rather than increase was tested for consistency and was found that it had no effect on the simulation (i.e. the results were symmetrical).

The same method was also done in the Y direction. All other solar wind parameters were kept constant: n = 5 cm^{-3}, C_s = 40 km/s, and zero dipole tilt. The "zero IMF method" from the *Bruntz et al*. (2012a) study was used such that the TPP output from the simulation was the viscous potential only. A range of V_z or V_y amplitudes and oscillation periods were tested. The uniform Pedersen conductance was set to 10 S for all LFM simulation runs with zero Hall conductance.

The first item that needed to be addressed was the consistency between the updated LFM-MIX code (what this study used) to the LFM version used in the *Bruntz et al*. (2012a) study. The two versions of LFM produced similar results, although the dependency on the solar wind plasma and bulk flow velocity changed slightly. The comparison between the two are shown in equations 3.2 and 3.3.

$$\Phi_{\mathrm{V}} = (0.00431)\, n^{0.439}\, V^{1.33}\, kV \qquad \textit{Bruntz et al}.\ (2012a)\ \text{LFM} \qquad (3.2)$$

$$\Phi_V = (0.000764)\, n^{0484}\, V^{1.576}\, kV \qquad \text{2016 using LFM-MIX} \qquad (3.3)$$

While the functional forms are slightly different, and the normalization constant seems quite different, actually the values of the potential for any given density and velocity are not too different. For example, for n = 5 cm^{-3} and V = 400 km/s, equation 3.2 yields 25.2 kV, while equation 3.3 yields 21.0 kV.

3.3.1 The Effect of V_Y Fluctuations on the Viscous Interaction

The first study conducted was the effects on the TPP of equatorial plane oscillations in the in the *Y*-direction (V_y). The results for a 30 km/s amplitude V_y oscillation with a period of 60 minutes are presented in figure 3-2. The dashed line is a steady state run with the same value as the amplitude of oscillation (in this case 30 km/s). The solid black line is with just V_x = -400 km/s and no V_y. There appears to be a slight reduction of the TPP from the steady state input with no V_Y compared to when there was a steady V_Y, which appeared throughout all the results. However, in the case of fluctuations in the V_Y velocity component, the overall potential did not change much, though a small (1-2 kV) modulation in the TPP is evident.

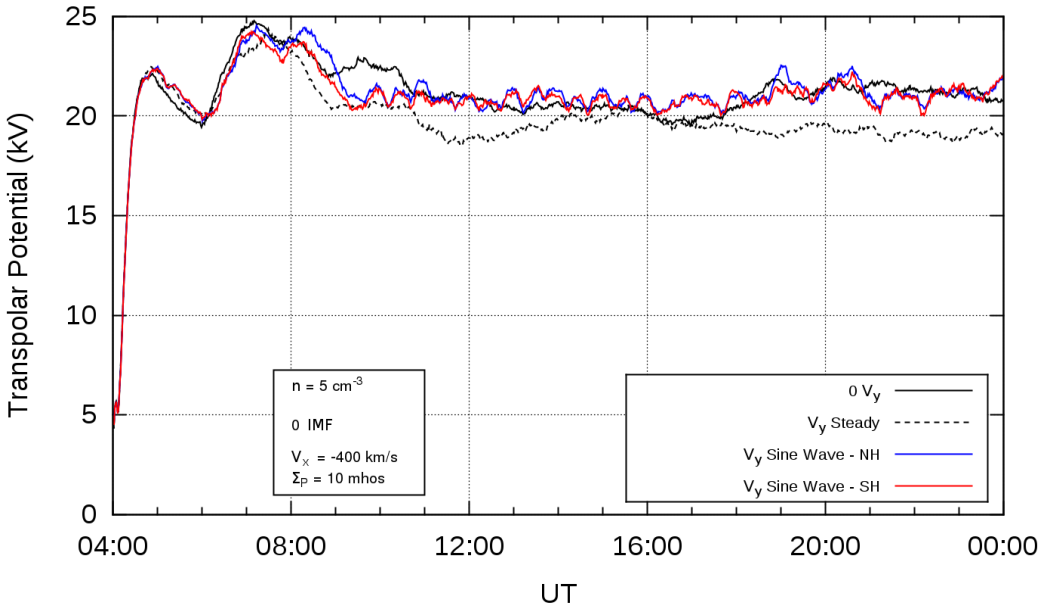

Figure 3-2 LFM-MIX TPP output for equatorial plane oscillations with a V_Y = 30 km/s amplitude and a 60 minute sine wave (blue is northern hemisphere and red is southern hemisphere). The dashed line is a constant V_Y = 30 km/s and the solid black line is a constant V_X = -400 km/s with 0 V_Y.

The blue and red lines in figure 3-2 are the TPP values for the northern and southern hemispheres, respectively. The first thing to notice is that there is a slight recovery from the steady state reduction to the TPP when oscillations are added. The TPP value with oscillations follows the 0 V_y line pretty well, albeit a little more erratic. There is no difference between the northern and southern hemisphere responses. The thing to notice most about equatorial oscillations is that for a sinusoidal solar wind input in the equatorial plane, there is no significant sinusoidal response in the TPP, though the small modulation is likely driven by the velocity fluctuations. Interestingly, the modulation has double the period of the velocity fluctuations. This is consistent with an east-west cycle in the velocity corresponding to two cycles of deviation from a pure V_Y.

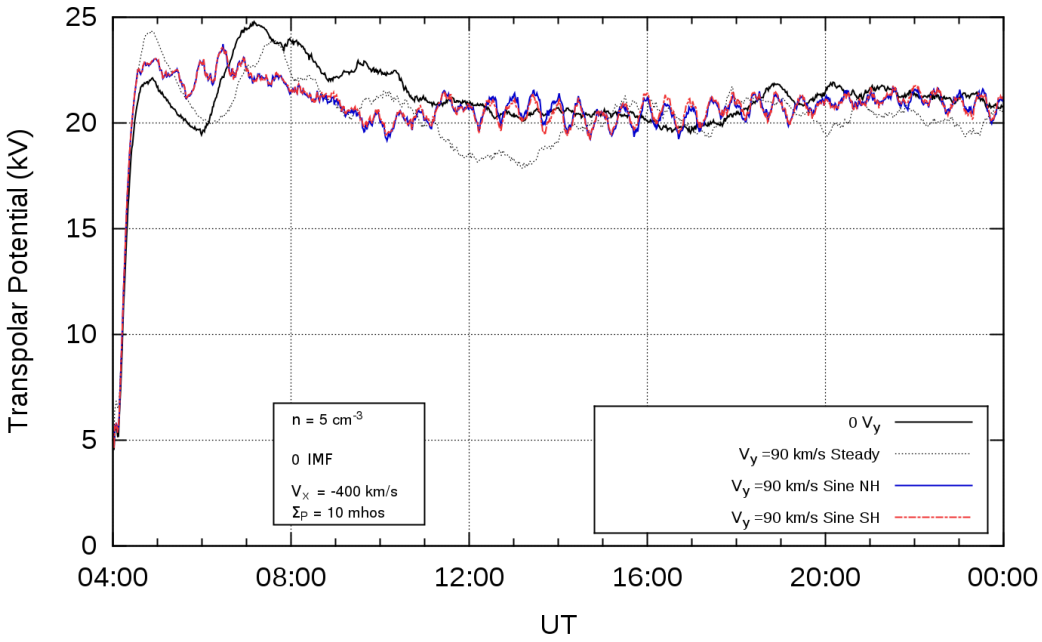

Figure 3-3 LFM-MIX TPP output for equatorial plane oscillations with a V_Y = 90 km/s amplitude and a 60 minute sine wave (blue is northern hemisphere and red is southern hemisphere). The dashed line is a constant V_Y = 90 km/s and the solid black line is a constant V_X = -400 km/s with 0 V_Y.

Figure 3-3 shows the output for a 60 minute sine wave with a 90 km/s amplitude in V_y. The difference between the two outputs is that a sinusoidal pattern emerges when the amplitude was increased to 90 km/s (the first such amplitude which shows a discernible sinusoidal TPP response). However, the period of the TPP output is one half the solar wind V_y input. Again, the variation of the absolute value of V_Y has two peaks (+/- V_Y) in one 60-miinute period, so that must be what is driving the small deviations in the TPP. The amplitude of the TPP response increases with increasing V_y solar wind input past 90 km/s. The period changes in the equatorial plane oscillations had no affect on the TPP response whatsoever.

3.3.2 The Effect of V_Z Fluctuations on the Viscous Interaction

The next step was to switch to meridional plane oscillations (V_z). The same method for equatorial plane oscillations was used. The results for a similar run to figure 3-2 (30 km/s amplitude and 60 minute sine wave) now in the meridional plane are presented in figure 3-4.

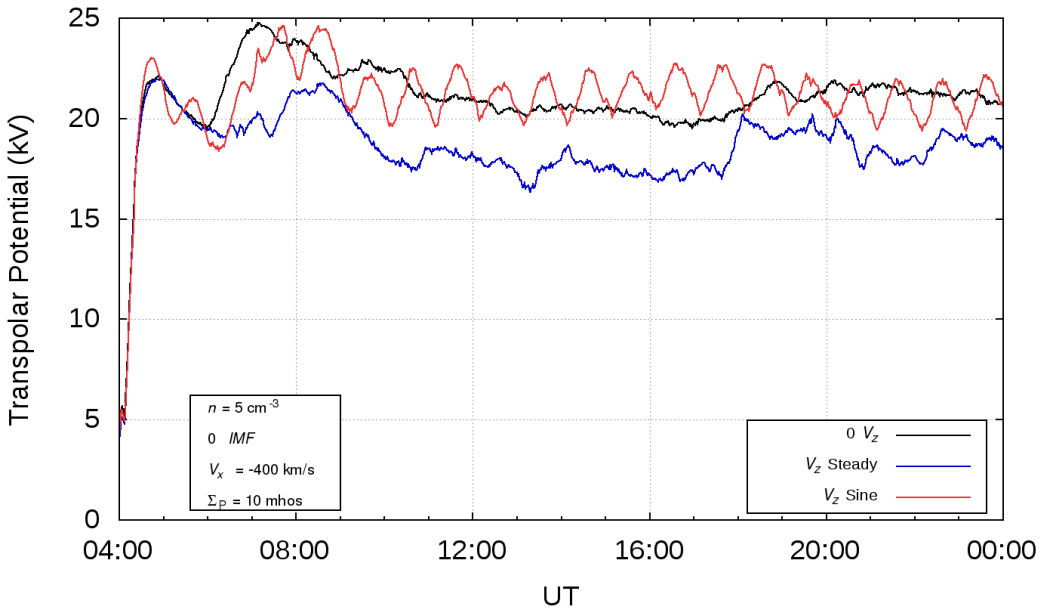

Figure 3-4 LFM-MIX TPP output for meridional plane oscillations with a V_Z = 30 km/s amplitude and a 60 minute sine wave (red line). The solid black line is a constant V_X = -400 km/s with 0 V_Z and the blue line is a constant V_Z = 30 km/s.

The most noticeable difference is the obvious sinusoidal response to the TPP (red line) from a sinusoidal V_z input, with the period equaling that of the input. This is quite different for the V_Y response, which had a signal at half the period. There is still the reduction of the TPP due to steady state input (blue line) and the recovery with oscillations (red line). An even more interesting result came from testing meridional plane oscillations: hemispheric favorability. Figure 3-5 shows the LFM-MIX TPP output

for both the northern hemisphere (blue line) and for the southern hemisphere (orange line). The figure shows that the TPP in each hemisphere is exactly out-of-phase to the response of meridional oscillations.

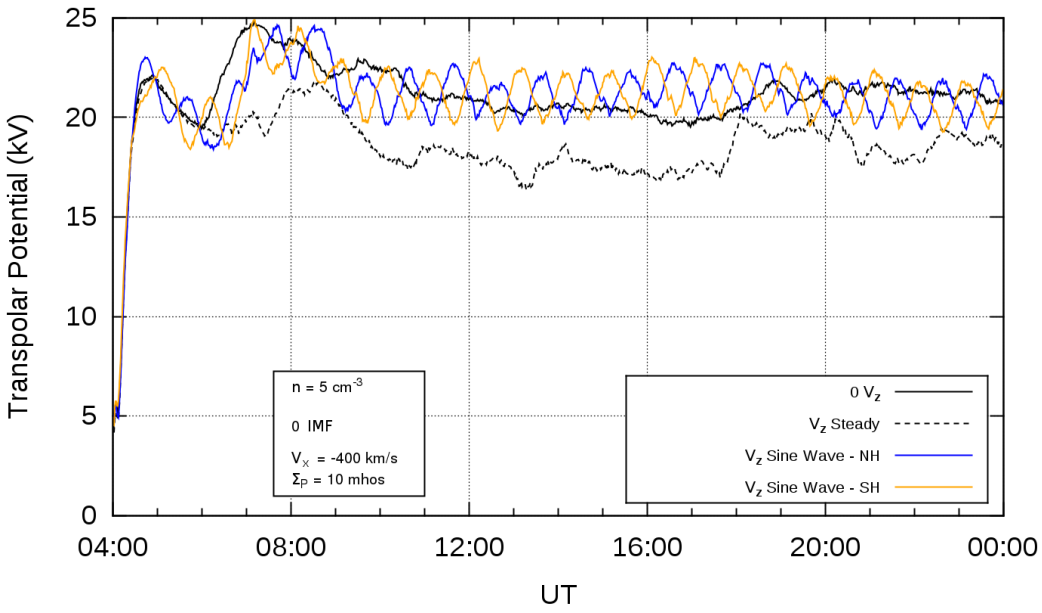

Figure 3-5 LFM-MIX TPP output for meridional plane oscillations with a V_Z = 30 km/s amplitude and a 60 minute sine wave (blue is northern hemisphere and yellow-orange is southern hemisphere). The dashed line is a constant V_Z = 30 km/s and the solid black line is a constant V_X = -400 km/s with 0 V_Z.

This hemispheric difference is interesting since the equatorial oscillations (figures 3-2 & 3-3) showed no favorability between hemispheres. A simulation with the V_z amplitude of 180 km/s was done and those results are presented in figure 3-6. The TPP amplitude response is noticeably larger, creating a large TPP difference between hemispheres.

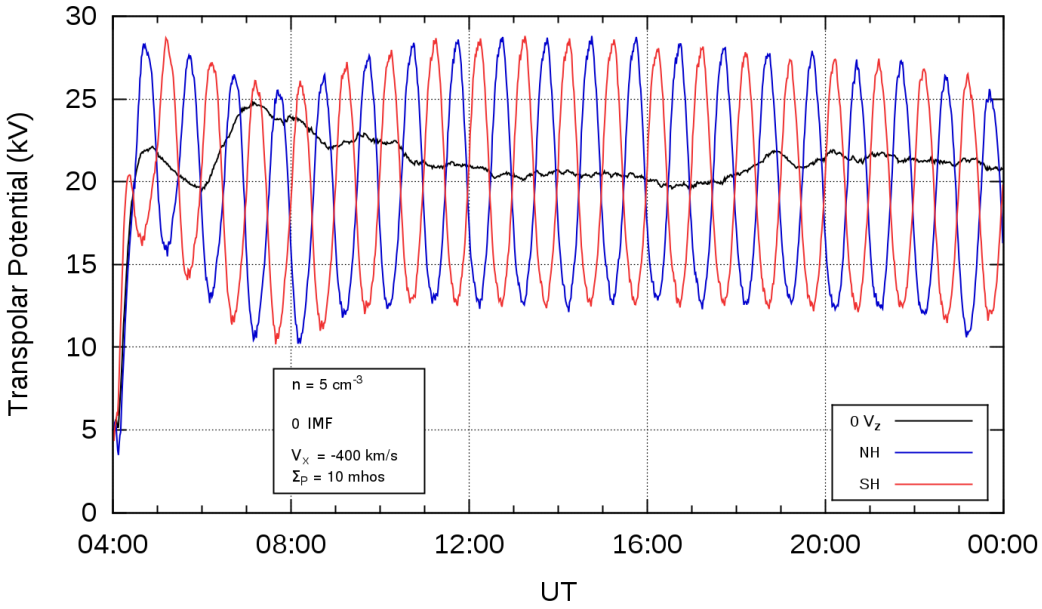

Figure 3-6 LFM-MIX TPP output for meridional plane oscillations with a V_Z = 180 km/s amplitude and a 60 minute sine wave (blue is northern hemisphere and red is southern hemisphere). The solid black line is a constant V_X = -400 km/s with 0 V_Z.

The magnetotail will align itself with the change in V_y or V_z, just like a wind sock. Figure 3-7 shows a one hour output using the ParaView visualization software in the meridional plane. The top panel (6 frames) is color-coded for (log) density in 10 minute increments. The magnetotail flaps up and down in response to the changes in V_z. The bottom panel (6 frames) is color-coded for V_x. The blue colors indicate antisunward flow, green is neutral, and red indicates sunward flow. The time lapse panels show that when the magnetotail is near the extreme positions in response to the maximum V_z input, there is a strong sunward (> 150 km/s) flow in either the northern or southern magnetotail lobes. This could account for the difference in the hemispheric response, although at this point, it is unclear how.

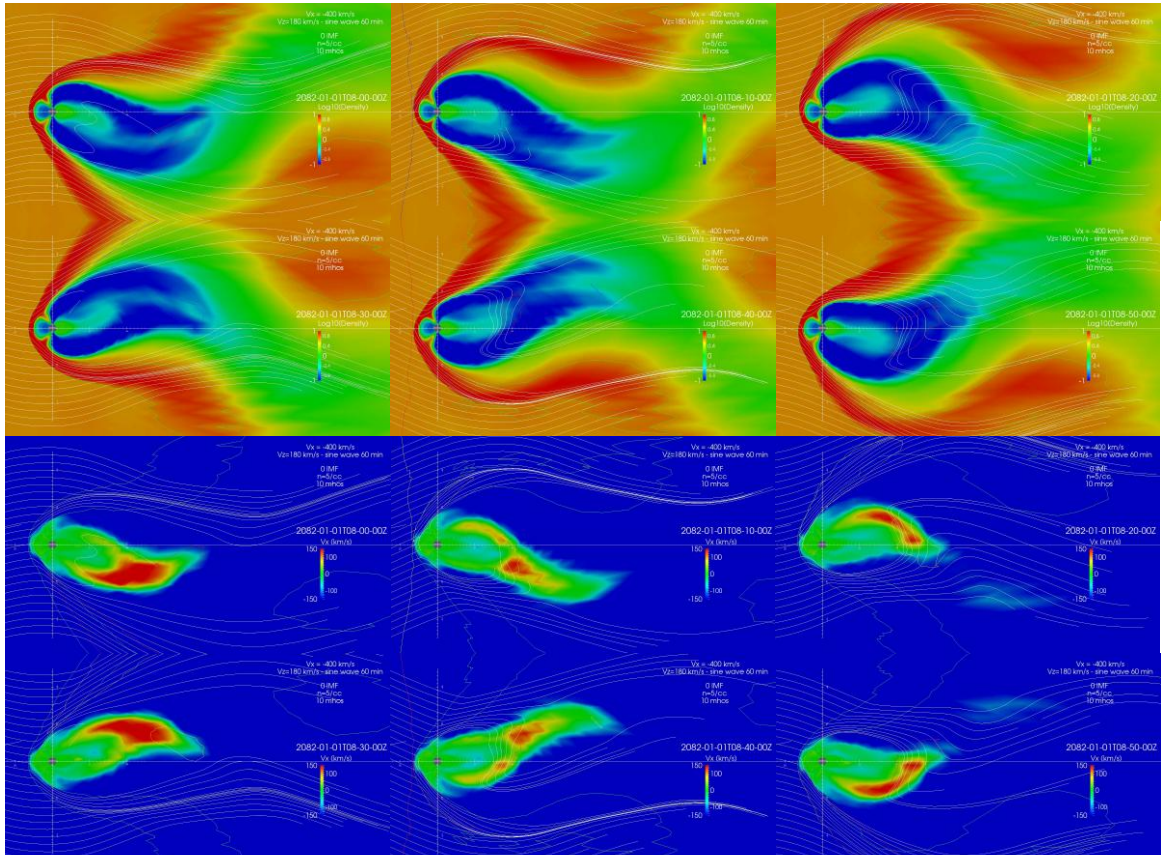

Figure 3-7 Time lapse of a ParaView output (over one hour) in the meridional plane for 180 km/s V_z amplitude and 60 min sine waves. The top panel (6 frames) is color-coded for solar wind plasma (log) density and the bottom panel (6 frames) is color-coded for V_x.

The changes in the TPP due to a change in the input solar wind V_z amplitude were linear, with the TPP changing about 1 kV for every 30 km/s of input V_z amplitude (see figure 3-8).

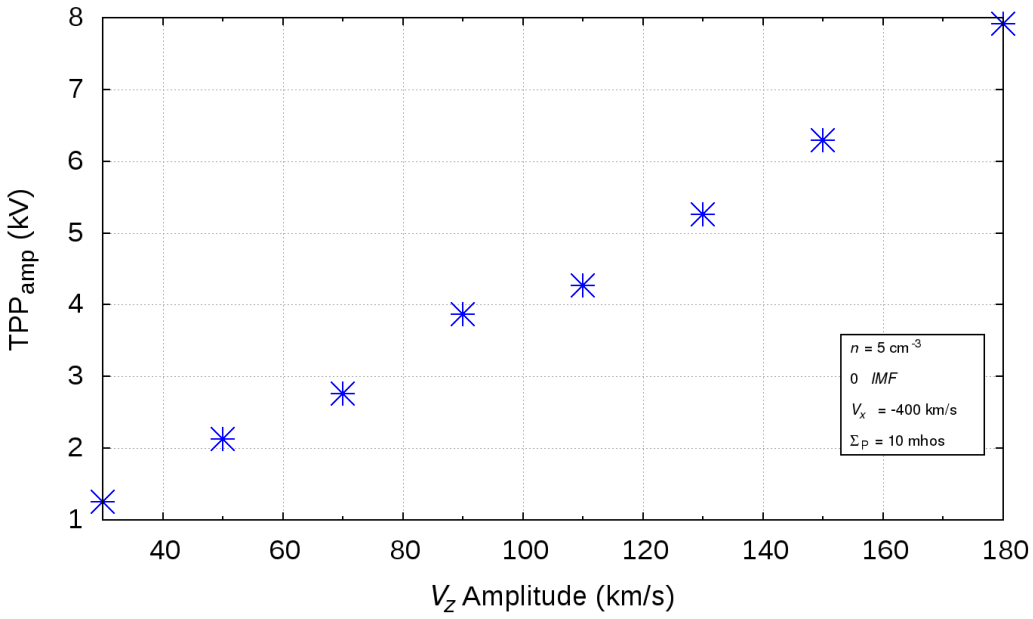

Figure 3-8 TPP amplitude response as a function of V_z input amplitude.

The oscillation period was also changed anywhere from 5 minutes to 4 hours. Although the TPP period response matched that of the V_z input period, there was no change in the TPP magnitude as a result of changing the V_z input period. Figure 3-9 shows the response to 30 min, 60 min, and 120 min sine waves. It is clear from the figure that the TPP period matches that of the V_z input period but the magnitude of the TPP does not change with changing input oscillation period.

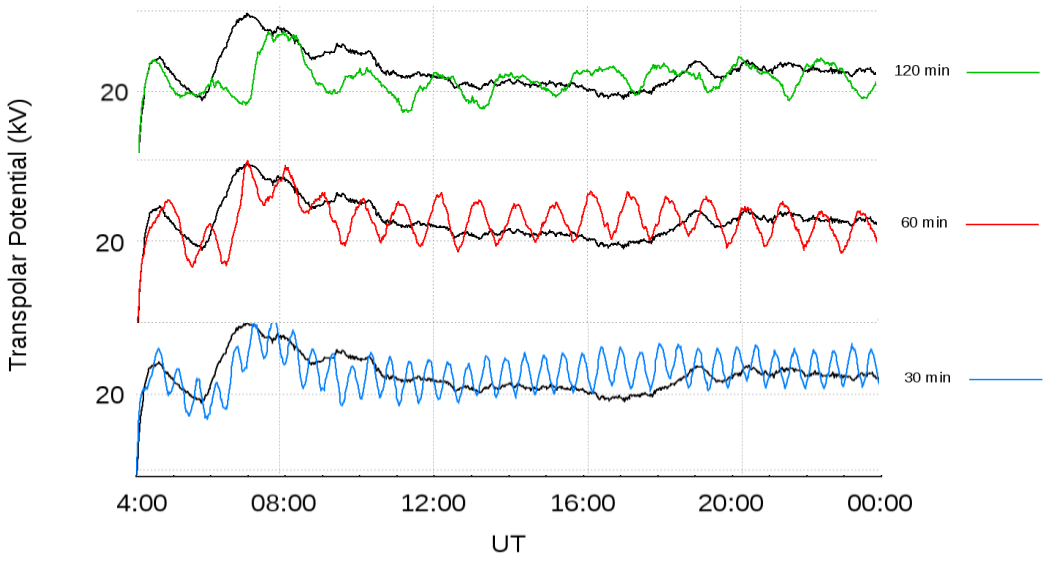

Figure 3-9 TPP response to changing oscillation periods in the meridional plane. The amplitude was 30 km/s. The color lines are TPP values with oscillations at the given oscillation period and the black line is with 0 V_z conditions.

Another study was done to see the effects of velocity fluctuations along with IMF fluctuations. The results of this study are presented in figure 3-10. Two simulations were run, one with a baseline of -1 nT in the input IMF B_z and the other used a 1 nT baseline in the input IMF B_z. Both runs used a 5 nT amplitude in the IMF oscillations. The input V_z correlation used was 10 km/s in V_z for every 1 nT in the input IMF B_z. The TPP responds just like V_z oscillations did, with a matching oscillation period output to the oscillation period input. The TPP response to IMF oscillations dominates the TPP response to the viscous interaction, as expected. The northward IMF TPP response (blue lines) is reduced compared to the southward IMF case (red lines). This is consistent with the results from *Bhattarai & Lopez* (2013) which showed a reduction in the TPP due to northward IMF. An interesting feature of figure 3-10 is that the response for each hemisphere is back in phase when IMF oscillations were added.

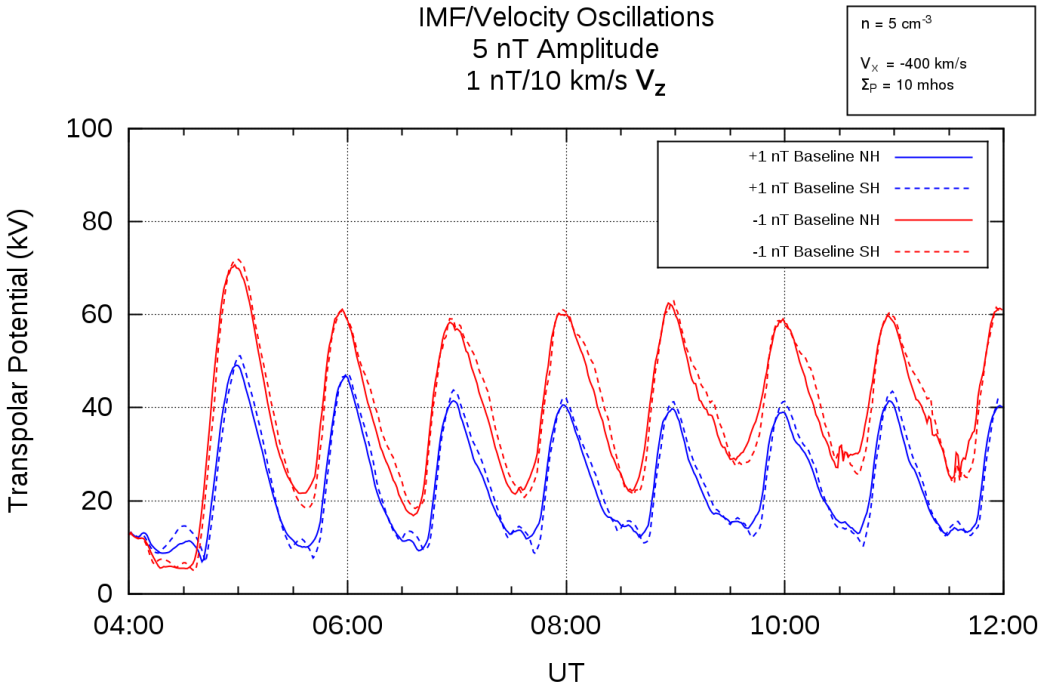

Figure 3-10 TPP response to a combination of both velocity and IMF fluctuations with 60 minute sine waves. The red lines are with a -1 nT southward IMF baseline and the blue line are with a 1 nT northward IMF baseline. The dashed lines are the southern hemisphere's response. The IMF amplitude of oscillation was 5 nT. The velocity oscillation was 10 km/s V_z for every 1 nT in IMF.

3.4 Conclusions

It is clear from the results presented here that the fluctuations in the meridional plane have much more effect than fluctuations in the equatorial plane. Although the TPP due to merging dominates the TPP due to the viscous interaction, the latter would be an important aspect in the effect velocity fluctuations have on the outer planets (Jupiter and beyond). The IMF on average is inclined about 45^{o} to the ecliptic at 1 AU [Kivelson & Russell, 1995]. Once the IMF has traveled say 9 AU, the distance to Saturn, that IMF

angle has been reduced significantly, such that the IMF is almost all in the equatorial plane (B_y), and therefore reconnection will not be a major driver of magnetospheric dynamics, except in rare instances [Masters et al., 2014]. The viscous interaction would then be the dominate mechanism for transferring energy and momentum to the magnetospheres of the outer planets.

Chapter 4

The Effect of Purely Southward IMF Fluctuations on the Subsolar Magnetopause

After the work on velocity fluctuations was complete, the research moved into investigating how IMF fluctuations would affect the TPP. While conducting this research, the AGU Chapman Conference was announced and the topic was going to cover dayside magnetosphere interactions. As a result, the focus of this work switched from how the TPP would respond to IMF fluctuations to how the dayside magnetosphere, in particular the subsolar magnetopause, would respond to IMF fluctuations. The results of this chapter were presented at this AGU Chapman Conference, which was held from July 10-14, 2017, in Chengdu, Sichuan Provence, China. The next year, the results were published in *Bonde et al*. (2018).

4.1 Magnetopause Erosion

The magnetopause position is an important space weather metric. Satellite operators have a vested interest in knowing when the satellite will exit the magnetosphere, especially if the satellite uses magnetic torquing for attitude control. It is also important for the planning of data taking requirements on a scientific mission such as MMS (Magnetospheric Multiscale) [Burch et al., 2016] or the upcoming SMILE mission (Solar Wind Magnetosphere Ionosphere Link Explorer) [Raab et al., 2016].

As discussed in chapter 1.5.2.1, the solar wind dynamic pressure is the single most important factor in the magnetopause position. Greater ram pressure from a faster flow will push the dayside magnetopause earthward. Observations have shown that the configuration of the magnetosphere changes depending on the direction of the IMF – in particular, for southward IMF B_z, the dayside magnetopause moves inward and the

nightside (magnetotail) magnetopause moves outward [Coroniti & Kennel, 1972]. Observational evidence also shows inward motion of the magnetopause for periods of southward IMF [e.g. Aubrey et al., 1970; Fairfield, 1971; Maezawa, 1974; Formisano et al., 1979; Rijinbeek et al, 1984]. This inward motion of the magnetopause, due to southward IMF, was referred to as magnetopause "erosion" by *Aubrey et al*. (1970). There are two theories as to why the magnetopause erodes.

The first theory proposed to explain erosion, as discussed (and rejected) by *Sibeck et al*. (1991) is referred to as the "onion peel" model. When southward directed IMF approaches Earth's northward directed dipole field, they merge near the subsolar magnetopause point, as described in chapter 1.6.1.1. The magnetic flux is then transported away from this merging line and dragged through the magnetosheath to the nightside, where reconnection happens again in the magnetotail, adding to the tail's magnetic flux. Layers of magnetic flux are "peeled" away from the dayside and are transported to the nightside. The problem with that model is that it does not preserve force balance at the magnetopause.

The second theory of magnetopause erosion was put forth by *Maltsev & Lyatsky* (1975). When the IMF is directed southward, there is an increase in the Birkeland Region 1 currents. These Region 1 currents produce fringe fields on the dayside that are oppositely directed to Earth's magnetic dipole, thus reducing the dayside magnetic field. The pressure balance equation (1.7) shows that under constant dynamic pressure, the magnetopause will move inward of the pressure balance point until the pressure balance has been reestablished. This model does preserve force balance at the magnetopause, and *Sibeck* et al. (1991) argued that it was consistent with the observations as well as theoretical considerations.

An extension to the *Maltsev & Lyatsky* (1975) theory was proposed by *Maltsev et al*. (1996). Their theory was that in addition to the Birkeland Region 1 current growth, the cross-tail current (described in chapter 1.7.2) growth also contributes to the reduction of the dayside magnetic field. Furthermore, they argued that it is the cross-tail current that has the most contribution to the reduction of the dayside magnetic field.

Knowing that the subsolar magnetopause position depends on the direction of the IMF, in addition to the dynamic pressure, magnetopause position models now reflect both aspects [e.g. Roelof & Sibeck, 1993]. A study comparing both models and observations found that the subsolar magnetopause position as a function of IMF B_z is nonlinear [Shue et al., 2001]. The LFM results for magnetopause erosion under steady solar wind inputs are presented in figure 4-1. The LFM simulation confirms magnetopause erosion and is fairly linear as a function of IMF B_z, until the magnitude exceeds 10 nT at which point saturation effects becomes apparent [Lopez et al., 2010].

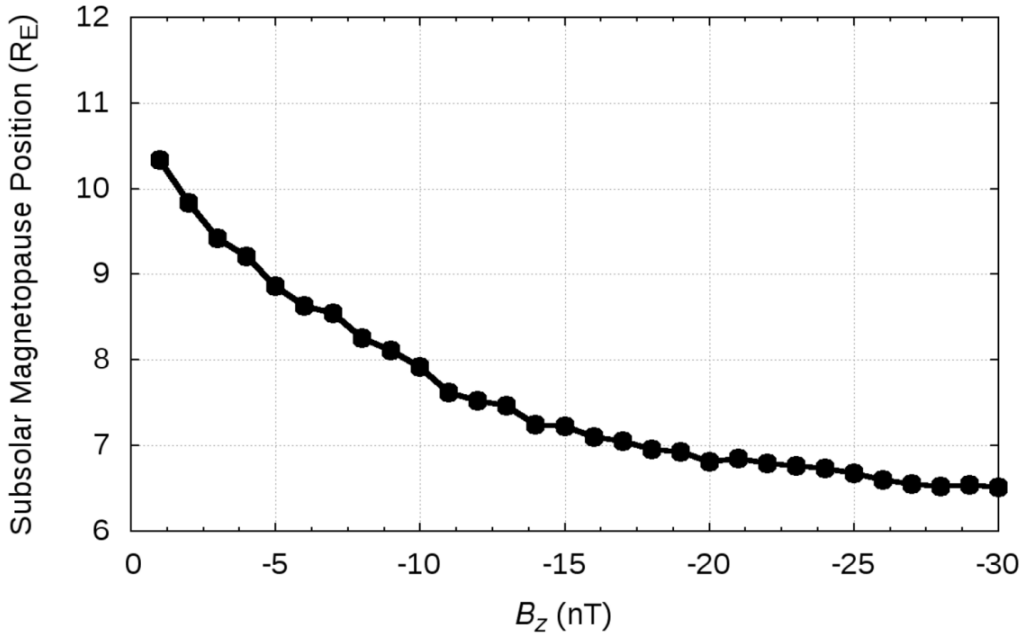

Figure 4-1 Magnetopause erosion in LFM under steady state solar wind input [figure 2 from *Bonde et al.* (2018)].

During intense storms, the magnetopause can move inward of geosynchronous orbit [Rufenach et al., 1989]. This could expose satellites to the harsh plasma environment of the magnetosheath. This was the case during the Halloween storms in 2003 [Lopez et al., 2007]. There have been many empirical models that have been developed to predict the magnetopause position [e.g. Formisano et al., 1979; Sibeck et al., 1991;, Petrinec & Russell, 1996; Shue et al., 1997,1998, 2001; Lin et al., 2010; Wang et al., 2013]. These models provide a magnetopause position through instantaneous solar wind parameters. As can be seen in figure 1-30, the solar wind, and thus the magnetopause position, is highly dynamic. Therefore, these models cannot fully represent the magnetopause motion with instantaneous inputs.

Previous MHD studies on magnetopause erosion have used steady state solar wind inputs [e.g. Palmroth et al., 2001; Lu et al., 2013]. While global MHD models contain enough physics to provide a more realistic representation of the dynamic geospace environment, using steady state solar wind inputs is not exhibitive of real solar wind conditions. This is most notable during a high-speed stream (HSS) where there are large amplitude Alfvén waves with $\delta \boldsymbol{B}/B > 1$ [Belcher & Davis, 1971]. To understand the magnetospheric response to a HSS, the time history of the solar wind must be considered [Denton & Borovsky, 2012].

4.2 The *Wiltberger et al.* (2003) Study on Magnetopause Erosion using LFM

An extensive study on magnetopause erosion using LFM was carried out by *Wiltberger et al*. (2003). The initialization of LFM in their study was similar to the description in chapter 2, with the exception that the initialization period is 6 hours. The first 3 hours is set to n = 5 cm^{-3}, V_x = -400 km/s, C_s = 40 km/s, and IMF B_z = 5 nT. The uniform ionospheric conductivity was set to 5 S. All other values were set to zero. At 0300 ST (simulation time), the IMF B_z was flipped to 5 nT while all other values were held the same as before. At 0600 ST, the IMF B_z was flipped back down to -5 nT and held constant for the rest of the simulation. A second simulation was run with a user input of -10 nT at 0600 ST.

The *Wiltberger et al*. (2003) study found a two-stage process of magnetopause erosion. Figure 4-2 shows the difference between the current B_z and the input B_z (taken at 0555 ST), for several values along the Sun-Earth (X) line. With the arrival of the southward IMF at 0600 ST, the Region 1 currents begin to grow. This is shown in the bottom panel of figure 4-2 as the immediate weakening of the noonequatorial magnetic field inside the magnetosphere. This is the first stage of magnetopause erosion.

The second stage of magnetopause erosion occurs at around 0620 ST. The nightside currents are shown decreasing at this time in the top panel of figure 4-2. This is associated with the growth of the cross-tail current, which weakens the dayside field. The 20-minute lag time is consistent with the development of the directly-driven magnetospheric response to the IMF [Bargatze et al., 1985]. There is also a delay between the equatorward motion of the cusp regions and the onset of the motion of the polar cap boundary in response to a southward change in the IMF [Lyon et al., 1998; Lopez et al., 1999]. The *Wiltberger et al*. (2003) study confirmed the *Maltsev & Lyatsky* (1975) theory of the cross-tail currents being most responsible for magnetopause erosion. The delay in magnetopause erosion from the arrival of the IMF is not consistent with the "onion peel" model or the Region 1 current fringe field model, but it is consistent with the Region 1 model if one adds the effect of the nightside magnetotail currents with a delay in the time those currents change relative to changes in the dayside conditions.

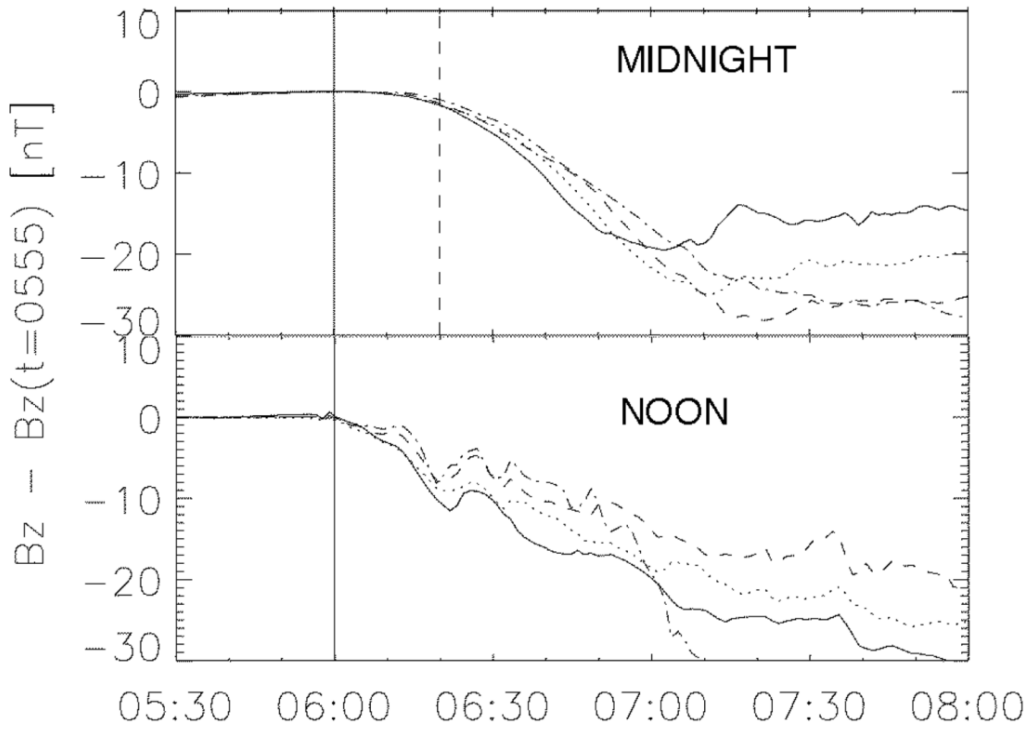

Figure 4-2 The difference between the magnitude of the equatorial B_z at a given simulation time and the value of the equatorial B_z at 0555 UT for several values of the X coordinate (Y and Z = 0) for a case where the IMF was changed from B_z = 5 nT to B_z = -5 nT in the LFM simulation. The solid line is the value at X = 6 R_E, the dotted line the value at X = 7 R_E, the dashed line is X = 8 R_E, and the dash dot line is X = 9 R_E [constructed from Figures 5 and 7 from *Wiltberger et al.* (2003)].

A significant portion of the magnetopause erosion does not even start until 20 min after the southward IMF arrives at the dayside. This suggests that IMF variations might result in an instantaneous magnetopause position that differs from the steady state position.

4.3 The *Bonde et al.* (2018) Study on the Response of the Subsolar Magnetopause to IMF Fluctuations

This study concentrated on fluctuations solely in the southward IMF B_z as that is the most important component of the IMF. The input of IMF B_z into LFM was taken to be a sinusoidal input (± a constant) while $B_x = B_y = 0$. The baseline of the sinusoidal IMF B_z input is taken to be the average value of the sine wave and the amplitude is taken to be the maximum displacement from the baseline. The other solar wind parameters were held constant and at the same values as the initialization (n = 5 cm^{-3}, V_x = -400 km/s, C_s = 40 km/s, $V_y = V_z = 0$, and zero dipole tilt). The uniform conductance for the ionosphere model was set at 10 S for all runs.

The subsolar magnetopause position was determined to be the point at which the magnetic field crosses $B_z = 0$. This provides a well defined and unambiguous definition for the magnetopause eposition. Figure 4-3 shows the LFM-MIX output for B_z in the equatorial plane along the Sun-Earth line with the magnetopause location circled in red (where it crosses the $B_z = 0$ line). The IMF B_z input has been constant for several hours at -9 nT.

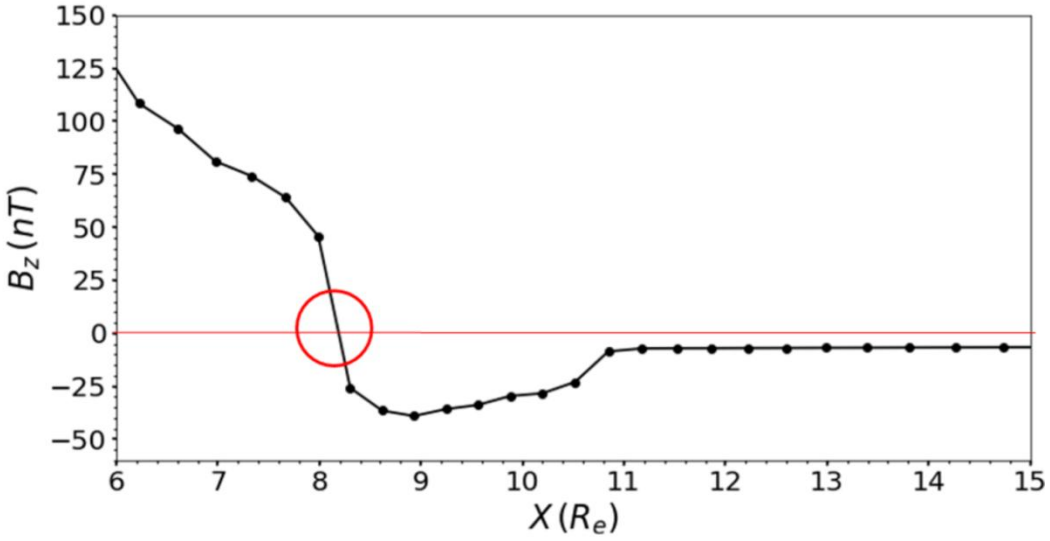

Figure 4-3 LFM-MIX simulation output of B_z in the equatorial plane along the Sun-Earth line. At this time step, IMF B_z has been constant at -9 nT for several hours. The magnetopause location is determined where B_z crosses the 0 nT line (circled in red) [figure 1 from *Bonde et al.* (2018)].

Since Earth's magnetic dipole is always pointed north, this method of finding the magnetopause position only works for southward directed IMF. Therefore, all IMF B_z amplitudes were kept less than the input IMF B_z baseline (i.e. the input IMF B_z was southward for the entire simulation). A variety of input IMF B_z amplitudes, frequencies, and baselines were tested to see the response of the subsolar magnetopause position. All magnetopause positions were determined several hours after initialization in order to establish some sort of equilibrium and not be subjected to the delayed growth of the cross-tail current as described in *Wiltberger et al*. (2003).

The first effect noticed when adding oscillations to the IMF B_z component is that the average magnetopause position is inflated relative to steady state values. The effect is somewhat more pronounced the more negative the IMF B_z is. Figure 4-4 shows the

magnetopause position for steady state values (green dots) and the average magnetopause position for B_z oscillations (black dots). While the average value of the oscillating IMF B_z input is the same as the steady state value, the average magnetopause position in figure 4-4 is more distant from Earth outward with oscillations than under steady state conditions.

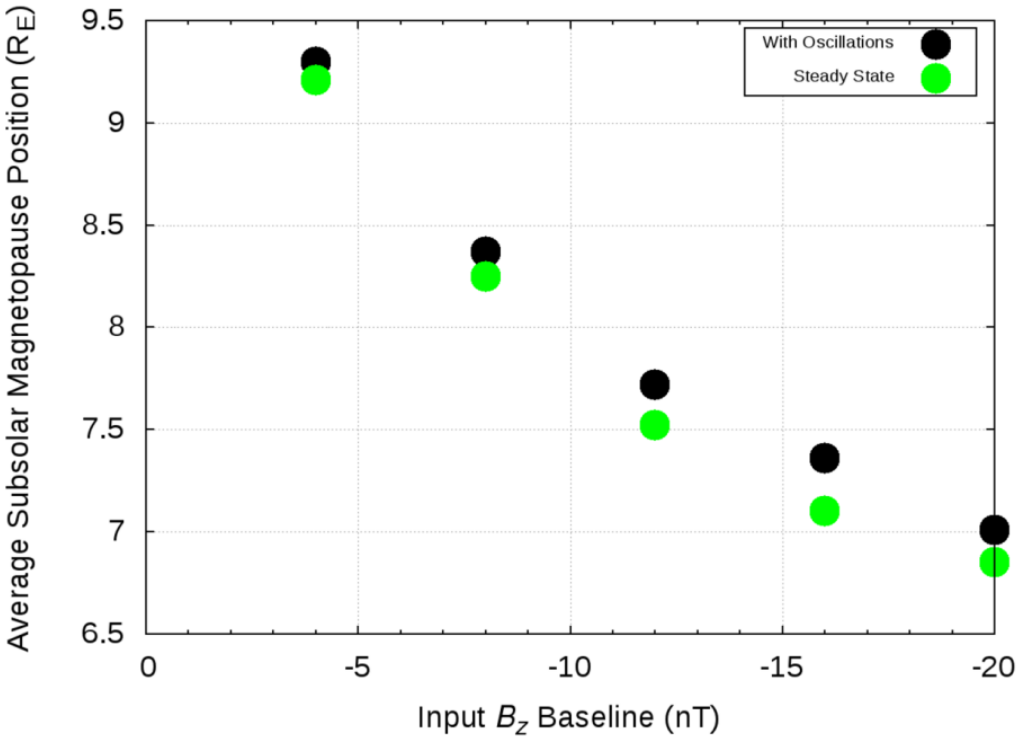

Figure 4-4 Average position of the subsolar magnetopause for steady state solar wind inputs (green dots) and with B_z oscillations (black dots). The oscillations were 60 minute sine waves and a 3 nT amplitude added to the baseline [figure 4 from *Bonde et al.* (2018)].

The next effect seen when oscillations were added was a sort of dampening effect of the subolsar magnetopause position amplitude as a function of input IMF B_z baseline. The magnetopause position is roughly linearly dependent on the IMF B_z value (for moderate IMF magnitudes) in both observations [Sibeck et al., 1991] and MHD simulations. Figure 4-5 presents five input IMF B_z baselines (averages values) from -4 nT to -20 nT in steps of 4 nT. The magnetopause positions were taken over a three cycle period (starting at the end of the initialization period plus two cycles) and then averaged.

For the -4 nT baseline in figure 4-5, the magnetopause positions oscillate between about 9 R_E and 9.5 R_E (amplitude of roughly 0.25 R_E) for the 1 nT input IMF B_z amplitude. For the -20 nT baseline, at 1 nT input IMF B_z amplitude, the magnetopause oscillates between about 6.8 R_E and 7.1 R_E (amplitude of 0.15 R_E) which is a smaller response than for the -4 nT baseline. This reduction in the magnetopause amplitude response can be seen in the other input IMF B_z amplitudes.

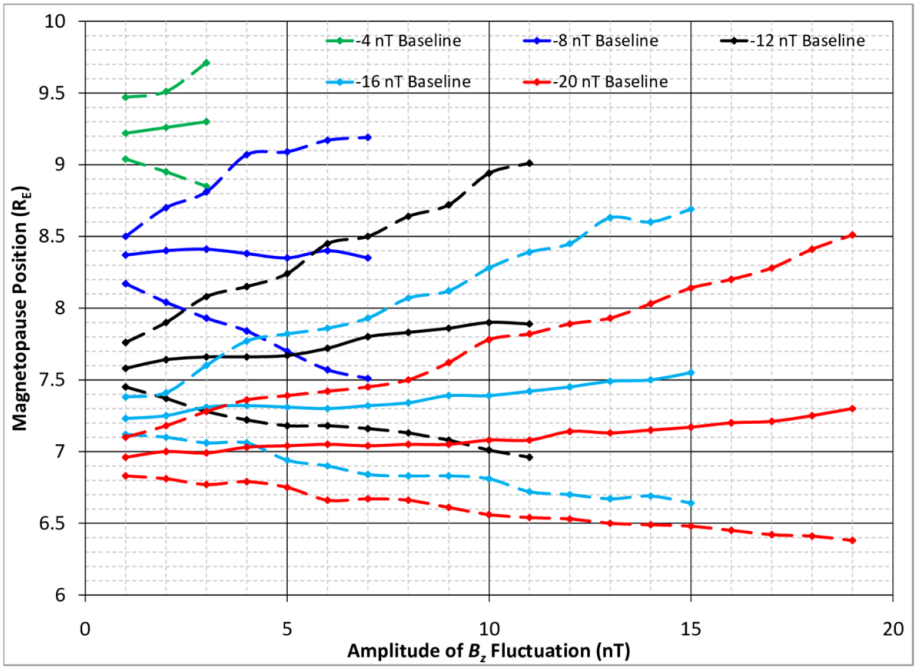

Figure 4-5 Minimum, maximum, and average subsolar magnetopause positions as a function of input IMF B_z amplitude. All oscillations had a 60-minute period [figure 5 from *Bonde et al.* (2018)].

In general, the magnetopause displacements are linearly related to the amplitude of the IMF B_z oscillation. The outward motion of the magnetopause tends to have greater amplitudes than the inward. This effect is seen more in the larger baseline magnitudes (-12 nT, -16 nT, -20 nT). This makes sense, since the inward motion of the magnetopause for large magnitude baselines corresponds to the saturation region shown in figure 4-1.

This dampening effect of the subsolar magnetopause is more apparent in figure 4-6. This figure shows an equatorial cut plane (in ParaView) color-coded for density for zero IMF conditions. The yellow dashed line and the white dashed line represent the subsolar magnetopause locations for -1 nT and -11 nT, respectively. The solid green

lines represent the maximum and minimum subsolar magnetopause positions for a -6 nT IMF B_z input baseline and a 5 nT input amplitude. The green dashed line is the -6 nT steady state input magnetopause position.

With a 5 nT amplitude from a -6 nT baseline, the input IMF B_z values will reach a minimum of -1 nT and a maximum of 16 nT. The maximum and minimum subsolar magnetopause positions (solid green lines) never relax to the steady state values (yellow and white dashed lines) and can be as much as 1 R_E away from the steady state values. Furthermore, the subsolar magnetopause location is much closer to the -11 nT steady state value as compared to the -1 nT steady state value, even though it's is oscillating about a baseline (-6 nT) half-way in between.

As expected from the *Wiltberger et al.* (2003) study, the motion of the magnetopause is delayed relative to the variation in the input IMF B_z. Figure 4-7 shows this delay for a -8 nT input IMF B_z baseline and a 3 nT amplitude. There is about a 12-minute delay between the maximum southward IMF input and the maximum earthward displacement (erosion).

Using the same set of cycles to calculate the average displacement of the magnetopause in figure 4-5, the time lag for two different input IMF B_z baselines and several amplitudes was calculated – the results are presented in figure 4-8.

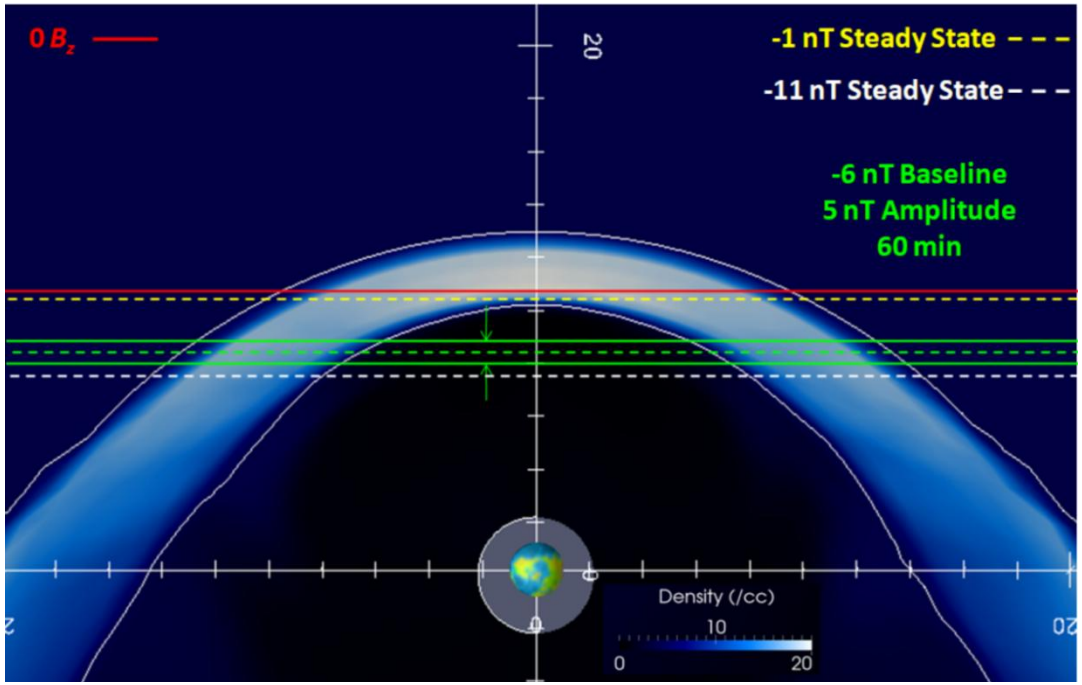

Figure 4-6 ParaView image of an equatorial cut plane color-coded for density with zero IMF conditions, n = 5 cm^{-3}, $V = V_x$ = -400 km/s, and C_s = 40 km/s. The red line is the subsolar magnetopause position for zero IMF. The yellow and white dashed lines indicate the subsolar magnetopause positions with steady state input B_z for -1 nT and -11 nT, respectively. The green dashed line is the subsolar magnetopause position for a steady state -6 nT B_z input. The solid green lines are the maximum and minimum subsolar magnetopause positions for a -6 nT baseline and a 5 nT amplitude for a 60-minute period [figure 6 from *Bonde et al.* (2018)].

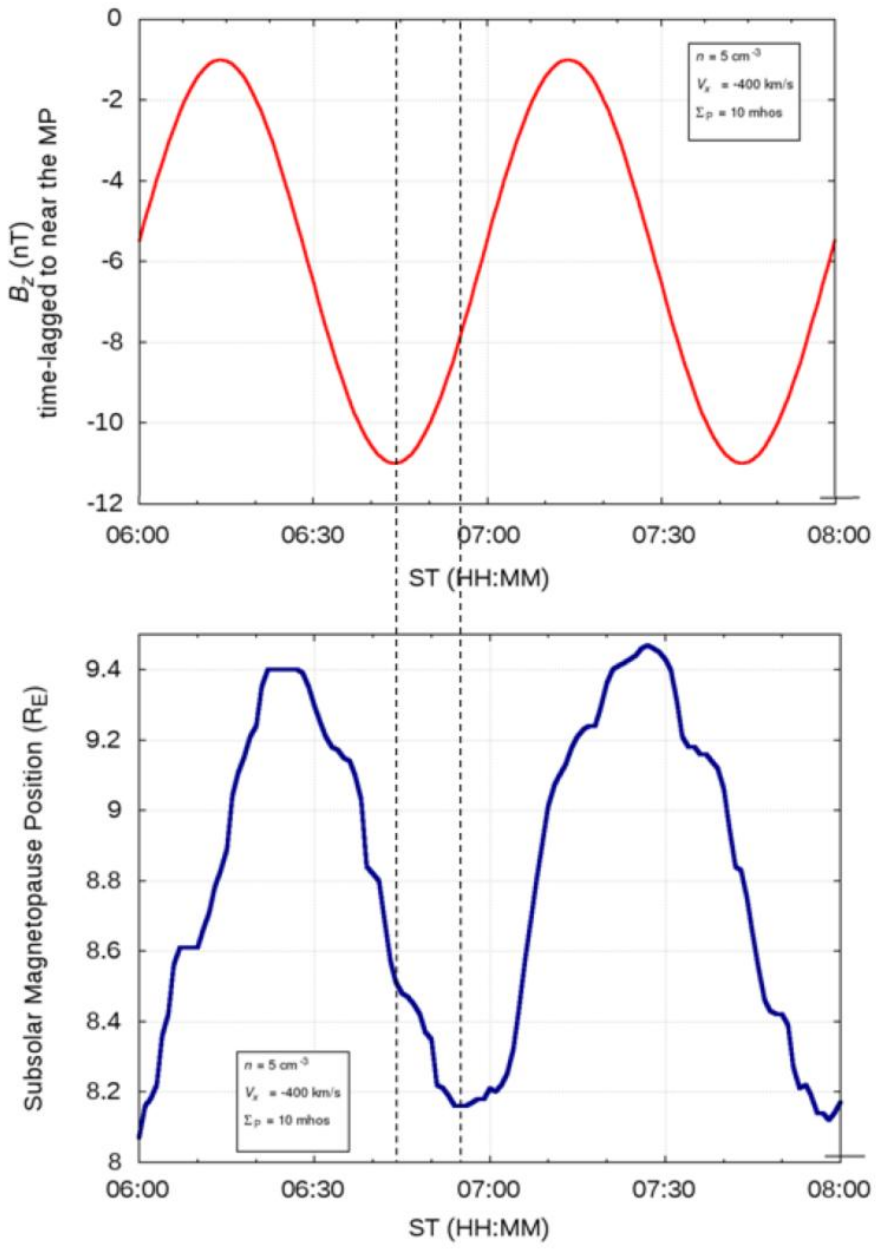

Figure 4-7 Time-lagged comparison between the input IMF B_z sine wave time lagged for the arrival at X = 0 (top panel) and the response of the subsolar magnetopause position (bottom panel). The baseline input IMF B_z was -8 nT with a 3 nT amplitude for a 60-minute sine wave [figure 7 from *Bonde et al.* (2018)].

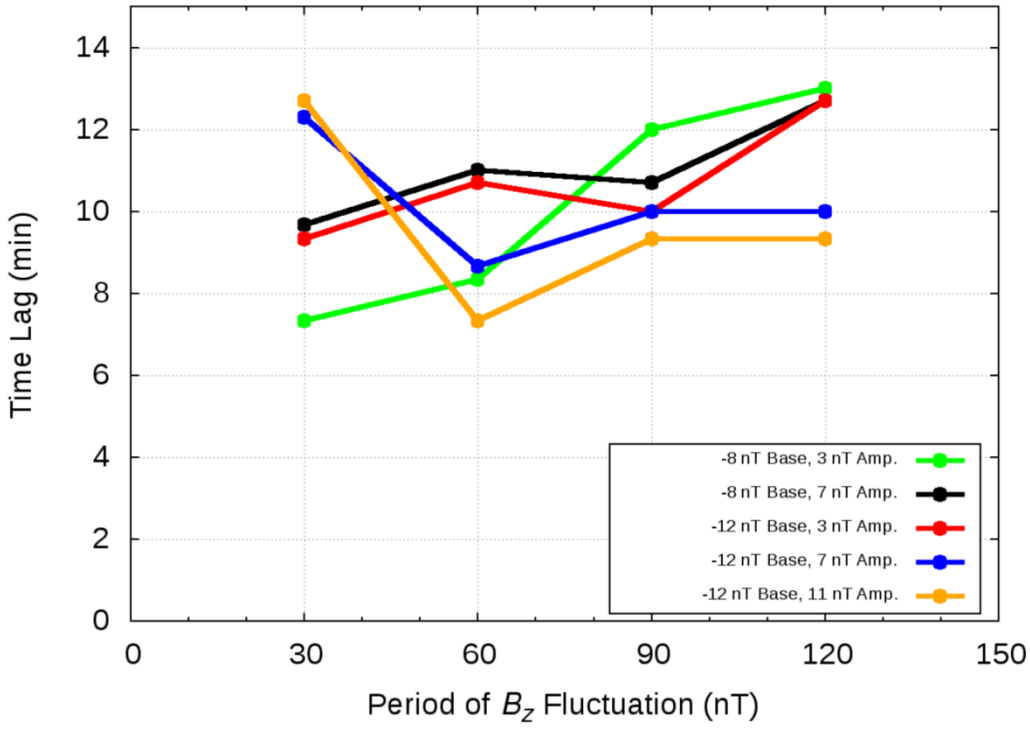

Figure 4-8 Subsolar magnetopause oscillation time lag relative to IMF B_z input as a function of IMF B_z oscillation period for different input IMF B_z amplitudes and baselines of -8 nT and -12 nT [figure 8 from *Bonde et al.* (2018)].

It is evident from figure 4-8 that there is no consistent trend for the time delay of the subsolar magnetopause position depending on input IMF B_z period, amplitude, or baseline. More extreme baseline cases (-20 nT) were tested and showed similar results. For any given run, there is significant variability, with averages ranging from 6 minutes to 14 minutes. Even with this variability, the average time lag as a whole is on the order of 10 minutes.

Given that it takes 20 minutes for the cross-tail currents to build up and weaken the dayside field [Wiltberger et al., 2003], it is not surprising that there is a lag time

between the IMF variation and the magnetopause position. Moreover, the response of the dayside currents is quite prompt [Lopez et al., 1999]. Thus, an average lag time between the IMF variation and the magnetopause response is not unreasonable since it is roughly the average of the two response times. Given that the lag time does not seem to depend on the nature of the IMF magnitude or frequency, it seems that it is controlled by internal magnetospheric time scales rather than external forcing.

It is clear from the results presented here that the time history of the IMF must be considered when determining the magnetopause position. For example, with a steady IMF B_z of -1 nT, we would expect to find tha magnetopause at 10.5 R_E, yet for a -4 nT baseline and an amplitude of 3 nT, the IMF B_z achieves a value of -1 nT every 60 minutes and the magnetopause never inflates past 9.7 R_E (on average). Cases with large baselines and fluctuations have a value of a subsolar magnetopause position that's even closer to the Earth. This shows that during periods of HSS, the empirical models of the magnetopause position may be less reliable.

Another interesting result from this study was the time it takes for the magnetopause to inflate to steady state values. Most of the work presented here was done with 60-minute sine waves. Although it only takes 20 minutes for significant erosion to occur, perhaps the continual variation in the solar wind does not allow the magnetopause enough time to relax to steady state values. Although the subsolar magnetopause position amplitude grows with input IMF B_z amplitude, the steady state subsolar magnetopause positions move farther away from the baseline.

Figure 4-9 presents the subsolar magnetopause position amplitude as a function of input IMF B_z oscillation period over a few input IMF B_z amplitudes at -16 nT baseline. The amplitude response of the subsolar magnetopause position increases with increasing input oscillation period and tend towards saturation, both of which can be

expected. The blue stars indicate the time for the maximum (outward) subsolar magnetopause position to achieve the corresponding maximum steady state value and the orange stars are the times it takes the minimum (inward) subsolar magnetopause position to achieve the corresponding minimum steady state value.

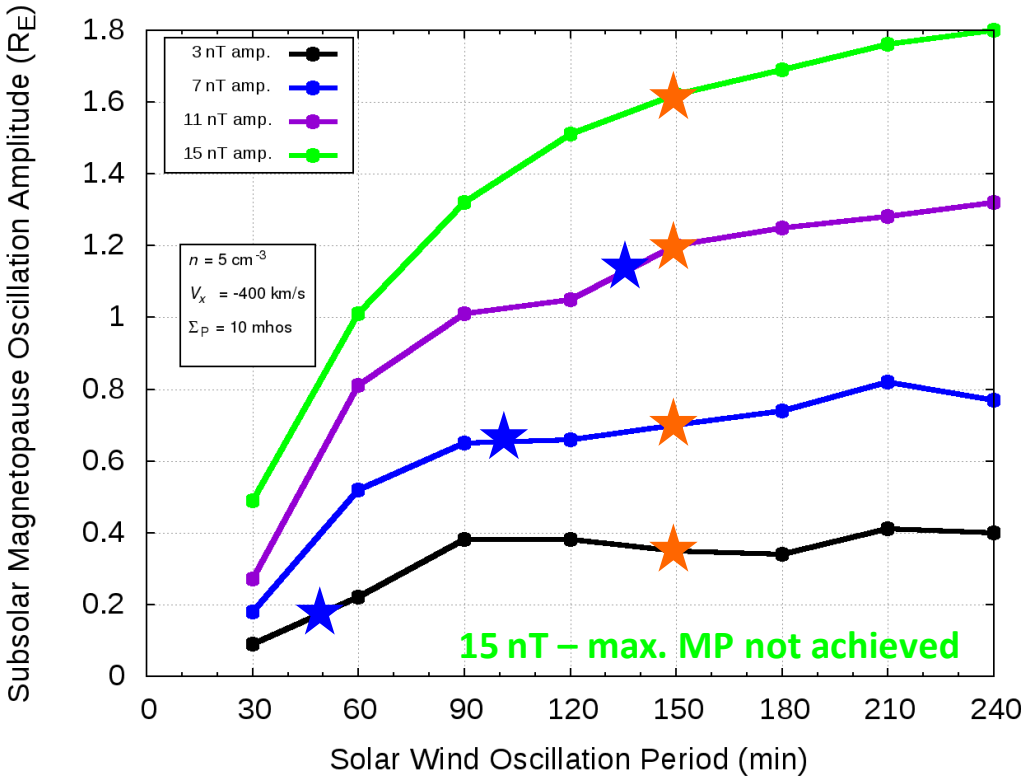

Figure 4-9 Subsolar magnetopause oscillation amplitude as a function of input IMF B_z oscillation period for differing input IMF B_z amplitudes (with a -16 nT baseline). The blue stars indicate the time for the maximum (outward) subsolar magnetopause position to achieve steady state values. The orange stars indicate the time for the minimum (inward) subsolar magnetopause to achieve steady state values.

For the 3 nT amplitude input (black line), the values of the IMF B_z input oscillate between - 13 nT and -19 nT. The corresponding steady state subsolar magnetopause

positions are 7.46 R_E and 6.92 R_E, respectively. With roughly a 45 minute input oscillation period, the maximum (outward) subsolar magnetopause position is on average 7.70 R_E. For any oscillation period greater than 45 minutes, the subsolar magnetopause will achieve the steady state value (and inflate even more in this case). However, the minimum (inward) subsolar magnetopause position will not be achieved unless there is at least a 150 minute input oscillation period (indicated by the orange star).

It is interesting to note that it takes roughly a 150-minute input oscillation period to achieve the inward steady state subsolar magnetopause position, regardless of the input IMF B_z amplitude. The time it takes to achieve the maximum (outward) steady state value increases with input oscillation period to the point where after an 11 nT input IMF B_z amplitude, the outward most value of the subsolar magnetopause response will never achieve the steady state value.

4.4 Conclusions

The magnetopause motion exhibited a range of behaviors which can be understood in terms of time lag [Bonde et al., 2018]. For large values of the IMF, the magnetopause exhibited saturation behavior [e.g. Lopez et al., 2010]. The motion of the subsolar magnetopause responded as expected, with a sort of dampening effect for large IMF oscillation amplitudes. The 10-miinute time delay of the magnetopause response (see figure 4-8) is not surprising, given that it takes 20 minutes for the tail currents to build up [e.g. Wiltberger et al., 2003] and the response of the dayside currents is quite prompt [e.g. Lopez et al., 1999]. This 10-minute time lag seems to be an average of the two response times. The most interesting aspect of this study was the magnetopause could be up to 1 R_E away from the nominal position for stead state values. This showed

that the time history of the IMF is of a significant importance and that empirical models of the magnetopause may be less reliable than at other times.

There is a significant limitation to this study and that is the IMF was not allowed to turn northward. During the duration of a HSS, the fluctuating IMF has both northward and southward directions. The determination of the magnetopause position for northward IMF is extremely difficult given that the IMF direction is aligned with Earth's magnetic dipole. In the LFM simulation, field lines may be traced to see which field lines are connected to Earth and which are connected to the solar wind. The boundary between the last Earth-connected field line and the first solar wind-connected field line (as moving outward from Earth) is the magnetopause position. However, this involves tracing many field lines, over many time steps, and many LFM runs, which quickly became too computationally intensive. This study is nonetheless important as it is the southward B_z component along with large amplitude Alfvén waves that are mostly responsible for magnetic reconnection at Earth [Tsurutani & Gonzalez, 1987].

Chapter 5

Simulation of a High-Speed Stream: A Case Study

5.1 NASA's THEMIS Mission

In 2007, NASA launched a constellation of five satellites called THEMIS (Time History of Events and Macroscale Interactions during Substorms) in a highly elliptical orbit around Earth. The THEMIS mission's primary objective was to study the processes that initiate substorms; however, another objective was to study dayside interactions in the magnetosphere [Sibeck & Angelopoulos, 2008]. Its highly elliptical orbit puts it into a position to have the magnetopause cross over it a few months a year. THEMIS is complementary to MMS (Magnetospheric Multiscale Mission), another NASA mission with a constellation of four satellites flown in a tetrahedral formation. The MMS mission's primary objective is to study magnetic reconnection in the magnetosphere [Burch et al., 2016]. By having MMS in opposition to THEMIS, one mission can observe magnetic reconnection on the dayside while the other can observe it on the nightside.

The eccentricity of the THEMIS spacecraft has increased since its launch. Figure 5-1 (left) shows the five THEMIS spacecraft in the equatorial plane about a year and a half after their launch. Their apogee is in such a position to just approach the magnetopause. It would take a large increase in dynamic pressure or a strong southward IMF to push the magnetopause cleanly past THEMIS. A clean crossing is one where the spacecraft moves all the way from the magnetosheath into the magnetosphere and remaining there for a length of time. The spacecraft could also move from the magnetosphere into the magnetosheath. Since the THEMIS apogee is at about the location we would expect to find the magnetopause, many THEMIS approaches just grazed the magnetopause. A THEMIS summary plot for September 21, 2008 is presented in figure 5-2. The high B_Z values earlier in the day (top panel, figure 5-2)

indicate that THEMIS A is moving from inside the magnetosphere towards the magnetopause. At about 15:00 UT, THEMIS moves somewhat into the magnetosheath, since there are periods of $B_Z < 0$. The ESA (Electrostatic Analyzer) also shows an indication of magnetosheath plasma (third panel from the bottom, figure 5-2) – a larger density of lower energy electrons.

While it is clear that THEMIS made an approach to the magnetopause, there is not a definitive, clear magnetopause crossing. There were very few clean magnetopause crossings during the first few years of the THEMIS mission. Figure 5-1 (right) shows orbits that are more eccentric, allowing for a clean pass through the magnetopause. Most of the clean THEMIS magnetopause crossings were over the past few years.

In late 2009, THEMIS B (P1) and THEMIS C (P2) left Earth orbit for the Moon. They reached lunar orbit in 2010 and were re-designated as ARTEMIS (Acceleration, Reconnection, Turbulence and Electrodynamics of the Moon's Interaction with the Sun) [Sweetser et al., 2012].

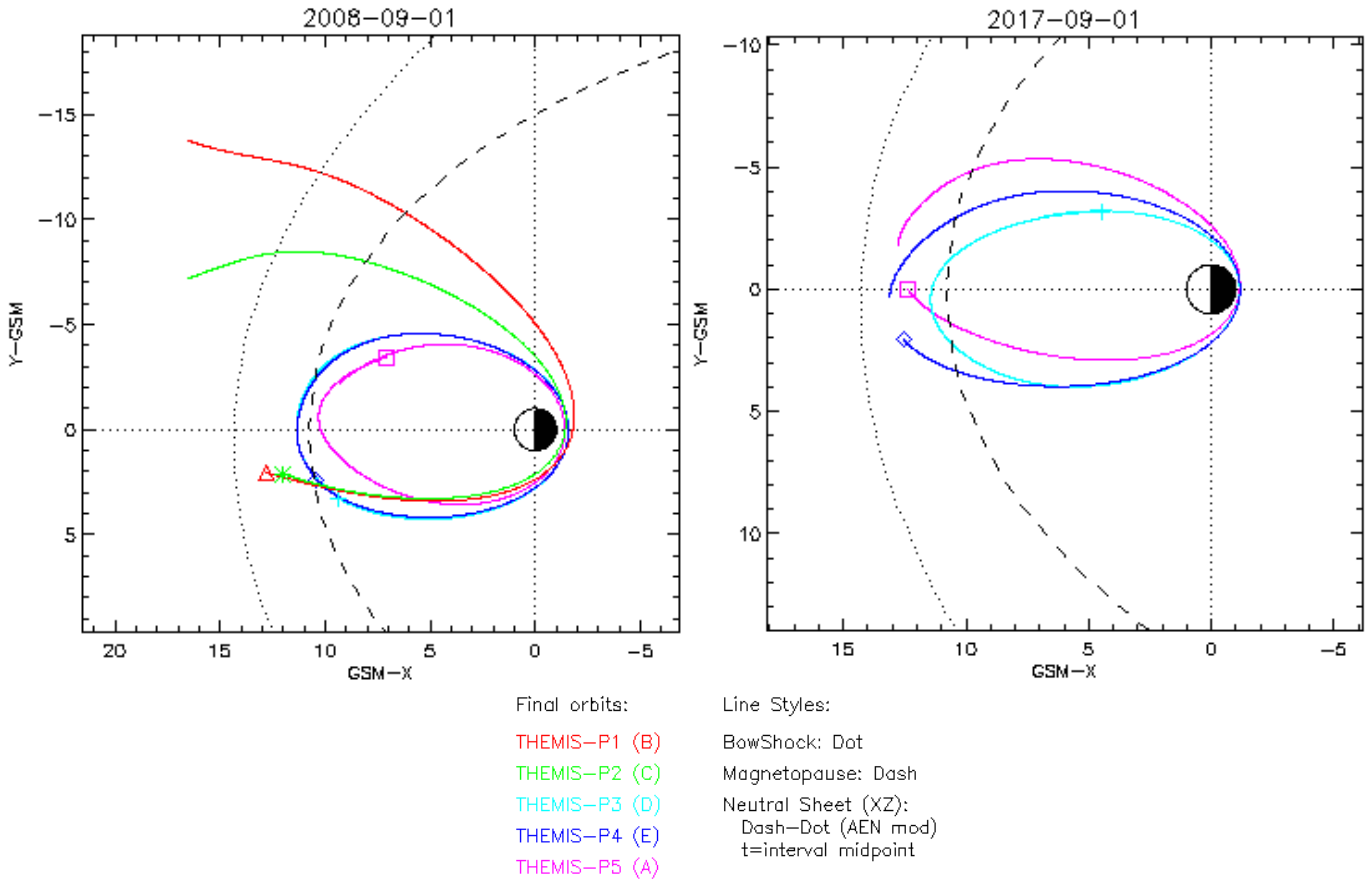

Figure 5-1 Equatorial plane view of THEMIS orbit plot for 1 September 2008 (left) and 1 September 2017 (right). The magnetopause and bow shock positions are for a dynamic pressure of 2 nPa and 0 IMF [NASA/THEMIS/Berkeley].

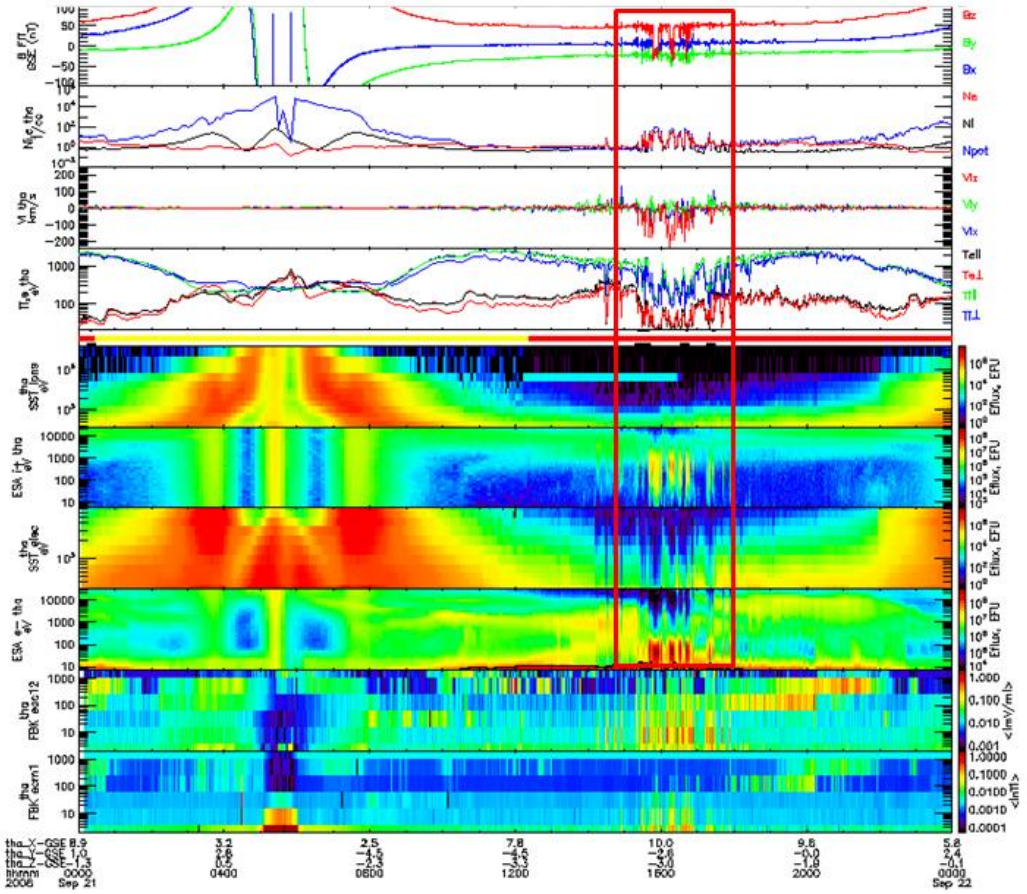

Figure 5-2 THEMIS A (P5) summary plot for 21 September 2008 [NASA/THEMIS/Berkeley].

5.2 14-19 September 2017 High-Speed Stream

The last part of this work was to find a high-speed stream (HSS) and simulate it in LFM. A collection of THEMIS magnetopause crossings would be cataloged and those magnetopause positions would be compared to LFM and empirical models.

In September of 2017, a series of four HSS impacted Earth. The average solar wind bulk flow speed for the month was 520 km/s. These HSS occurred in favorable conditions as THEMIS apogee was near the nose of the magnetopause (along the Sun-

Earth line, see figure 5-1). The first two HSS had large data gaps and the magnetopause crossings were not able to be analyzed. The last two of the month had no large data gaps; however, the fourth one had only a couple of clean magnetopause crossings. The third HSS, occurring from September 14 to September 19, 2017, had eight clean magnetopause crossings. Figure 5-3 presents the solar wind B_Z, flow speed, and proton density during the HSS. Even though the HSS occurred into the 19th, there was some data gaps on the 19th. This day was therefore removed for analysis.

The solar wind data was retrieved from OMNIweb. This is data collected from various solar wind-reading satellites at the L1 Lagrange point. An algorithm is then used to propagate the data to Earth's predicted bow shock.

A HSS is characterized by a large spike in proton density from the higher speed stream running into the slower solar wind, creating a buildup of proton density. There is a peak in solar wind bulk flow velocity, which starts to decrease during the remainder of the HSS. A characteristic of a HSS is the bulk flow properties of the solar wind during a HSS are relatively constant, with proton densities around 2-3 cm^{-3} [Kivelson & Russell, 1995], since the density behind a HSS is tenuous.

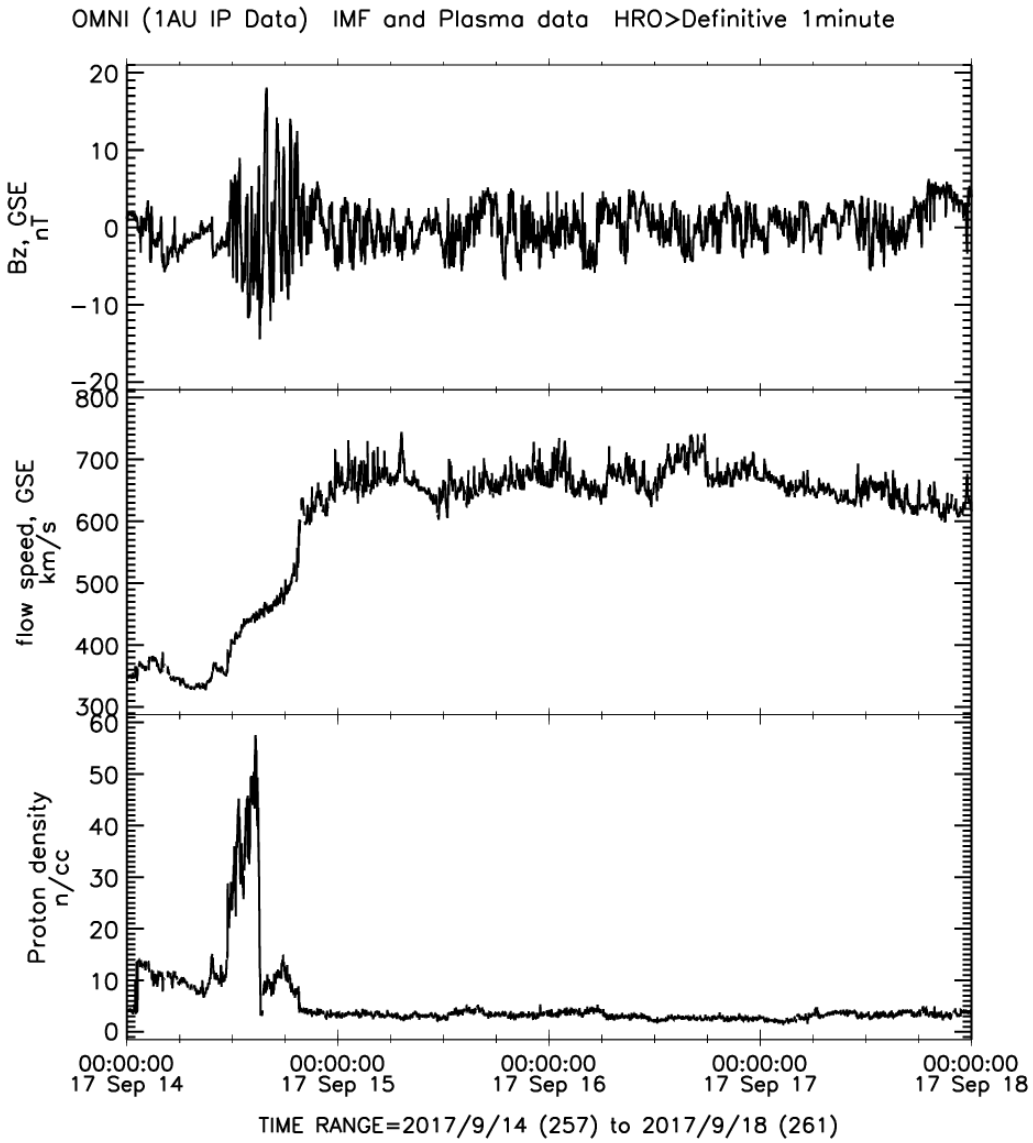

Figure 5-3 OMNI solar wind data for 14-18 September 2017

[NASA/GSFC/CDAWeb/OMNI].

The start of the HSS that was analyzed arrived by noon on the 14th and the speed elevated past 450 km/s by 15:00 UT. The HSS analysis was not started until 19:00 UT on the 14th to allow for both the bulk flow velocity to increase and the proton

density to settle down to roughly constant values. This HSS was rather unique as the density was close to 4 cm^{-3} for the duration of the HSS and the velocity doesn't start decreasing until two days after the HSS arrived. This could have been due to an expanded coronal hole. Figure 5-4 (left) shows the Sun on September 11, 2017. The coronal hole can be seen extending down equatorward from the solar north pole. It takes 2-3 days for high-speed solar wind to reach Earth. The coronal hole is elongated and is still visible on September 15, 2017 (see figure 5-4, right).

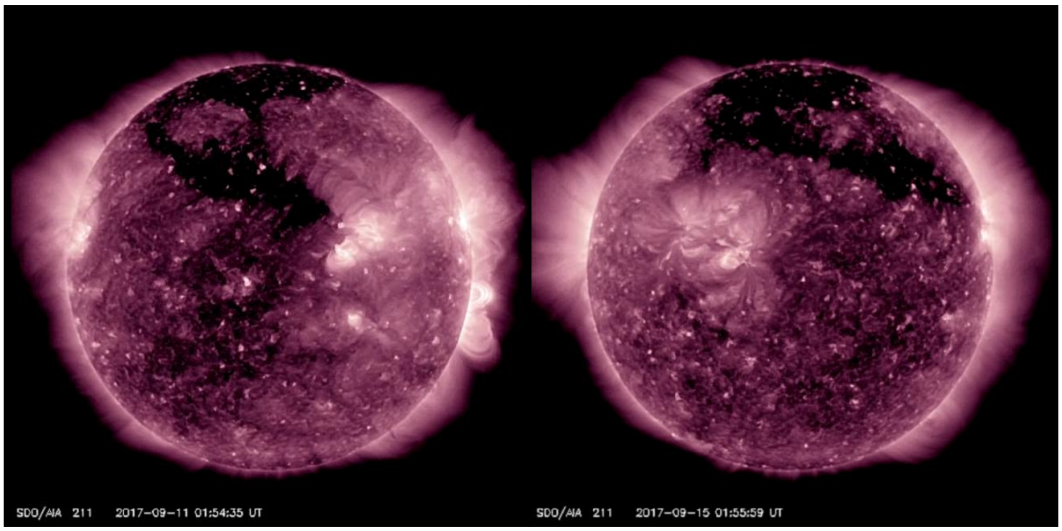

Figure 5-4 SDO image of the Sun at 211 Å on 11 September (left) and 15 September (right), 2017 [NASA/SDO/GSFC].

5.3 Identification of a THEMIS Magnetopause Crossing

The same method of identifying a crossing that was used in chapter 4 was used here: the crossing of the B_Z = 0 line from southward IMF to the positive B_Z of Earth's magnetic dipole (or vice versa). To further identify a crossing, the ESA was scanned to be sure that the plasma was indeed magnetosheath plasma – a higher density of lower energy electrons. To make sure that the crossing was during southward IMF conditions,

at least 10 continuous data points of southward IMF had to precede the crossing into the magnetosphere, or 10 continuous data points of southward IMF had to follow a crossing into the magnetosheath. The FGM (Flux Gate Magnetometer) on THEMIS reads every 3 seconds, so this represents 30 seconds of continuous southward IMF.

If there were some northward IMF data points in the preceding 10, the number of continuous data points was extended to 30 and a restriction that not more than 20% of the data points in the 30 could be northward IMF. In addition, there could be no more than 3 continuous data points of northward IMF in the preceding 30.

Once THEMIS is inside the magnetosphere, the B_Z values must be above 30 nT and sustained at these values for better than 90% of the data points. Most of the crossings happened around 9-10 R_E and the value of Earth's magnetic dipole at 10 R_E is roughly 30 nT.

A limit on how long THEMIS could be inside or outside the magnetosphere was placed at 3 minutes to allow enough time for THEMIS to read magnetospheric B_Z values or southward IMF values. For example, THEMIS could cross into the magnetosphere at X = 9 R_E, in which case the dipole field value should be at least 40 nT. If THEMIS were to cross into the magnetosphere for 1 minute and then back out, it would not have enough time to achieve B_Z values that should be expected at 9 R_E.

It should be noted that when THEMIS is referred to as "crossing" into the magnetosphere, what is really happening is that the magnetopause is moving over THEMIS – the magnetopause moves too fast compared to THEMIS.

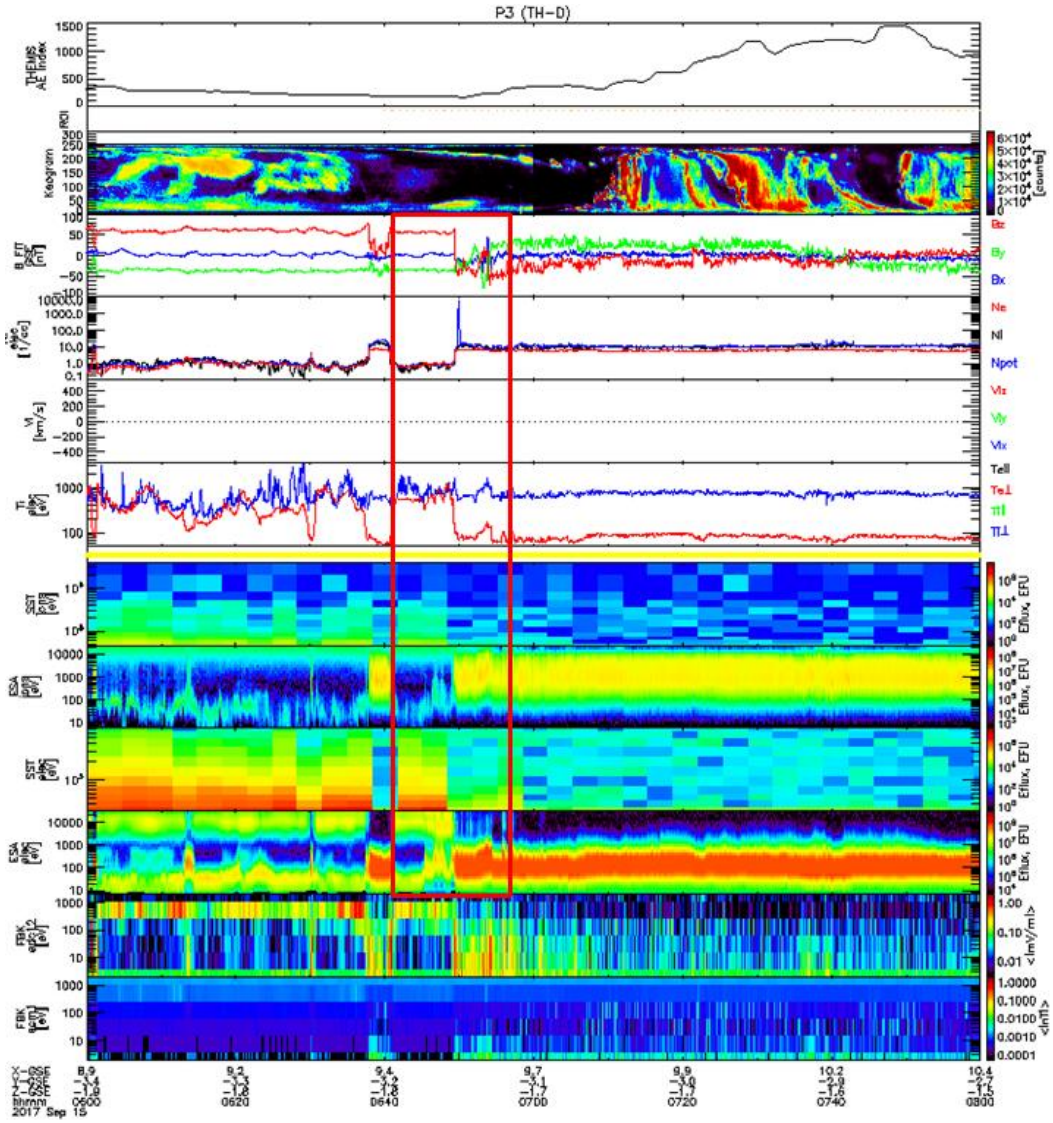

Figure 5-5 THEMIS D summary plot for 15 September 2017 from 06:00 UT to 08:00 UT. The crossing happens at 06:49 UT [NASA/THEMIS/Berkeley].

Figure 5-5 shows a summary plot for THEMIS D on September 15, 2017 from 06:00 UT to 08:00 UT. THEMIS D crossed from inside the magnetosphere to the magnetosheath at 06:49 UT as indicated in the red box (the B_Z = 0 line is clearly crossed in the top panel and the red bands in the ESA, third panel from the bottom, indicate

magnetosheath plasma). There was another crossing earlier at 06:40 UT, indicated by the red bands in the ESA; however, as seen in the top B_Z panel, this was a northward IMF crossing and therefore is excluded from this study.

THEMIS FGM data was retrieved from CDAweb (Coorindated Data Analysis web), a database of solar wind parameters for all NASA missions. THEMIS orbit information was retrieved from SSCweb (Satellite Situation Center web), a database of orbit information for all NASA missions. The SSC plot for THEMIS D during the crossing at 06:49 UT is presented in figure 5-6.

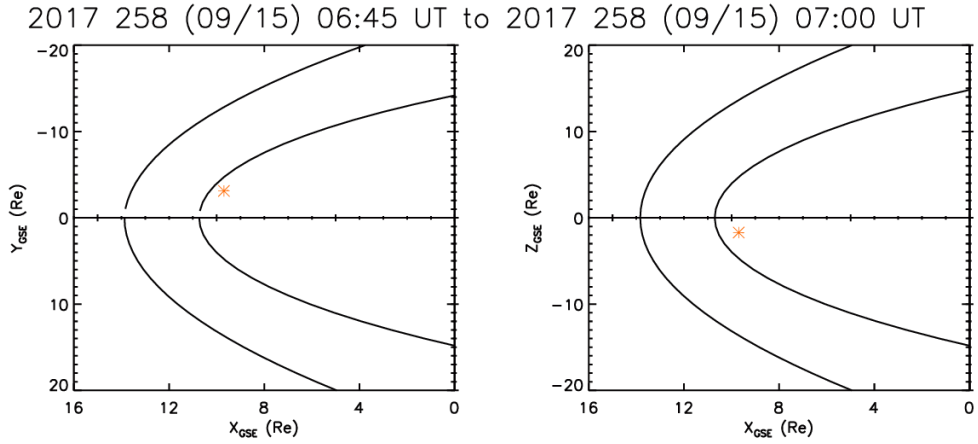

Figure 5-6 THEMIS D position (orange) during the September 15, 2017 06:49 UT crossing in the equatorial (left) and meridional (right) planes. The line closest to THEMIS D is the magnetopause for a solar wind dynamic pressure of 2 nPa and 0 IMF. The line to the left of that is the bow shock for the same conditions [NASA/GSFC/SSC].

5.4 Comparison to Empirical Models of the Magnetopause

After a THEMIS crossing was identified, the satellite location was compared to LFM and three empirical models:

Roelof & Sibeck (1993) – hereafter referred to as RS93. The RS93 model is employed on NASA's Satellite Situation Center (SSC) ["Models and Regions", n.d.].

Petrinec & Russell (1996) – hereafter referred to as PR96.

Shue et al. (1998) – hereafter referred to as SA98.

These models use the solar wind dynamic pressure and IMF B_Z to predict the *X* and *Y* values of the magnetopause. The analytical form for each model is presented in appendix A. All of these model predictions, as well as the THEMIS crossing location, were plotted in LFM to see how well LFM did in predicting the magnetopause. An equatorial plane view in LFM for the September 15, 2017 06:49 UT crossing of THEMIS D is presented in figure 5-7. The SAT location is the location where THEMIS crosses the magnetopause, given as the *X* value only. The crossings presented here were close to noon ($R_{YZ} = \sqrt{Y^2 + Z^2} < 4\ R_E$) and therefore there is no significant difference between the magnetopause position that crossed over THEMIS and the position along the Sun-Earth line. The magnetopause predictions for the three models are also shown in figure 5-7.

The LFM value was obtained by tracing magnetic field lines in LFM. It should be noted that there is the possibility of a discrepancy in the actual time the crossing happens in LFM, due to the nature of when the solar wind enters the LFM grid. There could be up to a 7 minute difference between the actual time of the crossing and when that solar wind propagates to the magnetopause. The magnetopause location was checked in LFM at times 10 minutes before and 10 minutes after the time of the THEMIS crossing. The average distance away from the magnetopause that LFM predicts was no more than 1-2% difference than the reported LFM values.

In the case of the THEMIS D crossing at 06:49 UT on September 15, 2017, LFM does a better job than the models at predicting the magnetopause location, with a slight exception to the SA98 model, which is only 2.5% ahead of the true location. The RS93 model is almost 1 R_E behind the magnetopause and the PR96 model is almost 1 R_E in

front of the magnetopause. A similar analysis was done with the seven other crossings. The details for each crossing can be found in appendix B and the results of the analysis are presented in table 5-1.

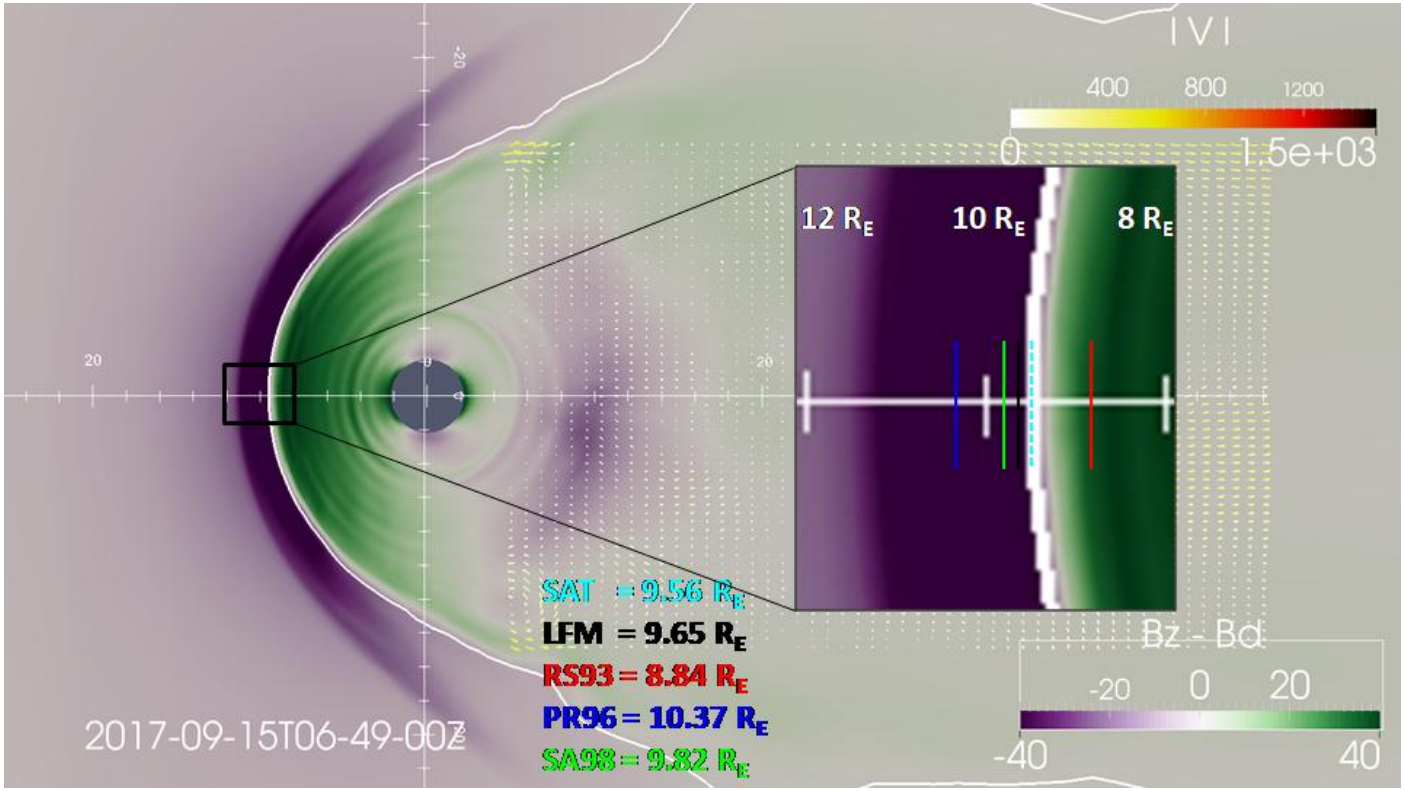

Figure 5-7 Equatorial plane view in ParaView for the September 15, 2017 06:49 UT crossing of THEMIS D, in LFM, color-coded for Earth's magnetic dipole subtracted from B_Z at that location. The turquoise "SAT" line is the location that THEMIS crosses the magnetopause (X coordinate only). The red, blue, and green lines are the empirical model predictions of the subsolar magnetopause location.

Satellite	Date	Time (UT)	X (R_E)	Y (R_E)	Z (R_E)	LFM (R_E)	RS93 (R_E)	PR96 (R_E)	SA98 (R_E)
A (P5)	9/14/2017	2005	10.32	0.03	-0.93	-0.87	-0.58	-0.67	-0.64
A (P5)	9/14/2017	2009	10.27	0.06	-0.90	-0.52	-0.64	-0.69	-0.68
A (P5)	9/14/2017	2042	9.79	0.36	-0.68	-0.94	-1.12	0.17	-0.06
A (P5)	9/14/2017	2046	9.73	0.39	-0.66	-0.58	-1.19	0.33	0.08
D (P3)	9/15/2017	649	9.56	-3.17	-1.74	0.19	-0.72	0.81	0.26
A (P5)	9/15/2017	2337	10.18	-0.06	-0.84	-0.93	-0.73	-0.42	-0.56
D (P3)	9/16/2017	1500	9.80	1.19	0.64	0.15	-1.05	0.14	0.08
D (P3)	9/16/2017	1533	9.35	1.46	0.78	-0.40	-1.44	0.97	0.52
			Average Distance Magnitude (R_E)			0.57	0.93	0.53	0.36

Table 5-1 THEMIS satellite crossings during the 14-19 September 2017 HSS. THEMIS crossed the magnetopause at the *X* value in column 4. The model/simulation results are presented as a distance away from the magnetopause. A negative value is earthward of the magnetopause. The average distance magnitude is the average distance the model/simulation predicts the magnetopause to be from the actual position (crossing) for the 8 crossings.

5.5 Conclusions

From the results, LFM predicts the magnetopause location just as well as the PR96 model and significantly better than the RS93 model. On the other hand, the SA98 model does a lot better job at predicting the subsolar magnetopause. Around October 31, 2003, the Sun unleashed a series of storms called the Halloween Storms. These storms created extreme conditions in the geospace environment that even caused the magnetopause to move inward of geosynchronous orbit [Lopez et al., 2007]. *Lopez et al.* (2007) did a study of magnetopause crossing prediction, comparing LFM to the three models listed above (with the exception of PR96; the *Lopez et al*. (2007) study used the *Petrinec & Russell* (1993) empirical magnetopause model). In this study, LFM was found to have predicted a magnetopause crossing slightly better than the other three empirical models; this is to be expected, since LFM uses fundamental physics whereas the models were pushed well past their limits [Lopez et al., 2007].

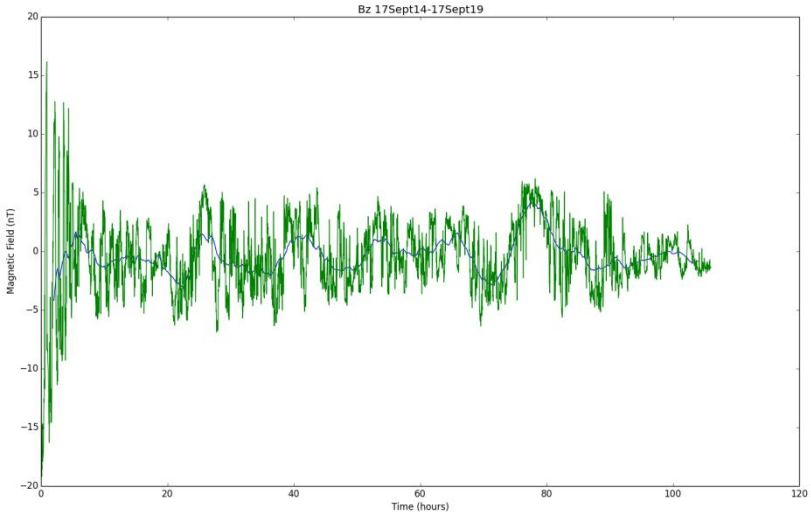

Figure 5-8 Plot of $\delta B_Z / B_Z$ for the 14-19 September 2017 HSS. The blue line is a running boxcar average (every 4 min) and the green line is the B_Z value at that time. [Credit: Michelle Bui & Hector Carranza, Jr.]

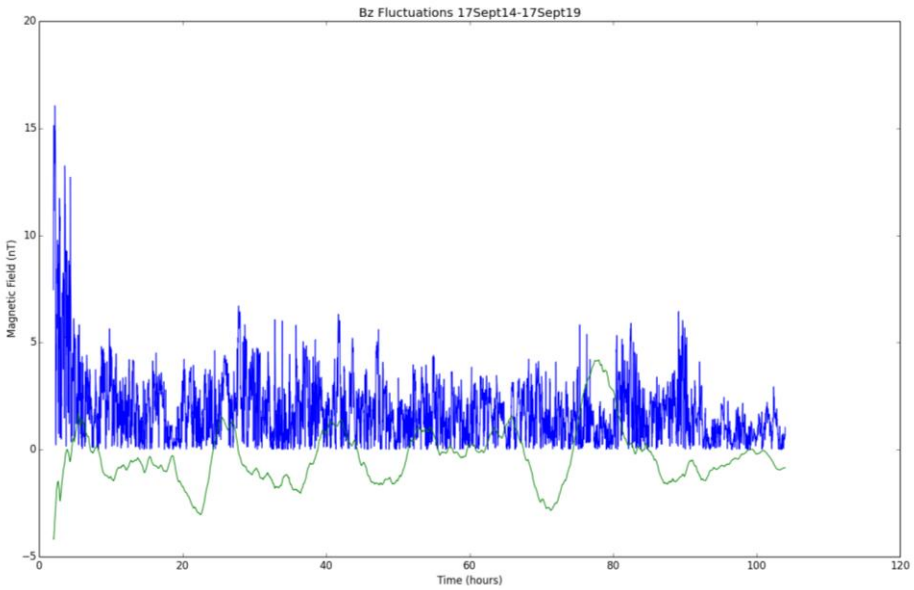

Figure 5-9 Plot of $|\delta B_Z/B_Z|$ for the 14-19 September 2017 HSS. The green line is now the running boxcar average (every 4 min) and the blue line is the $|B_Z|$ value at that time. [Credit: Michelle Bui & Hector Carranza, Jr.].

The limits for the RS93 model are ± 5 nT, the limits for the PR96 model are ± 10 nT, and the limits for the SA98 model are ± 18 nT. The conditions of this HSS were not as extreme as the Halloween Storms, therefore the conditions are within the limits if the models. All crossings happened with roughly – 3 nT < B_Z < 5.5 nT. The flow speed was not too extreme (~ 620 km/s average for the 15th to the 18th). During the main part of the HSS, the Alfvénic fluctuations were not too extreme. Figure 5-8 shows a graph of $\delta B_Z/B_Z$ the HSS. The blue line is the baseline: a running boxcar average (every 4 min). The green line is the value of B_Z at that time. Figure 5-9 shows the magnitude of the δB_Z (blue line) while the baseline is now green. It can be seen that the $\delta B_Z/B_Z$ ~ 2.5. The average baseline for the HSS was about -0.3 nT.

It is clear that LFM will predict the magnetopause location better during extreme conditions, as shown in the *Lopez et al*. (2007) study. LFM certainly does a better job than the RS93 model while the PR96 model is comparable to LFM. The most accurate prediction came from the SA98 model. Further studies with high-speed streams that have even larger Alfvénic fluctuations are needed to bring closure to this issue. The solar wind fluctuations have a time delay that the SA98 model does not represent.

Chapter 6

Summary and Future Work

6.1 Summary

Although previous studies have concentrated mostly on steady state solar wind conditions, the solar wind is exceptionally dynamic. The fluctuations in the solar wind will affect the solar wind-magnetosphere coupling. This in turn will affect the magnetosphere-ionosphere system. The TPP, being a proxy for magnetospheric convection, will show how well the solar wind fluctuations are affecting Earth's magnetosphere. Through a series of numerical experiments, we showed that oscillations in the equatorial plane showed little to no effect on the TPP. Once the amplitude of oscillations was at V_Y = 90 km/s or greater, the sinusoidal response to the TPP was evident, albeit with double the input period. The sinusoidal response to the TPP for meridional oscillations was apparent for all V_Z oscillation amplitudes run. The most interesting effect noticed in this numerical experiment was hemispheric asymmetry in the TPP due to the variations, with up to a 25 kV difference in the TPP between the hemispheres. The visualizations showed large asymmetries in the magnetotail. One of the two tail lobes exhibited large sunward flow as a result. The oscillation frequency appeared to have no effect on the TPP in both the equatorial and meridional planes.

The subsolar magnetopause position is a critical space weather parameter. Satellites on the dayside might be exposed to the harsh environment of the magnetosheath during a large geomagnetic storm or large-scale fluctuations in the solar wind. The dynamic pressure is the single most important factor in determining the magnetopause location [Martyn, 1951]. Precautions can be taken when a CME launches off the Sun. Satellites can visually see this event and can make estimates as to the impact it might have on Earth's magnetosphere; however, the one aspect of solar events

that cannot be determined visually is the embedded magnetic field. This will not be known until the structure flies past the L1 Lagrange point. The IMF will also have an impact on the location of the magnetopause, as it moves inward with southward IMF under constant pressure, an effect known as magnetopause erosion [Aubrey et al., 1970]. Previous work on magnetopause erosion using MHD has been mostly with steady state solar wind inputs [e.g. Wiltberger et al., 2003].

The work presented here showed that the dayside magnetopause undergoes a "breathing" motion under solar wind fluctuations and exhibits a hysteresis-like effect. The *Wiltberger et al*. (2003) study using LFM showed a two-stage process of magnetopause erosion under constant solar wind, with the majority of the erosion occurring 20 minutes after the arrival of the southward IMF. This is due to the buildup of the cross-tail current, which produces a magnetic field that opposes Earth's dayside magnetic field, thus reducing the magnetic pressure and allowing the magnetopause to move inward. We showed that while the IMF is constantly changing, the magnetopause lag time to respond was roughly 10 minutes.

We showed that the amplitude of the subsolar magnetopause position was proportional to the amplitude of the input solar wind B_Z amplitude, with the response diminishing with large magnitude B_Z values, as it enters the saturation regime of magnetopause erosion. The main aspect of this magnetopause breathing mode is that there are situations where the subsolar magnetopause position will never relax to steady state values. This means that empirical models of the dayside magnetopause must account for the time history of the solar wind.

We presented the LFM simulation of a HSS that occurred from 14-19 September 2017. During the HSS, the magnetopause crossed over THEMIS several times. We showed the comparisons between the THEMIS magnetopause crossing, LFM, and

empirical models. LFM did significantly better than the *Roelof & Sibeck* (1993) model, which is the model used on NASA's Satellite Situation Center (SSC). There were times when this model's prediction was over 1 R_E away from the actual magnetopause location. LFM was comparable to the *Petrinec & Russell* (1996) model, but the *Shue et al*. (1998) model had the best results. The particular HSS showed was not all that dissimilar from ambient solar wind conditions and the *Shue et al*. (1998) model outperforms the rest during these conditions; however, had the Alfvénic fluctuations been larger, LFM would have performed at least as well as *Shue et al.* (1998), as seen during the Halloween Storms [Lopez et al., 2007]. It is still clear that the other models still miss the mark at certain times and should possibly be modified to include the time history of the solar wind.

6.2 Future Work

The model/data comparison of the HSS showed how the magnetopause position is difficult to determine for most of the HSS. Only 8 clean crossings were identified near the subsolar point. A further study of HSS should move to include other THEMIS parameters in order to identify crossings that otherwise might have been determined to be dirty. Another obvious extension to this study is to include crossings during northward IMF; however, this cannot be done with B_Z and the ESA alone. This particular HSS is currently being studied more in depth and will eventually be written as a paper to be submitted. Future work in this area would be to analyze more HSS; however, there will be some difficulty in determining magnetopause crossings as most of the other HSS we looked at had a very small number of crossings. Combining both northward and southward IMF crossings and the identification & inclusion of crossings that were not deemed "clean" by this study would make for a nice extension to this work.

The difficulty in determining northward IMF magnetopause positions lies in the amount of computation time needed to trace magnetic field lines. At present, a further analysis is being done using dynamic pressure as a proxy for the subsolar magnetopause position. This will complement the previous studied presented in chapter 4. Magnetic field lines could be traced at various points throughout the cycles in order to verify the dynamic pressure method without using too much time. An extension to this study could include the magnetopause response time as a function of IMF magnitude. How fast does the magnetopause respond from say -5 nT to -10 nT as opposed to +5 nT to -10 nT?

One major study that was going to be included in this work is an extension to include the outer planets. As mentioned in chapter 3, the IMF is mostly in the B_Y direction when it reaches the outer planets [Masters et al., 2014]. Magnetic reconnection is significantly reduced at this point and the viscous interaction would be much more important. We originally intended to modify LFM to adapt one of the Jovian planet's magnetospheres (possibly Saturn or Uranus). Our plan included a series of numerical experiments to determine how crucial the viscous interaction is in the solar wind-magnetosphere coupling on one of these planets. Due to the shift in focus from the viscous interaction to the dayside magnetopause, this study was never carried out and would be a nice extension to this work.

Finally, the results presented here lacked two major contributions to the magnetopause position: the ring current and ionospheric outflow. LFM does not include these effects into the code. The ring current buildup will compress Earth's magnetic field, thus allowing the magnetopause to move earthward under constant pressure. LFM has the option to be run with the Rice Convection Model (RCM) [Toffoletto et al., 2003]. An

extension to this study could be to run LFM using the RCM and see how the results would differ.

The high-speed stream in chapter 5 was selected partially because the event lacked a significant ring current, and thus, would allow for better predictions in LFM. An enhanced ring current is the principle defining property of a magnetic storm [Gonzalez et al., 1994]. The intensity of a magnetic storm can be classified based on the *Dst* (disturbance storm time) index.

The ring current produces a magnetic field that opposes Earth's magnetic dipole. Therefore, an enhanced ring current will reduce the magnetic field measured on the surface of Earth. A series of magnetometers are set up near the equator around the world to measure this magnetic field reduction. A negative *Dst* value indicates that Earth's magnetic field has weakened in response to an enhanced ring current. The *Dst* index is the hourly average of the magnetometers. A 1-min. analogue to *Dst* is *SYM-H* (symmetric horizontal). Figure 6-1 shows the *SYM-H* values for the duration of the 14-19 September 2017 high-speed stream. At no time does the *SYM-H* value ever get far below -40 nT. This would be classified as a weak geomagnetic storm and therefore, the enhancement of the ring current is minimal [Gonzalez et al., 1994].

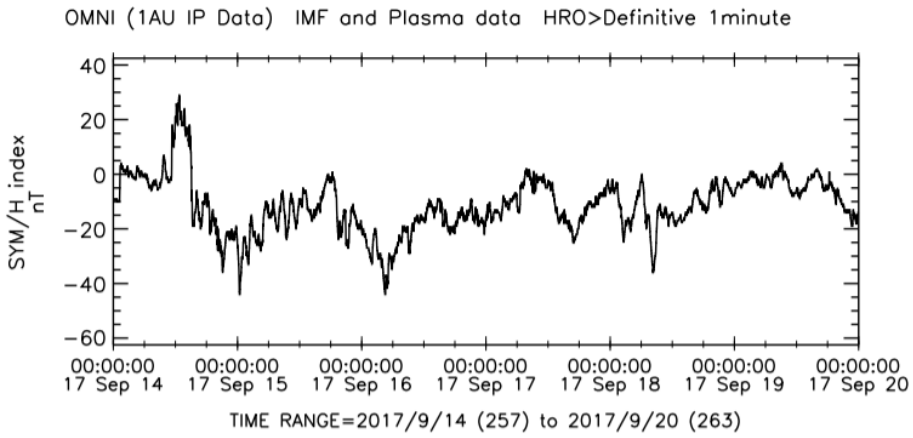

Figure 6-1 SYM-H OMNI data for the 14-19 September 2017 high-speed stream [NASA/GSFC/CDAWeb/OMNI].

Ionospheric H^+, He^+, and O^+ are accelerated into the magnetosphere causing the ring current to energize, further compressing Earth's magnetic field [Welling et al., 2015]. Ionospheric outflow can be adapted into LFM using a multifluid version of LFM [Wiltberger et al., 2010; Garcia et al., 2010]. This version of LFM could be used in conjunction with RCM, as suggested by *Pembroke et al*. (2012).

How the magnetopause responds to atypical solar wind and enhanced geospace conditions is an interesting subject that should be studied in greater detail.

Appendix A

Empirical Models of the Magnetopause used in Comparison with LFM

The empirical models used in this work depend on three parameters: B_Z (IMF B_Z in nT), D_p (solar wind dynamic pressure in nPa), and θ (solar zenith angle). Since this work was focused on the subsolar magnetopause location ($Y = Z = 0$), the solar zenith angle used is 0^o and the tail flaring was neglected.

***Roelof & Sibeck* (1993)**

$$R^2 + S_1X^2 + S_2X + S_3 = 0$$

where $R^2 = Y^2 + Z^2$ and X, Y, Z are coordinates in GSE (geocentric solar ecliptic). In GSE, the X-axis is along the Sun-Earth line (see figures 1-15 & 1-16). The Y-axis is towards dusk in the ecliptic plane, and the Z-axis is perpendicular to the ecliptic plane. The X-axis is the same for all three coordinate systems: $X_{SM} = X_{GSM} = X_{GSE}$. S_1, S_2, and S_3 are functions of D_p and B_Z and are given by,

$$S_1 = -1.764 - 0.299p_1 - 0.151b_1 - 0.246p_1^2 + 0.05p_1b_1 + 0.476b_1^2$$

$$S_2 = 2.934 - 0.076p_1 - 0.129b_1 - 0.012p_1^2 + 0.079p_1b_1 + 0..0026b_1^2$$

$$S_3 = 5.397 - 0.183p_1 - 0.041b_1 - 0.044p_1^2 + 0.04p_1b_1 + 0.02b_1^2$$

with,

$$p_1 = \log_2(D_p/2)$$

$$b_1 = B_Z/3.5$$

For the subsolar magnetopause position, $R = 0$ and the subsolar magnetopause position is determined by a simple quadratic equation: $S_1X^2 + S_2X + S_3 = 0$. The range of validity for this model is -5 nT < B_Z < 5 nT and 0.5 nPa < D_p < 8 nPa.

***Petrinec & Russell* (1996)**

$$r = \frac{14.63\left(\frac{D_p}{2.1}\right)^{-1/6}}{1+\left(\frac{14.63}{10.3+m_1 B_Z}-1\right)cos\theta}$$

where m_1 = 0 for northward IMF and m_1 = 0.16 for southward IMF. The range of validity for this model is -10 nT < B_Z < 10 nT and 0.5 nPa < D_p < 8 nPa.

***Shue et al*. (1998)**

$$r = r_0\left(\frac{2}{1+cos\theta}\right)^{\alpha}$$

where α is the level of tail flaring [$\alpha = (0.58 - 0.010B_Z)(1 + 0.010D_p)$]. The standoff at the subsolar point, r_0, was determined by *Shue et al*. (1997) by using a bivariant best fit:

$$r_0 = \begin{cases} (11.4 + 0.013B_Z)(D_p)^{-\frac{1}{6.6}}, & B_Z \geq 0 \\ (11.4 + 0.14B_Z)(D_p)^{-\frac{1}{6.6}}, & B_Z < 0 \end{cases}$$

The range of validity of this model is for -18 nT < B_Z < 15 nT and 0.5 nPa < D_p < 8.5 nPa.

Appendix B

Summary Graphs for the 8 THEMIS Crossings

during the 14-19 September 2017 HSS

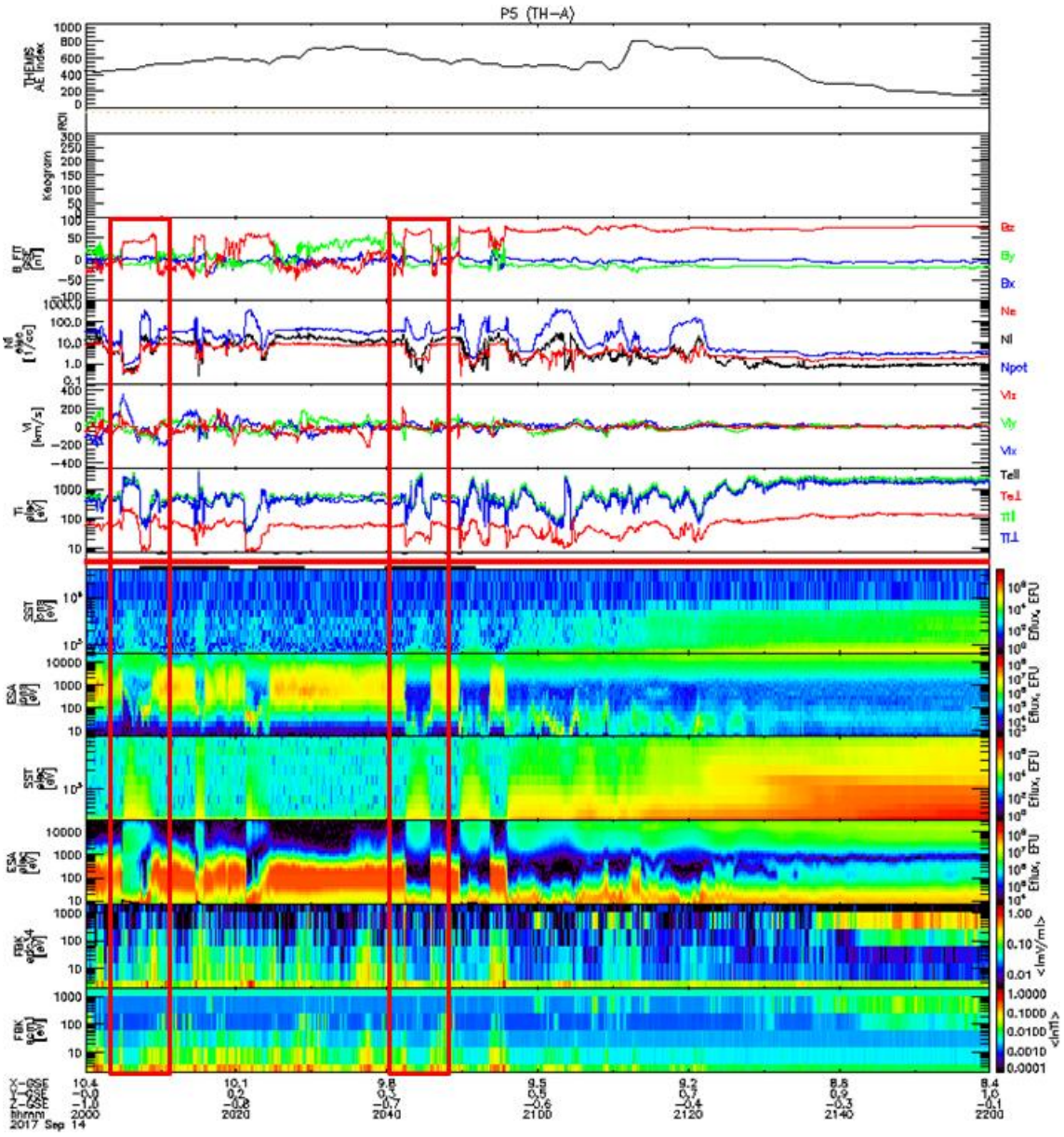

THEMIS A (P5) summary plot for 20:00 UT to 22:00 UT on September 14, 2017. THEMIS A crosses the magnetopause 4 times during this 2-hour time span (boxed in red): 20:05 UT, 20:09 UT, 20:42 UT, and 20:46 UT.

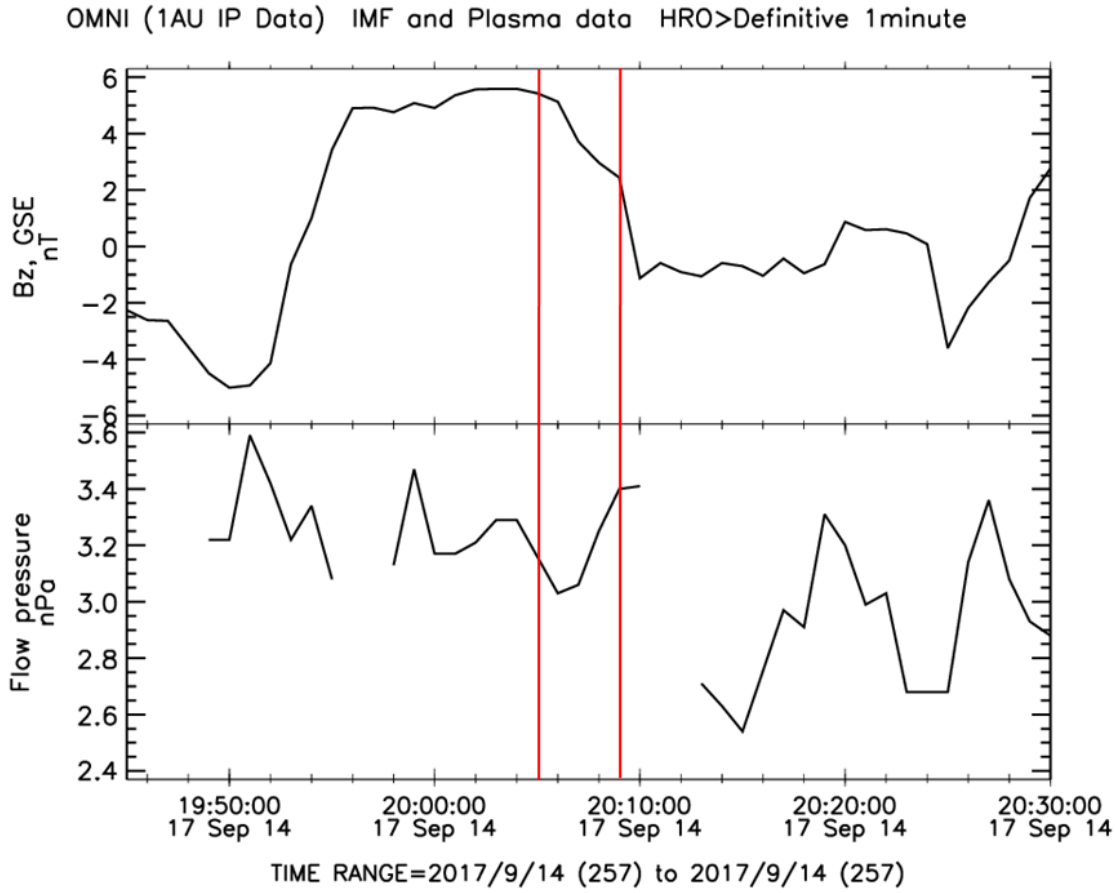

OMNI solar wind data for 19:45 UT to 20:30 UT on September 14, 2017. THEMIS A crosses the magnetopause at 20:05 UT and 20:09 UT (both marked in red).

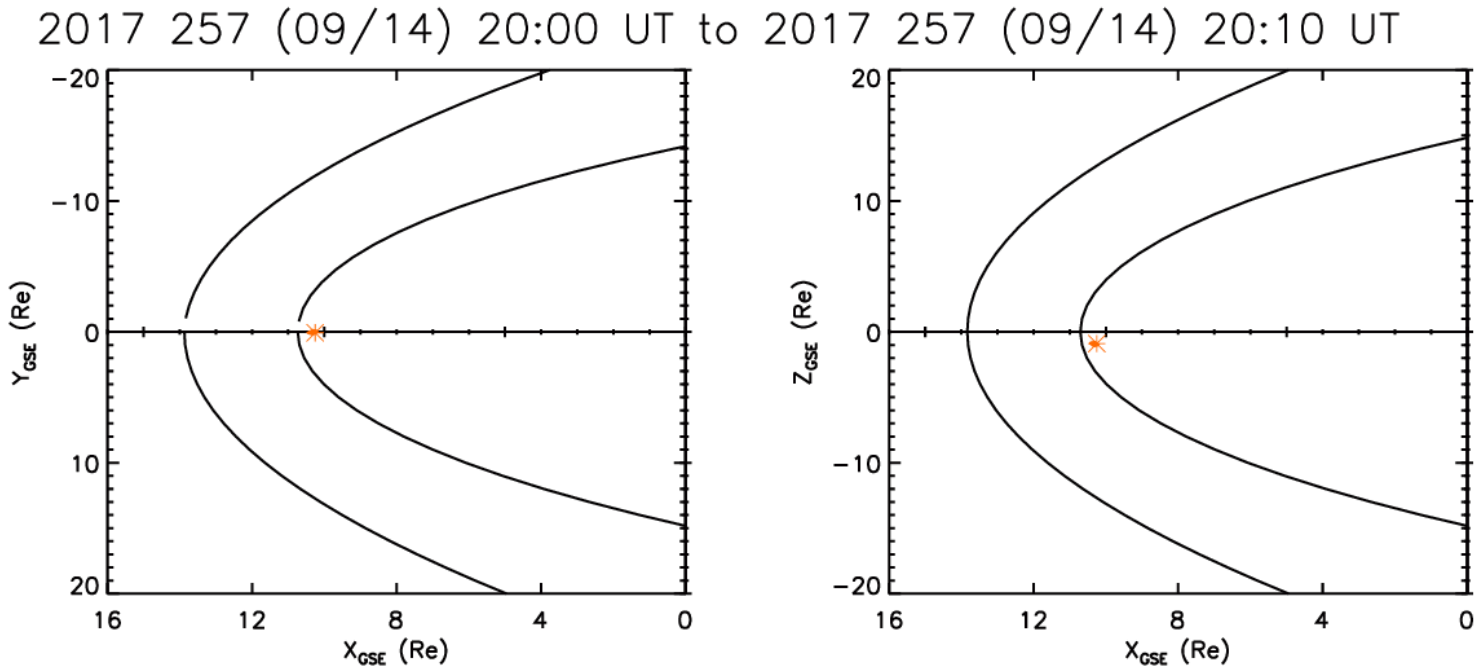

SSC position plot of THEMIS A (orange) for 20:00 UT to 20:10 UT on September 14, 2017. The line closest to THEMIS A is the magnetopause for a solar wind dynamic pressure of 2 nPa and 0 IMF. The other line is the bow shock for the same conditions. THEMIS A crosses the magnetopause at 20:05 UT and 20:09 UT.

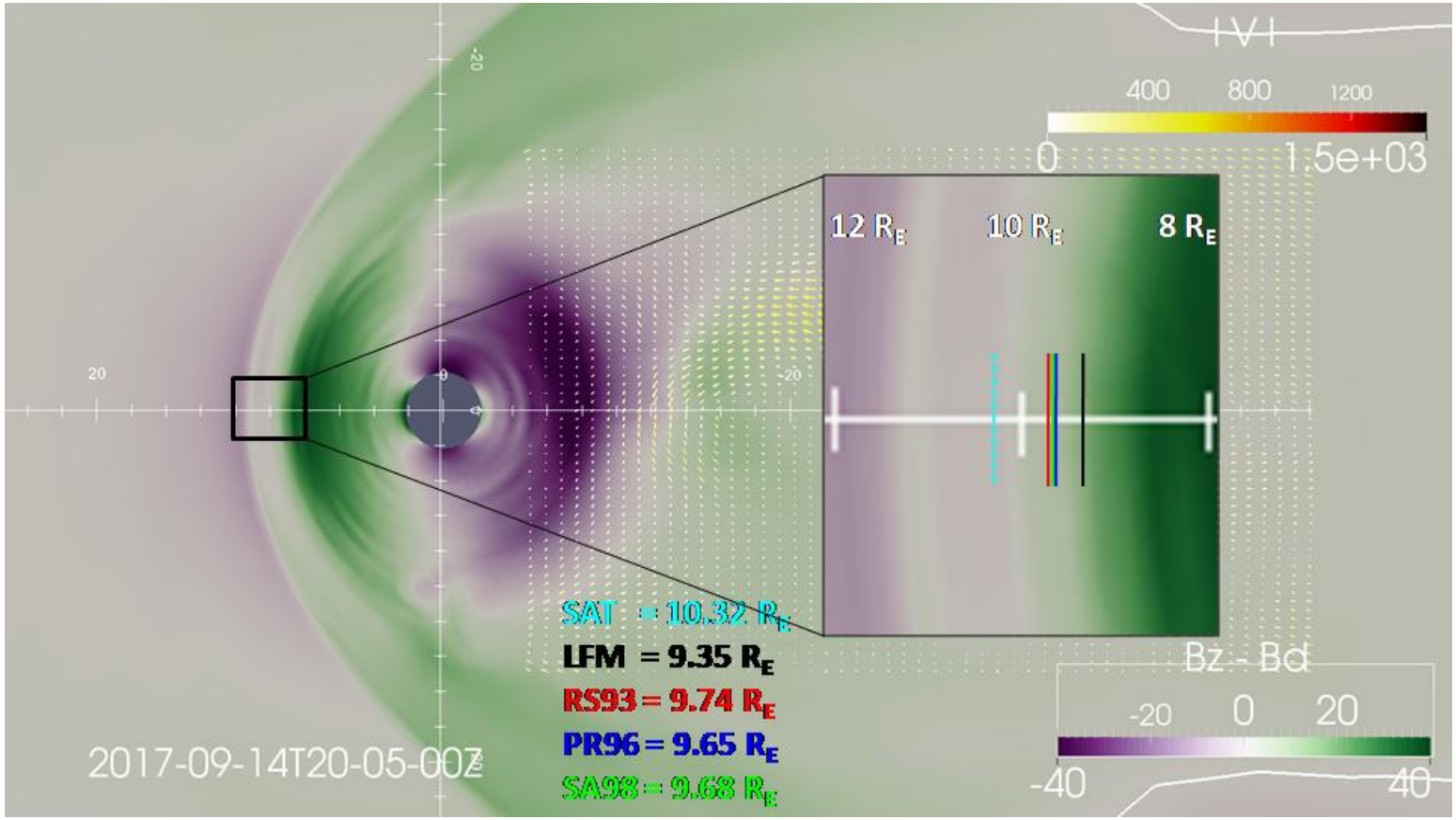

Equatorial plane view for the September 14, 2017 20:05 UT crossing of THEMIS A, in LFM color-coded for Earth's magnetic dipole subtracted from B_Z at that location. The turquoise "SAT" line is the location that THEMIS crosses the magnetopause (X coordinate only). The red, blue, and green lines are the empirical model predictions of the subsolar magnetopause location.

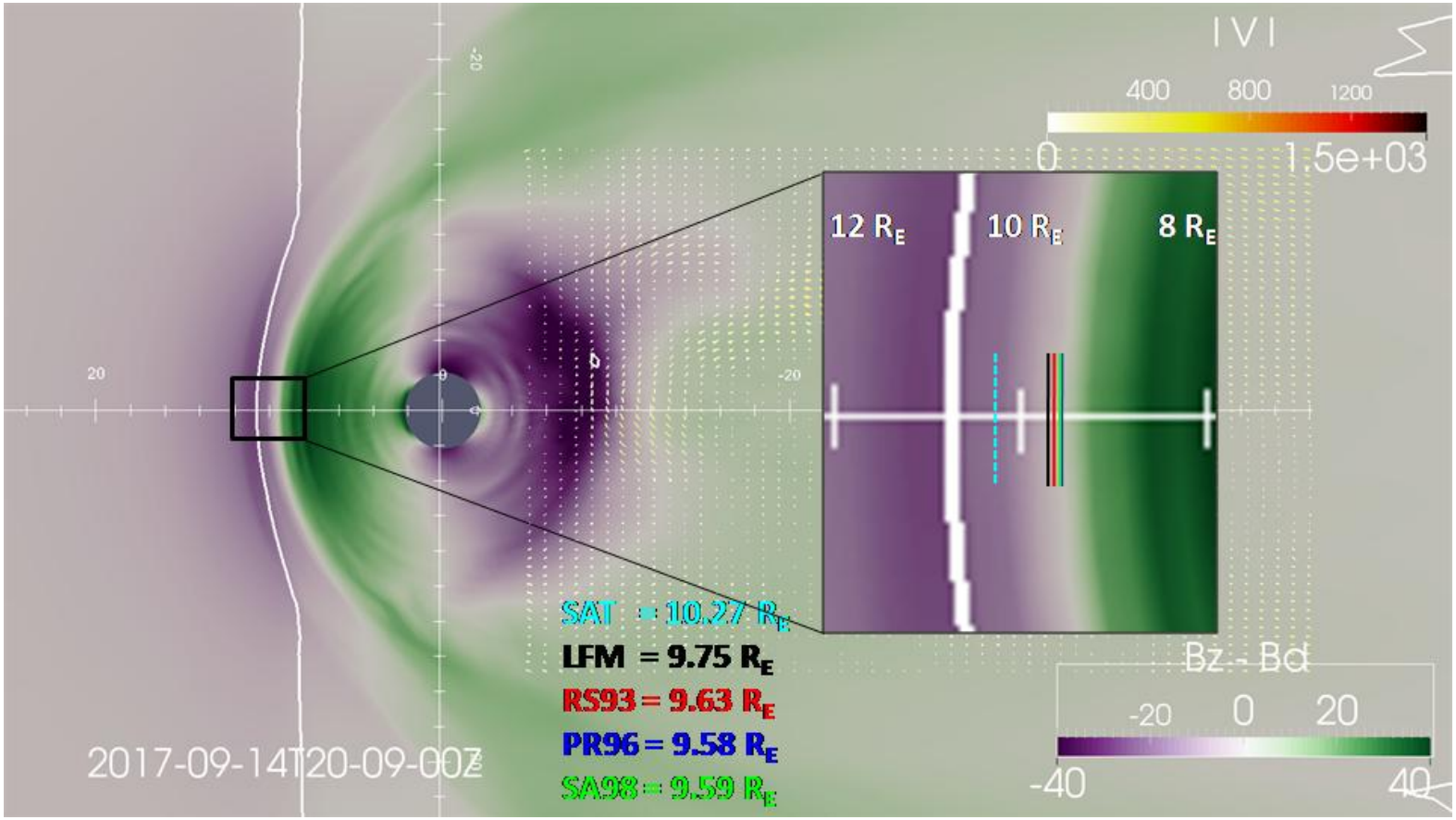

Equatorial plane view for the September 14, 2017 20:09 UT crossing of THEMIS A, in LFM color-coded for Earth's magnetic dipole subtracted from B_Z at that location. The turquoise "SAT" line is the location that THEMIS crosses the magnetopause (X coordinate only). The red, blue, and green lines are the empirical model predictions of the subsolar magnetopause location.

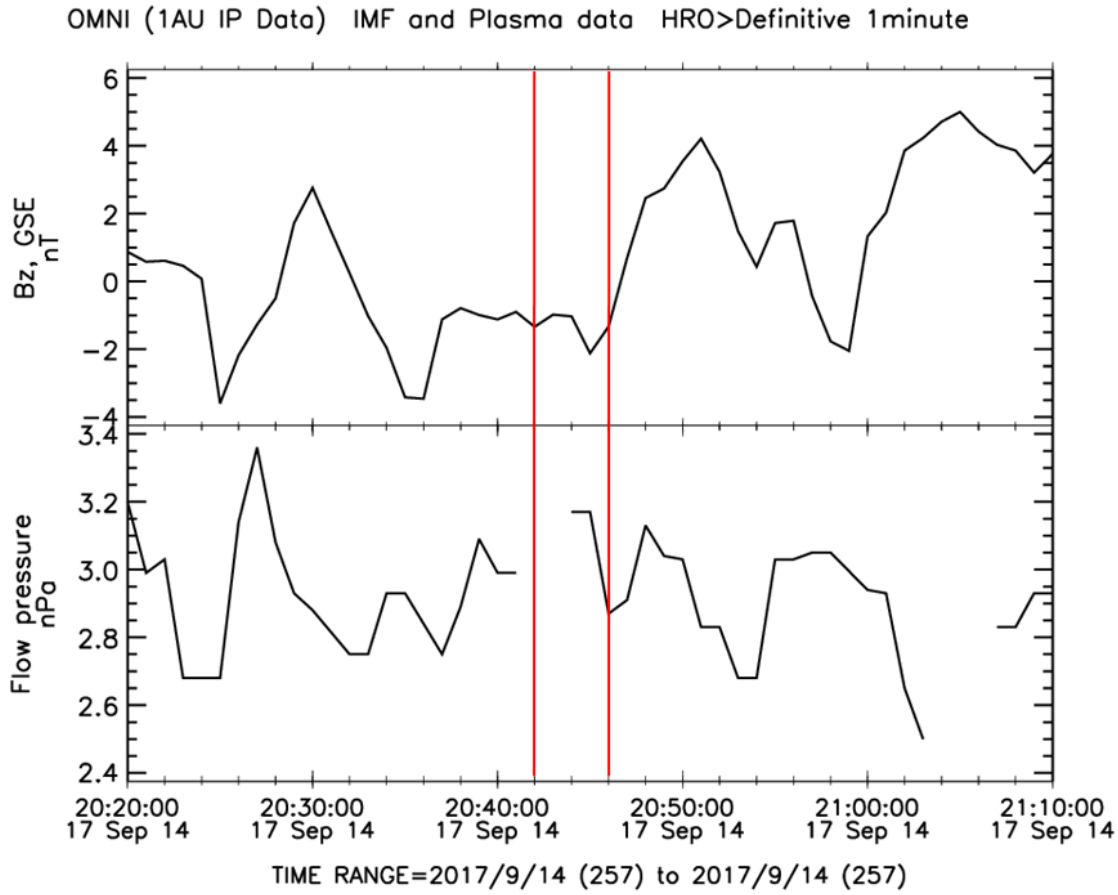

OMNI solar wind data for 20:20 UT to 21:10 UT on September 14, 2017. THEMIS A crosses the magnetopause at 20:42 UT and 20:46 UT (both marked in red).

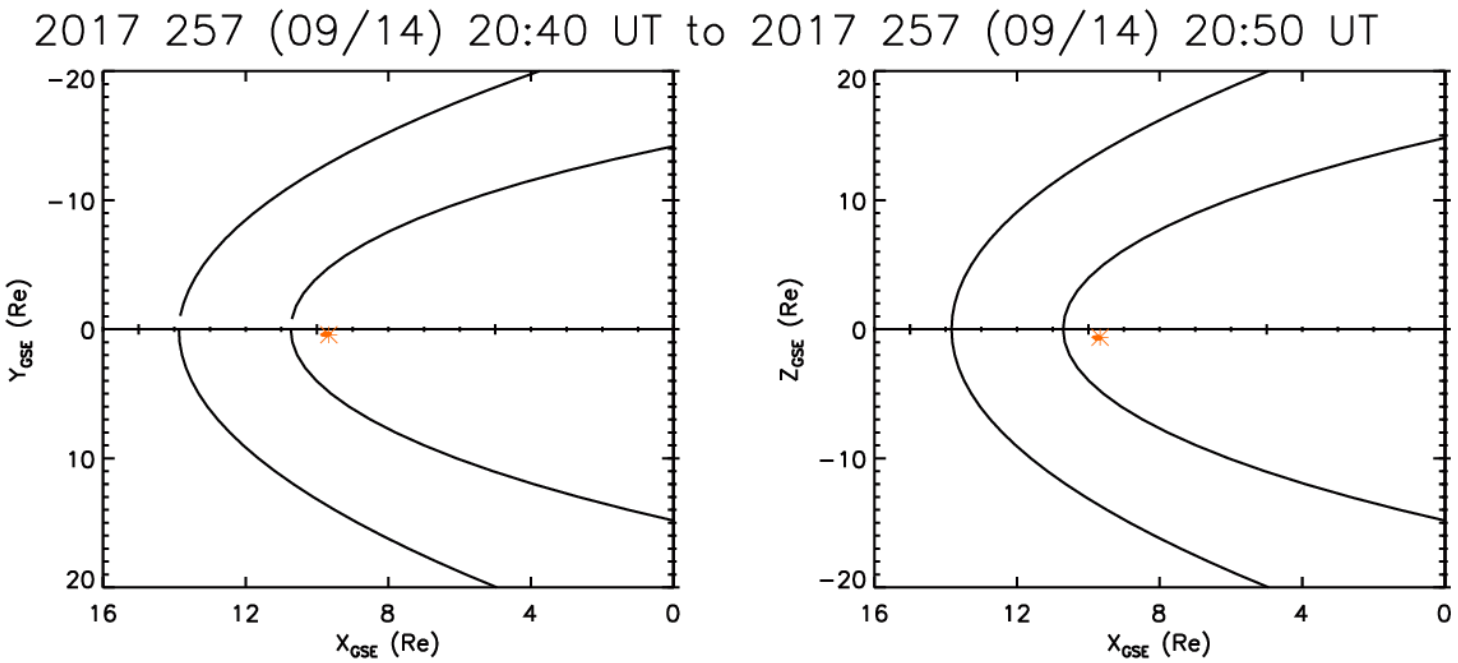

SSC position plot of THEMIS A (orange) for 20:40 UT to 20:50 UT on September 14, 2017. The line closest to THEMIS A is the magnetopause for a solar wind dynamic pressure of 2 nPa and 0 IMF. The other line is the bow shock for the same conditions. THEMIS A crosses the magnetopause at 20:42 UT and 20:46 UT.

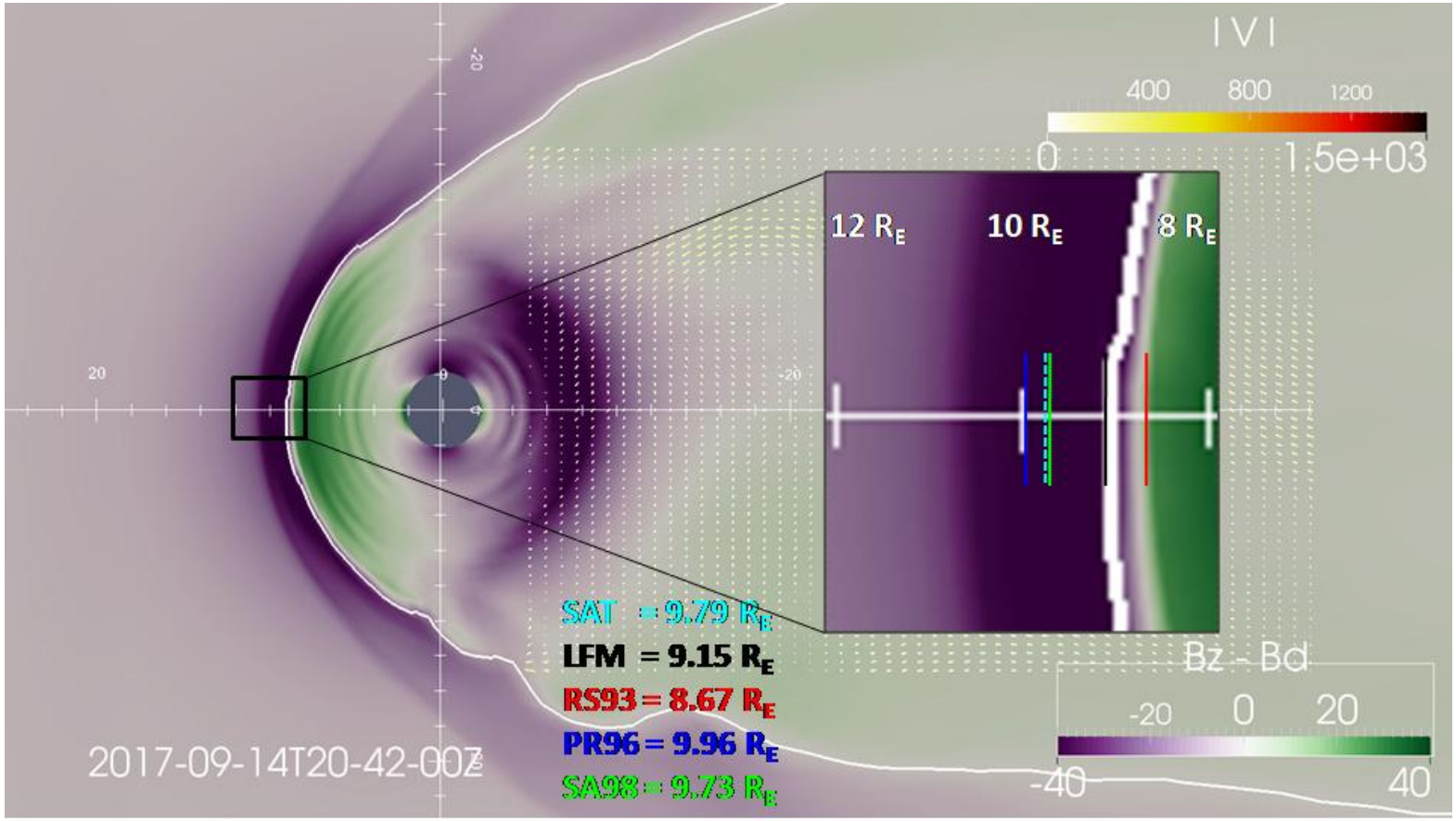

Equatorial plane view for the September 14, 2017 20:42 UT crossing of THEMIS A, in LFM color-coded for Earth's magnetic dipole subtracted from B_Z at that location. The turquoise "SAT" line is the location that THEMIS crosses the magnetopause (X coordinate only). The red, blue, and green lines are the empirical model predictions of the subsolar magnetopause location.

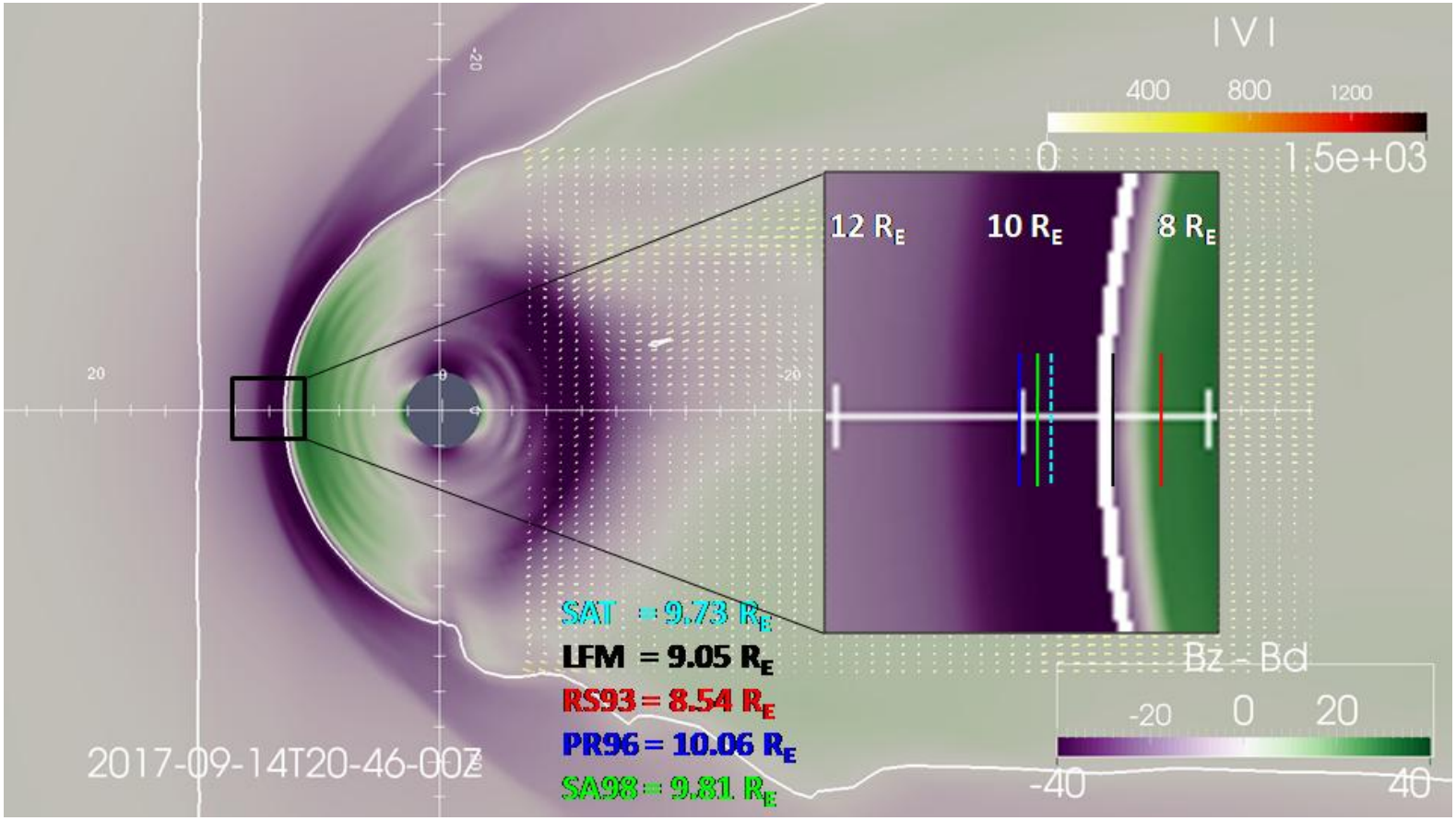

Equatorial plane view for the September 14, 2017 20:46 UT crossing of THEMIS A, in LFM color-coded for Earth's magnetic dipole subtracted from B_Z at that location. The turquoise "SAT" line is the location that THEMIS crosses the magnetopause (X coordinate only). The red, blue, and green lines are the empirical model predictions of the subsolar magnetopause location.

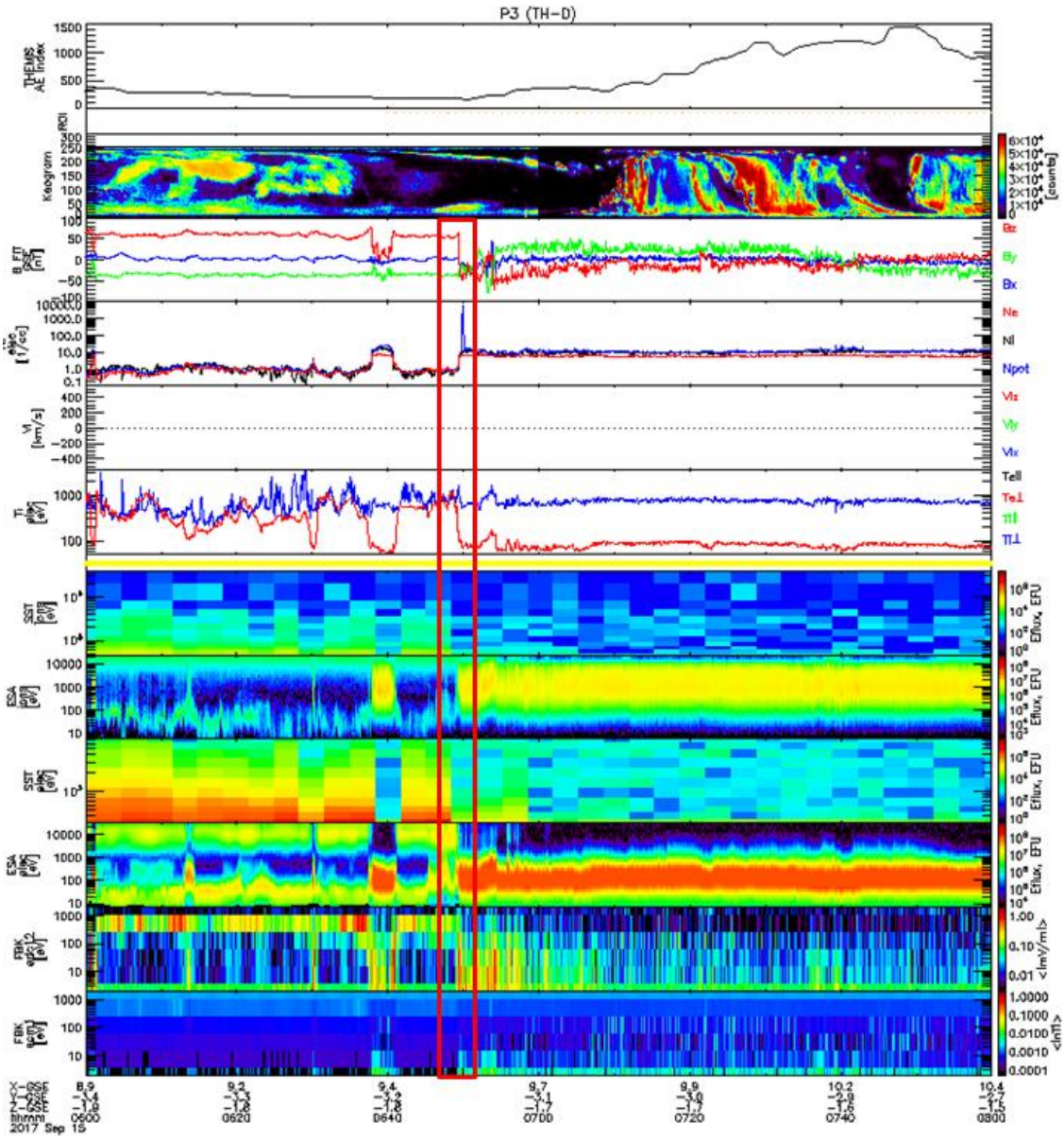

THEMIS D (P3) summary plot for 06:00 UT to 08:00 UT on September 15, 2017. THEMIS D crosses the magnetopause (boxed in red) at 06:49 UT.

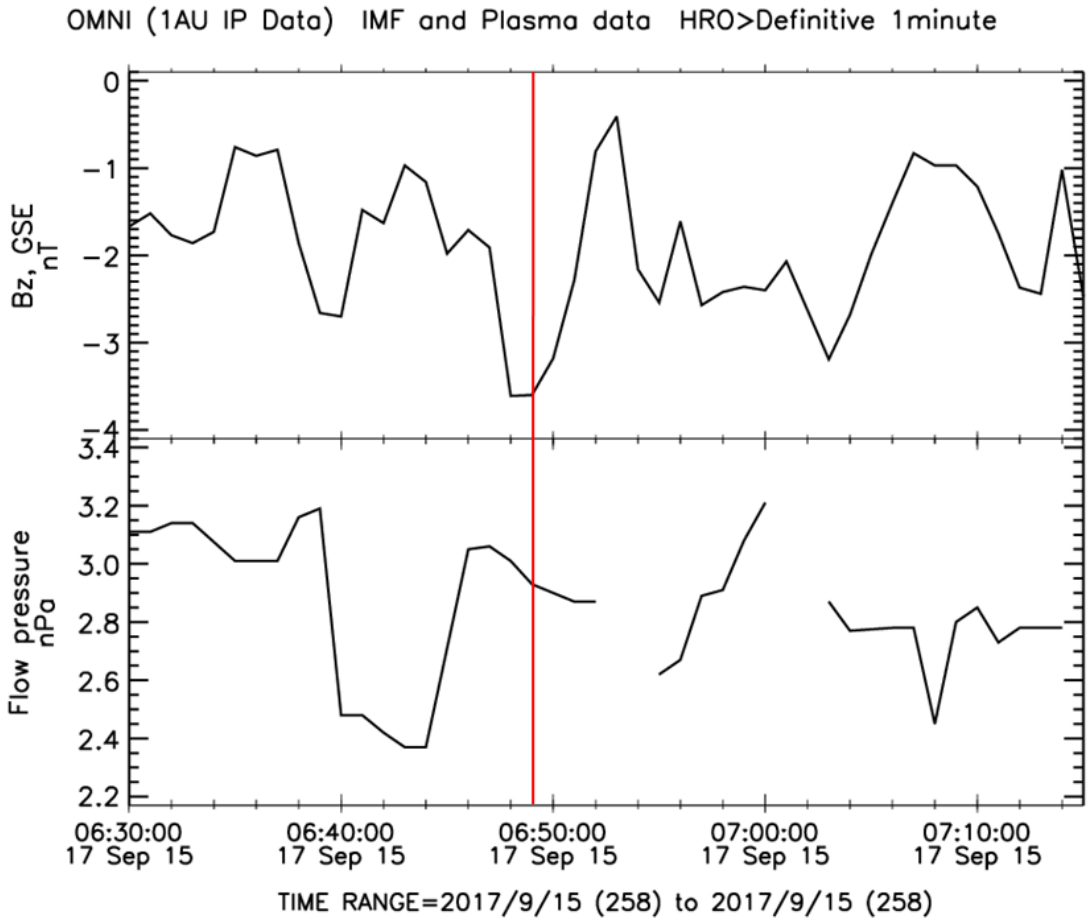

OMNI solar wind data for 06:30 UT to 07:10 UT on September 15, 2017. THEMIS D crosses the magnetopause at 06:49 UT (marked in red).

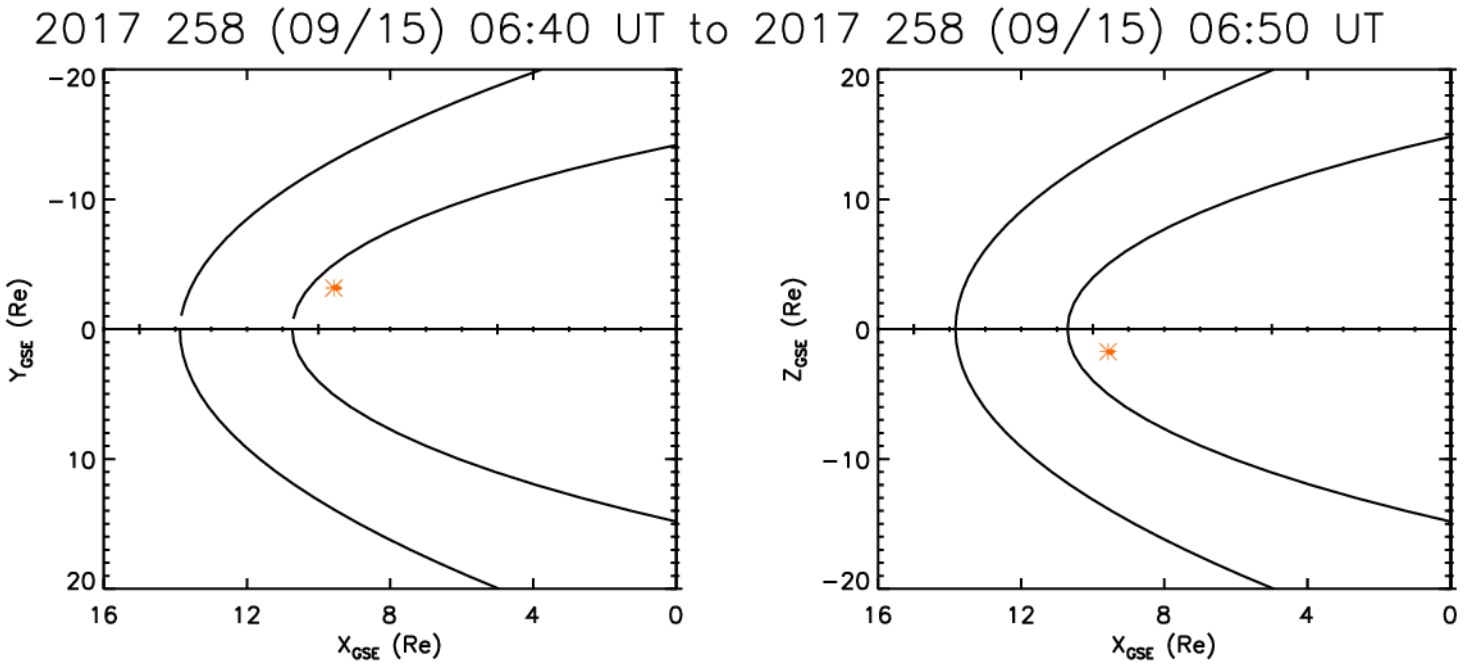

SSC position plot of THEMIS D (orange) for 06:40 UT to 06:50 UT on September 15, 2017. The line closest to THEMIS D is the magnetopause for a solar wind dynamic pressure of 2 nPa and 0 IMF. The other line is the bow shock for the same conditions. THEMIS D crosses the magnetopause at 06:49 UT.

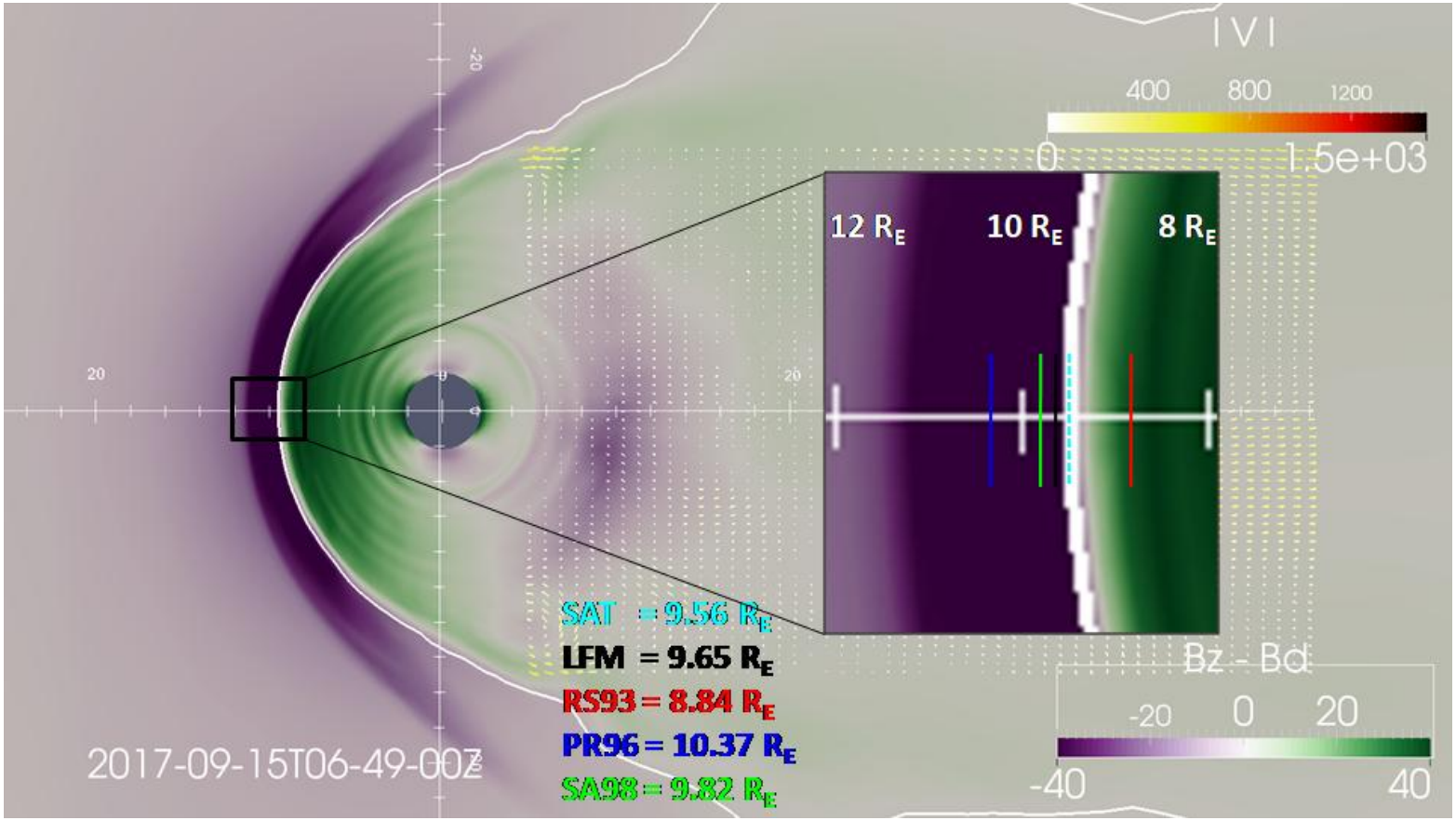

Equatorial plane view for the September 15, 2017 06:49 UT crossing of THEMIS D, in LFM color-coded for Earth's magnetic dipole subtracted from B_Z at that location. The turquoise "SAT" line is the location that THEMIS crosses the magnetopause (X coordinate only). The red, blue, and green lines are the empirical model predictions of the subsolar magnetopause location.

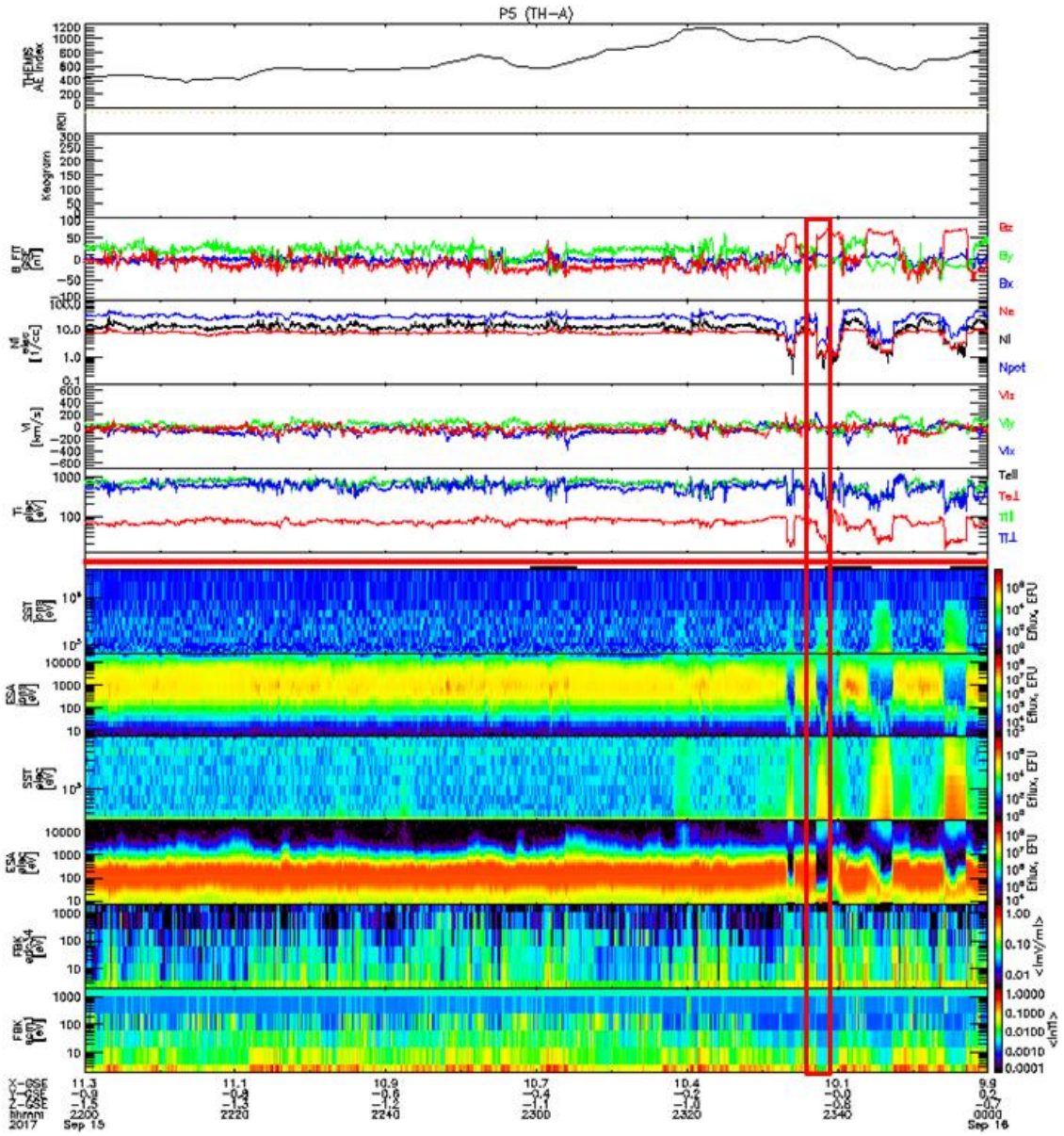

THEMIS A (P5) summary plot for 22:00 UT to 00:00 UT on September 15-16, 2017. THEMIS A crosses the magnetopause (boxed in red) at 23:37 UT.

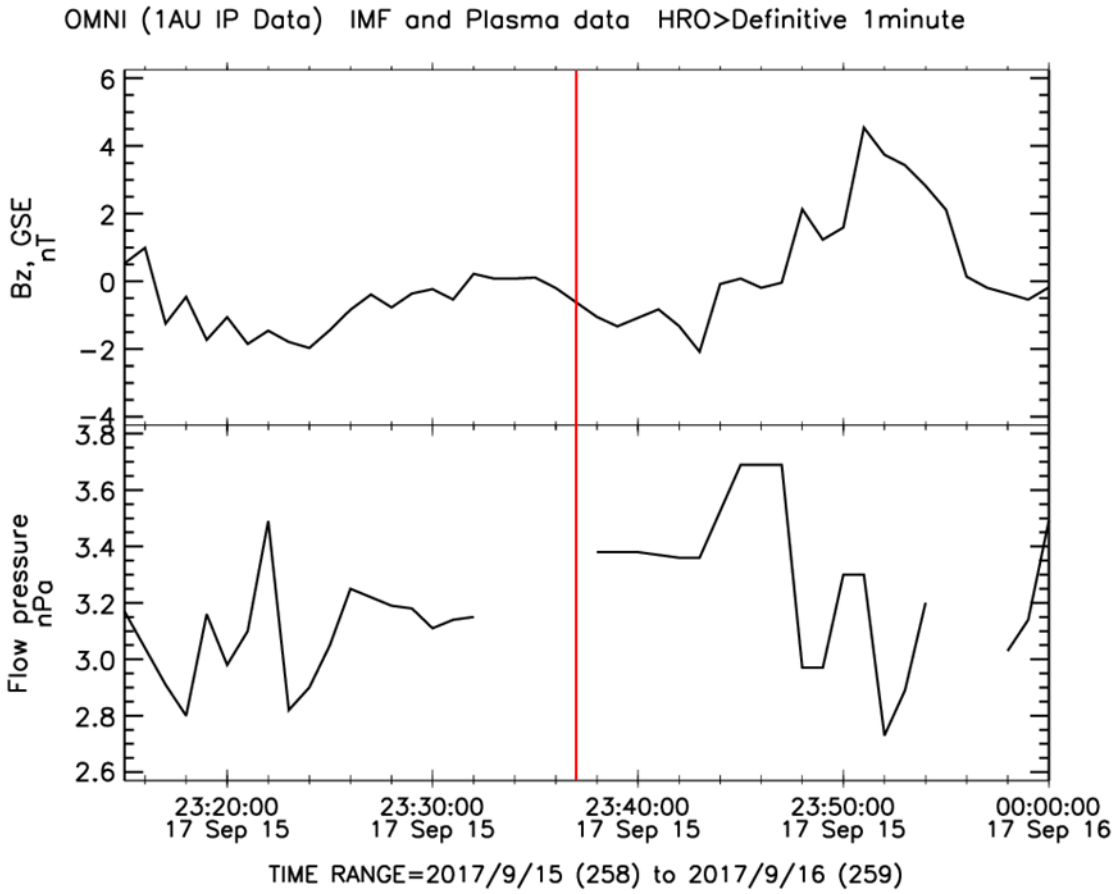

OMNI solar wind data for 23:20 UT to 00:00 UT on September 15-16, 2017. THEMIS A crosses the magnetopause at 23:37 UT (marked in red).

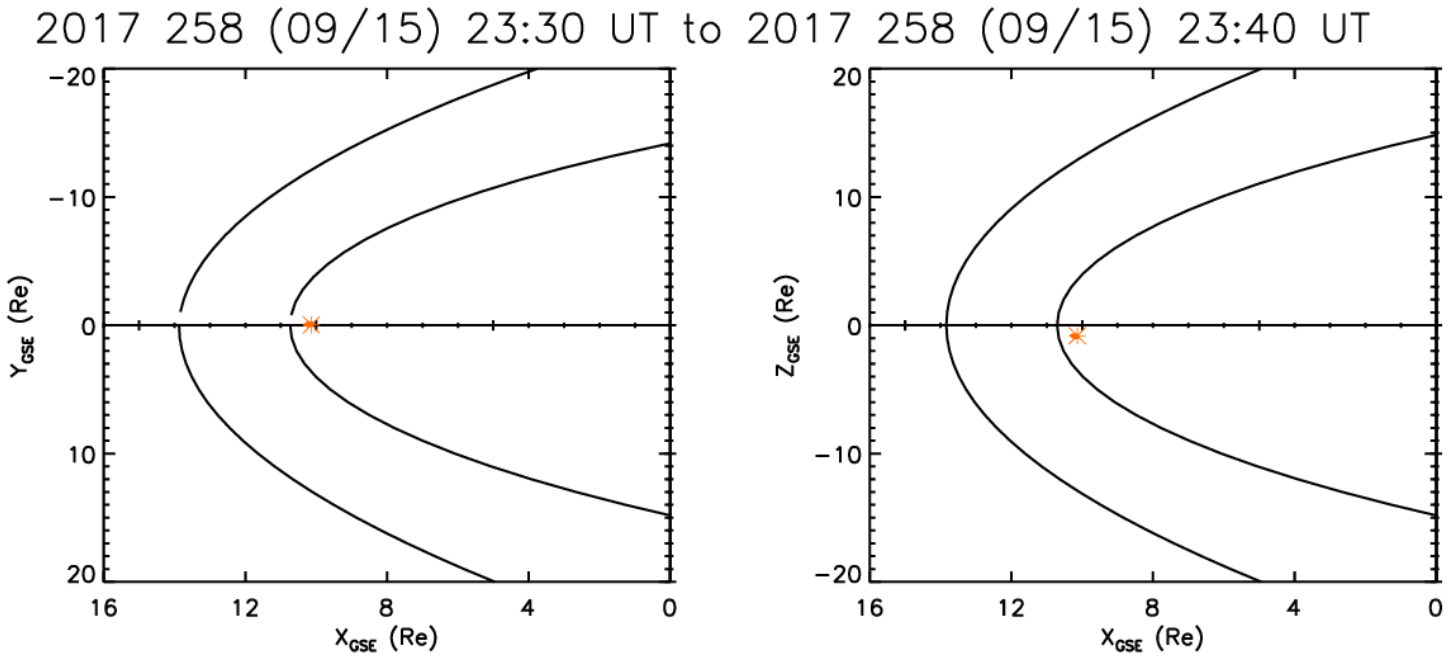

SSC position plot of THEMIS A (orange) for 23:30 UT to 23:40 UT on September 15, 2017. The line closest to THEMIS A is the magnetopause for a solar wind dynamic pressure of 2 nPa and 0 IMF. The other line is the bow shock for the same conditions. THEMIS A crosses the magnetopause at 23:37 UT

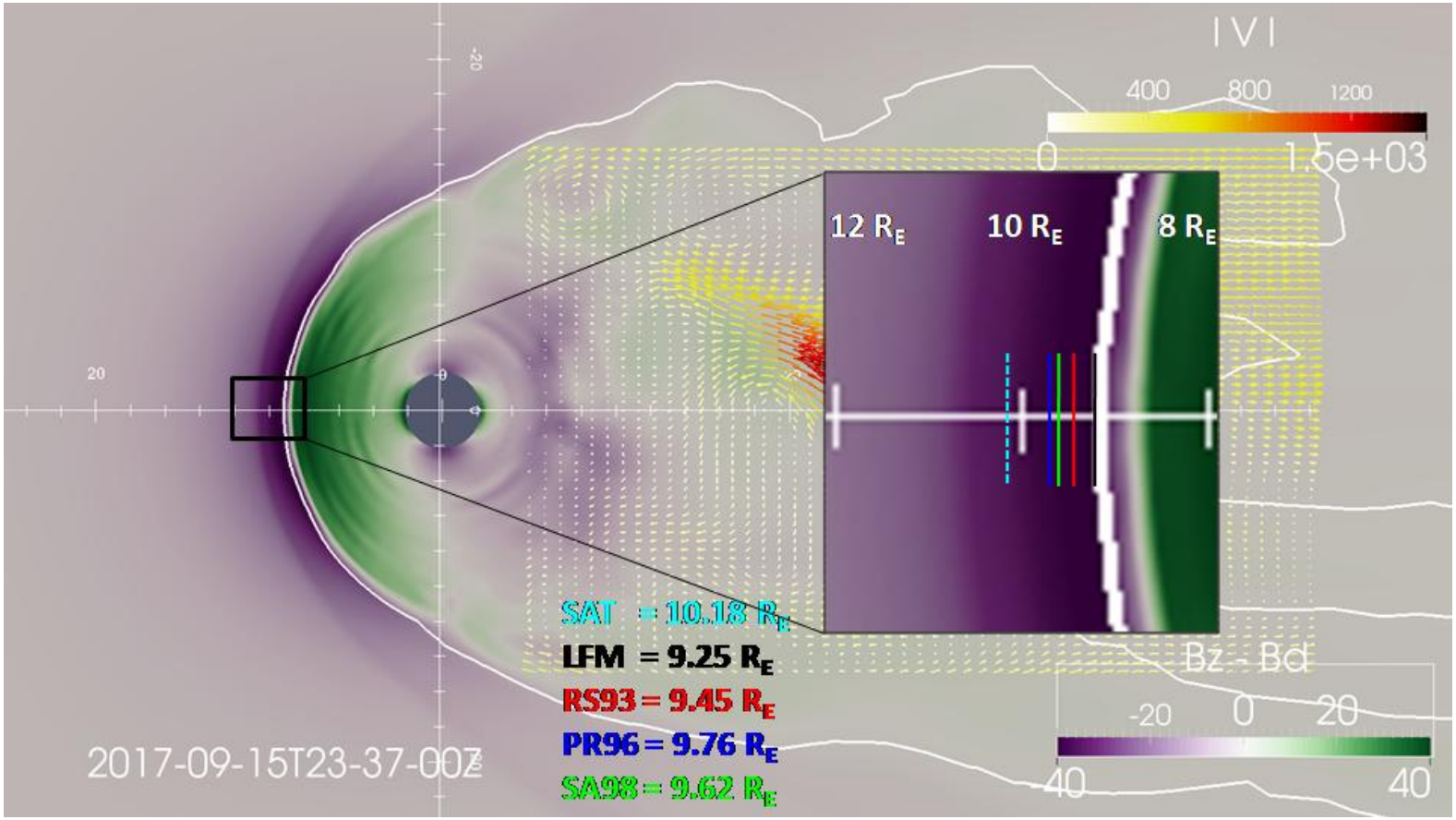

Equatorial plane view for the September 15, 2017 23:37 UT crossing of THEMIS A, in LFM color-coded for Earth's magnetic dipole subtracted from B_Z at that location. The turquoise "SAT" line is the location that THEMIS crosses the magnetopause (X coordinate only). The red, blue, and green lines are the empirical model predictions of the subsolar magnetopause location.

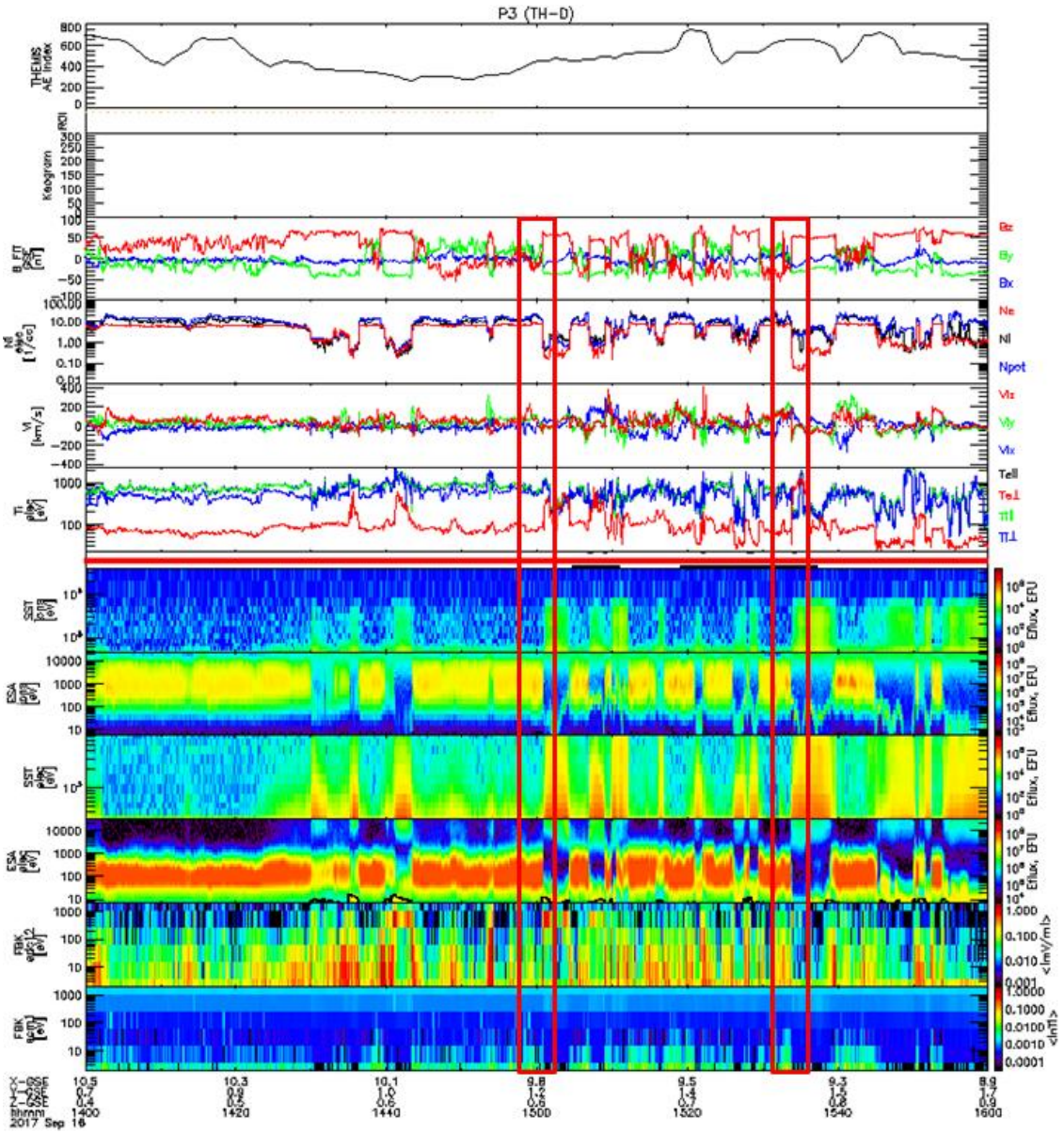

THEMIS D (P3) summary plot for 14:00 UT to 16:00 UT on September 16, 2017. T THEMIS A crosses the magnetopause at 15:00 UT and 15:33 UT (both boxed in red).

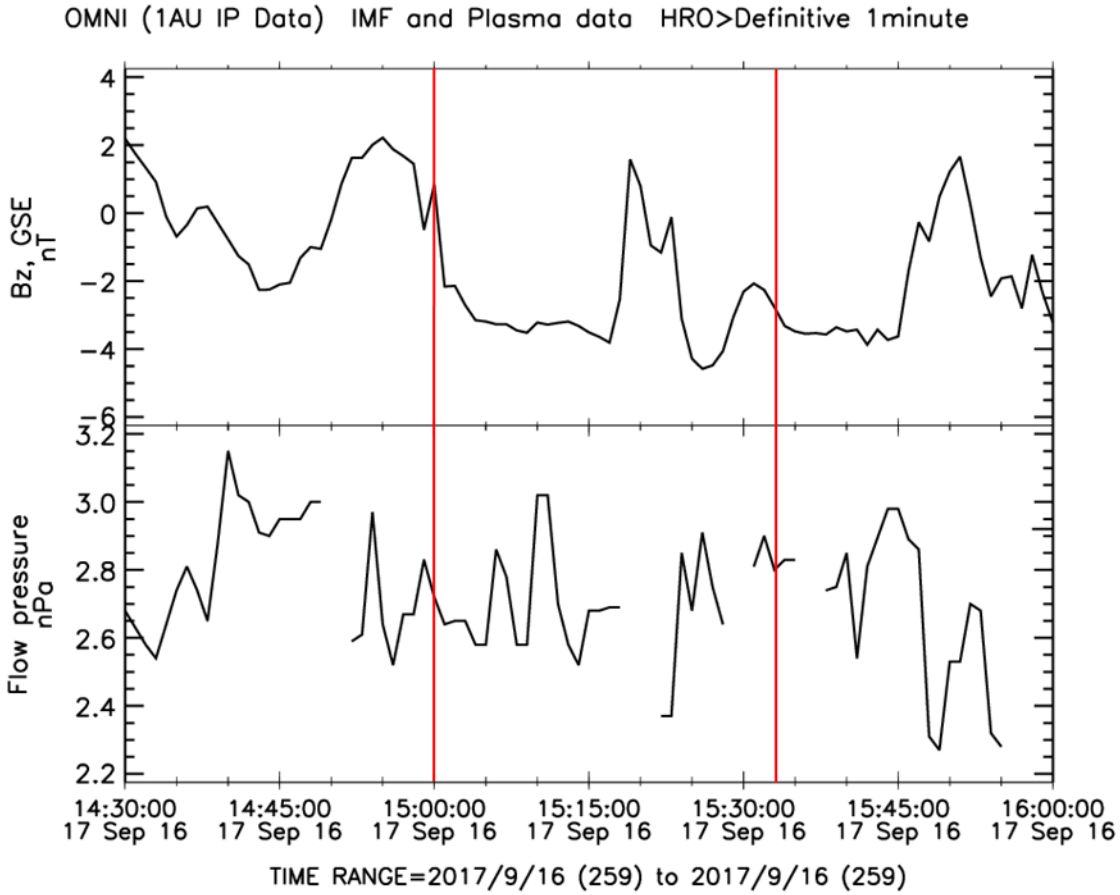

OMNI solar wind data for 14:30 UT to 16:00 UT on September 16, 2017. THEMIS A crosses the magnetopause at 15:00 UT and 15:33 UT (both marked in red).

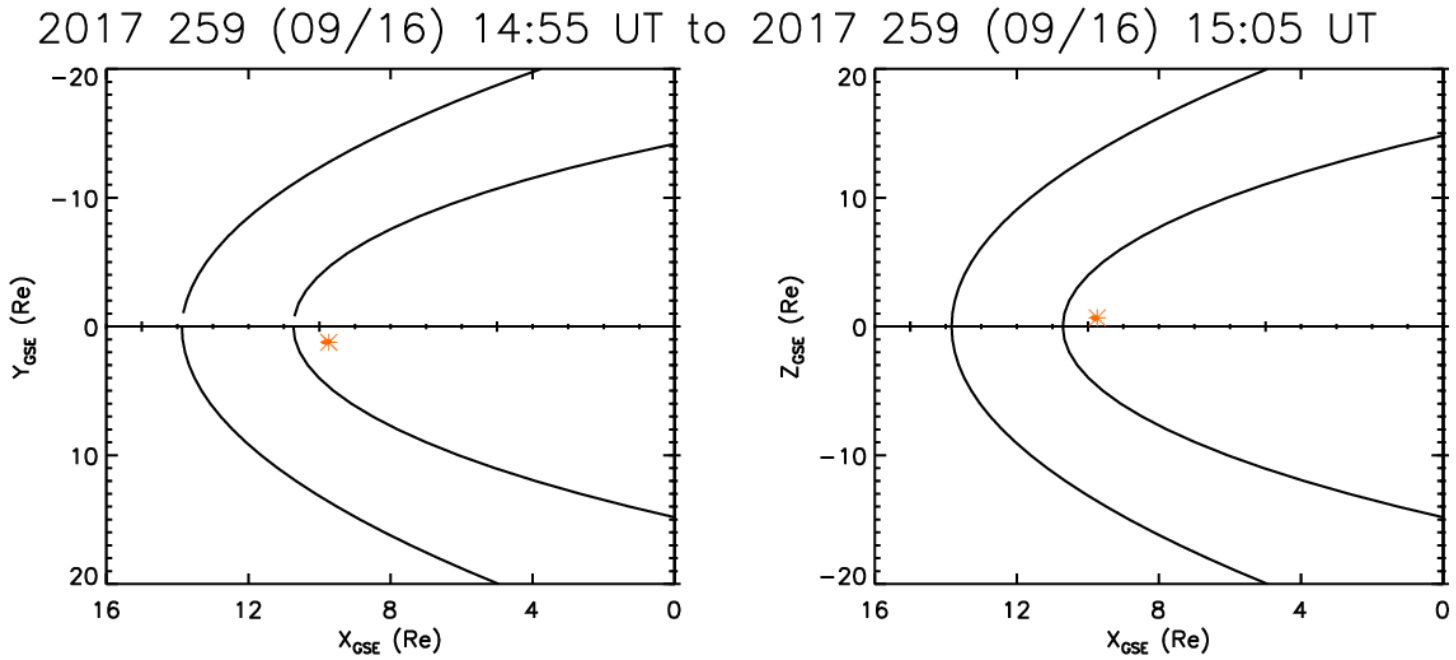

SSC position plot of THEMIS A (orange) for 14:55 UT to 15:05 UT on September 16, 2017. The line closest to THEMIS A is the magnetopause for a solar wind dynamic pressure of 2 nPa and 0 IMF. The other line is the bow shock for the same conditions. THEMIS A crosses the magnetopause at 15:00 UT

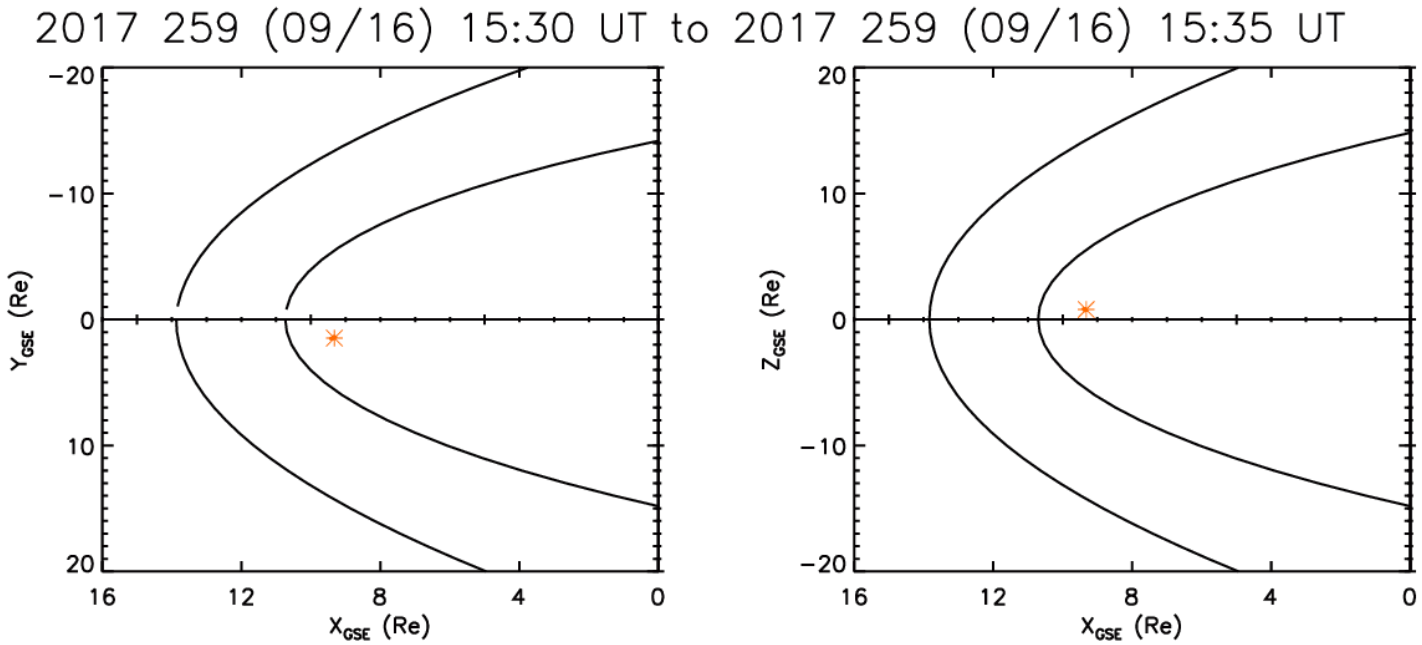

SSC position plot of THEMIS A (orange) for 15:30 UT to 15:35 UT on September 16, 2017. The line closest to THEMIS A is the magnetopause for a solar wind dynamic pressure of 2 nPa and 0 IMF. The other line is the bow shock for the same conditions. THEMIS A crosses the magnetopause at 15:33 UT

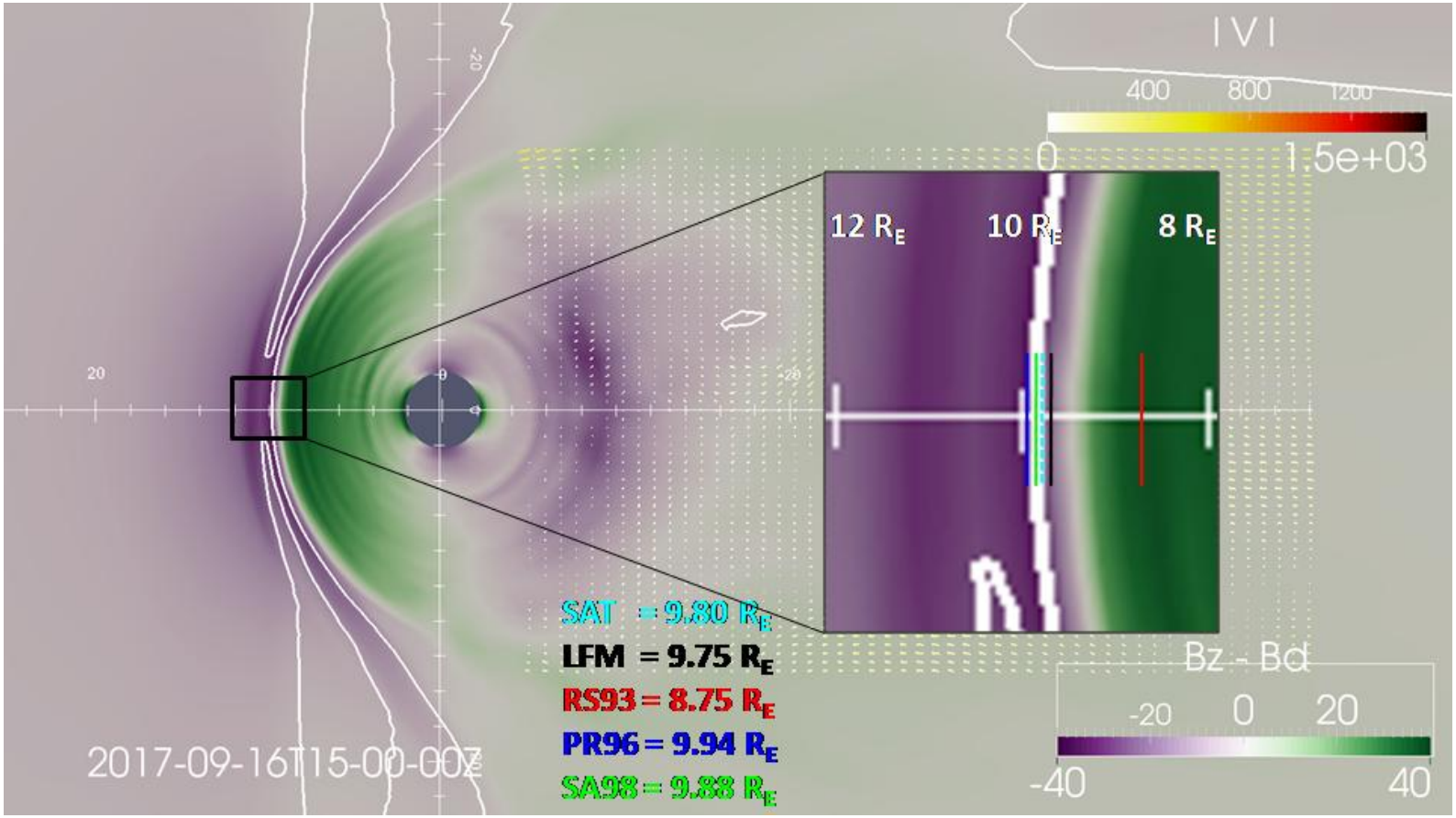

Equatorial plane view for the September 16, 2017 15:00 UT crossing of THEMIS A, in LFM color-coded for Earth's magnetic dipole subtracted from B_Z at that location. The turquoise "SAT" line is the location that THEMIS crosses the magnetopause (X coordinate only). The red, blue, and green lines are the empirical model predictions of the subsolar magnetopause location.

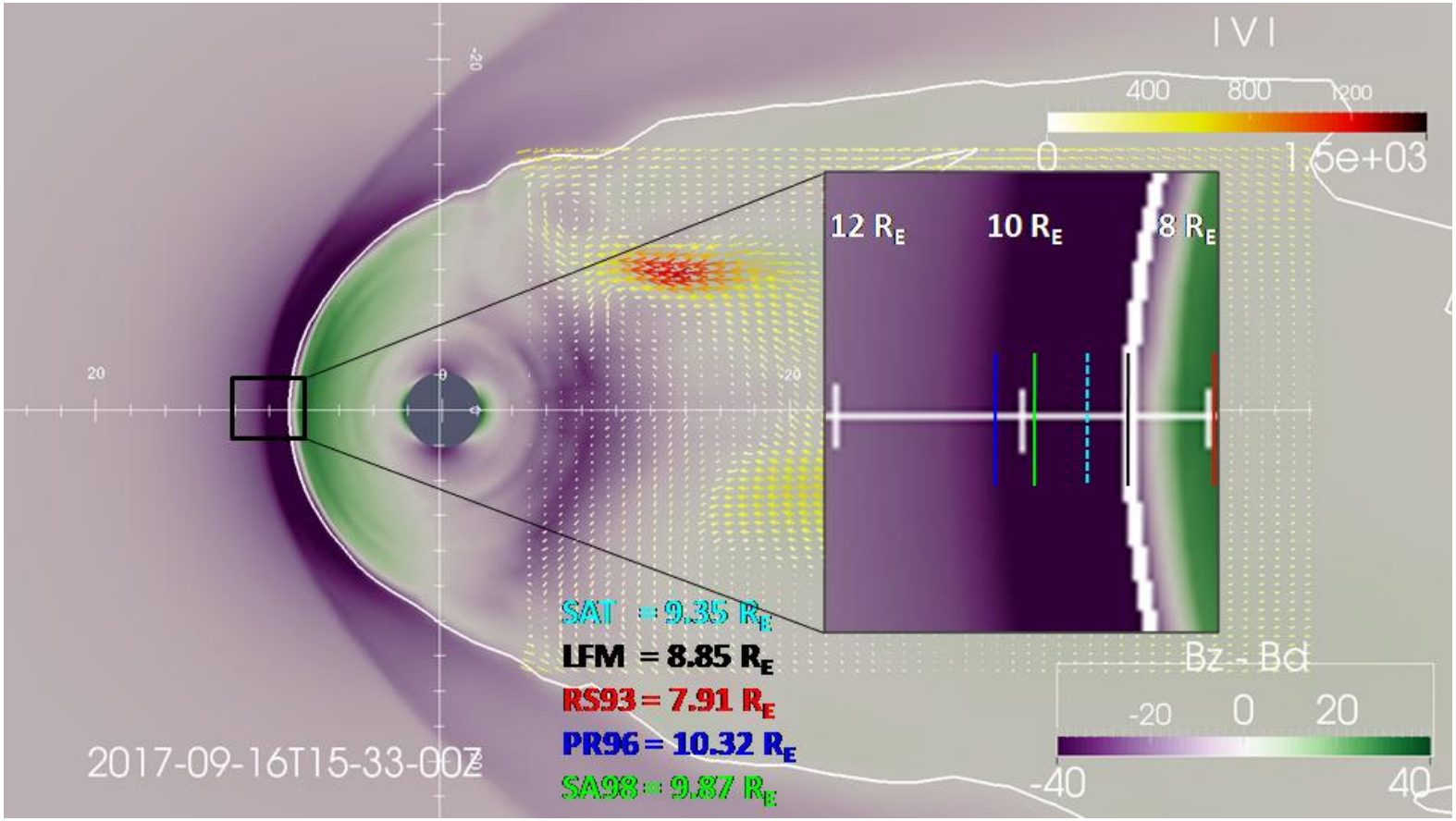

Equatorial plane view for the September 16, 2017 15:33 UT crossing of THEMIS A, in LFM color-coded for Earth's magnetic dipole subtracted from B_Z at that location. The turquoise "SAT" line is the location that THEMIS crosses the magnetopause (X coordinate only). The red, blue, and green lines are the empirical model predictions of the subsolar magnetopause location.

References

Aikio, A.T., and A. Selkälä (2009), Statistical properties of Joule heating rate, electric field, conductances at high latitudes, *Ann. Geophys*., *27*, 2661-2673.

Aksnes, A., O. Amm, J. Stadsnes, N. Ostgaard, G. A. Germany, R. R. Vondrak, and I. Sillanpaa (2005), Ionospheric conductances derived from satellite measurements of auroral UV and X-ray emissions, and ground-based electromagnetic data: a comparison, *Ann. Geophys., 23,* 343-358.

Alfvén, H. (1942), Existence of electromagnetic –hydrodynamic waves, *Nature*, *150*(3805), 405.

Aubry, M. P., C. T. Russell, and M. G. Kivelson (1970), Inward motion of the magnetopause before a substorm, *J. Geophys. Res.*, *75*(34), 7018–7031, doi:10.1029/JA075i034p07018.

Axford, W.I., and C.O. Hines (1961), A unifying theory of high-latitude geophysical phenomena and geomagnetic storms, *Can. J. Phys.*, 39, 1433–1464.

Babcock, H. D. (1959), The Sun's Polar Magnetic Field, *The Astrophysical Journal*, *130*, 364.

Bame, S. J., J.R. Asbridge, W.C. Feldman, and J.T. Gosling (1976), Solar cycle evolution of high-speed solar wind streams, *The Astrophysical Journal*, *207*, 977-980.

Baumjohann, Wolfgang, and Rudolf A. Treumann (1997), *Basic Space Plasma Physics*, Imperial College Press, London.

Bargatze, L.F., D.N. Baker, R.L. McPherron, and E.W. Hones (1985), Magnetospheric impulse response for many levels of geomagnetic activity, *J. Geophys. Res.*, *90*, 6387-6394, doi.org/10.1029/JA090iA07p06387.

Belcher, J. W., and L. Davis Jr. (1971), Large-amplitude Alfvén waves in the interplanetary medium, 2*, J. Geophys. Res., 76*(16), 3534–3563, doi:10.1029/JA076i016p03534.

Bhattarai, S. K., and R. E. Lopez (2013), Reduction of Viscous Potential for Northward Interplanetary Magnetic Field as seen in the LFM Simulation, *J. Geophys. Res. Space Physics, 118,* doi:10.1002/jgra.50368.

Biskamp, Dieter (2003), *Magnetohydrodynamic Turbulence*, Cambridge University Press, Cambridge.

Bonde, R. E. F., R.E. Lopez, and J.Y. Wang (2018), The effect of IMF fluctuations on the subsolar magnetopause position: A study using a global MHD model, *J. Geophys. Res., 123*, doi.org/10.1002/2018JA025203.

Boris, J. P. (1970), A physically motivated solution of the Alfvén problem, No. NRL-MR-2167, Naval Research Lab.

Boyle, C., P. Reiff, and M. Hairston (1997), Empirical polar cap potentials, *J. Geophys. Res.*, *102*(A1), 111 -125, doi:10.1029/96JA01742.

Brandt, P.C., D.G. Mitchell, E.C. Roelof, S.M. Krimigis, C.P. Paranicas, B.H. Mauk, J. Saur, and R. DeMajistre (2005), ENA Imaging: Seeing the Invisible, *Johns Hopkins APL Technical Digest, 26*(2).

Bruntz, R., R. E. Lopez, M. Wiltberger, and J. G. Lyon (2012a), Investigation of the viscous potential using an MHD simulation, *J. Geophys. Res., 117*, A03214, doi:10.1029/2011JA017022.

Bruntz, R., R. E. Lopez, S. K. Bhattarai, K. H. Pham, Y. Deng, Y. Huang, M. Wiltberger, and J. G. Lyon (2012b), Investigating the viscous interaction and its role in generating the ionospheric potential during the Whole Heliosphere Interval, *J. Atmos. Sol. Terr. Phys.*, *83*, 70-78, 10.1016/j.jastp.2012.03.016.

Burch, J.L., T.E. Moore, R.B. Torbert, and B.L. Giles (2016), Magnetospheric multiscale overview and science objectives, *Space Science Reviews*, *199(1-4)*, 5-21, doi:10.1007/s11214-015-0164-9.

Burke, W. J., D. R. Weimer, and N. C. Maynard (1999), Geoeffective interplanetary scale sizes derived from regression analysis of polar cap potentials, *J. Geophys. Res.*, *104*(A5), 9989–9994, doi:10.1029/1999JA900031.

Carlowicz, M., and R. E. Lopez (2002), *Storms from the Sun,* Joseph Henry Press, Washington D.C..

Carrington, R. C. (1859), On certain phenomena in the motions of solar spots, *Monthly Notices of the Royal Astronomical Society*, *19*, 81-84.

Chen, Francis F. (2006), *Introduction to Plasma Physics and Controlled Fusion. Volume 1: Plasma Physics*, Plenum Press, New York.

Claudepierre, S. G., S. R. Elkington, and M. Wiltberger (2008), Solar wind driving of magnetospheric ULF waves: Pulsations driven by velocity shear at the magnetopause*, J. Geophys. Res., 113*, A05218, doi:10.1029/2007JA012890.

Coroniti, F. V., and C. F. Kennel (1972), Changes in magnetospheric configuration during the substorm growth phase, *J. Geophys. Res.*, *77*(19), 3361–3370, doi:10.1029/JA077i019p03361.

Denton, M.H., and J.E. Borovsky (2012), Magnetopause response to high-speed solar wind streams: A comparison of weak and strong driving and the importance of extended periods of fast solar wind, *J. Geophys. Res*., *117,* A00L05, doi:10.1029/2011JA017124.

Dungey, J. W. (1961), Interplanetary magnetic field and the auroral zones, *Phys. Rev. Lett.*, *Vol. 6*, pp. 47-48.

Echer, E., B. Tsurutani, and W. Gonzalez (2011), Extremely low geomagnetic activity during the recent deep solar cycle minimum. *Proceedings of the International Astronomical Union, 7*(S286), 200-209. doi:10.1017/S174392131200484X.

Executive Order No. 13,744 (2016), FR 81(201), 71573-71577.

Fairfield, D. H. (1971), Average and unusual locations of the Earth's magnetopause and bow shock, *J. Geophys. Res.*, *76*(28), 6700–6716, doi:10.1029/JA076i028p06700.

Fedder, J.A., S.P. Slinker, J.G. Lyon, R.D. Elphinstone (1995), Global numerical simulation of the growth phase and the expansion onset for substorm observed by Viking, *J. Geophys. Res.*,*100*(A10), 19083–19093, doi:10.1029/95JA01524.

Fedder, J.A., and J.G. Lyon (1987), The solar wind-magnetosphere-ionosphere current-voltage relationship, *Geophys. Res. Lett.*, *14*(8), 880-883, doi.org/10.1029/GL014i008p00880.

Formisano, V., V. Domingo and K.P. Wenzel (1979), The three-dimensional shape of the magnetopause, *Planetary and Space Science*, *27*(9), 1137-1149.

Freeman, J. W. (2001), *Storms in Space*, Cambridge University Press, Cambridge.

Frey, H. U., T.D. Phan, S.A. Fuselier and S.B. Mende (2003), Continuous magnetic reconnection at Earth's magnetopause, *Nature*, *426*(6966), 533.

Garcia, K. S., V. G. Merkin, and W. J. Hughes (2010), Effects of nightside O^+ outflow on magnetospheric dynamics: Results of multifluid MHD modeling, *J. Geophys. Res.*, 115, A00J09, doi:10.1029/2010JA015730.

Gary, G. A. (2001), Plasma beta above a solar active region: Rethinking the paradigm, *Solar Physics*, *203*(1), 71-86.

Gonzalez, W. D., J. A. Joselyn, Y. Kamide, H. W. Kroehl, G. Rostoker, B. T. Tsurutani, and V. M. Vasyliunas (1994), What is a geomagnetic storm?, *J. Geophys. Res.*, *99*(A4), 5771–5792, doi: 10.1029/93JA02867.

Goodman, M. L. (1995), A three-dimensional, iterative mapping procedure for the implementation of an ionosphere-magnetosphere anisotropic Ohm's law boundary condition in global magnetohydrodynamic simulations, *Ann. Geophys.*, *13*(8), 843-853.

Goodrich, C. C., J.G. Lyon, M. Wiltberger, R.E Lopez, and K. Papadopoulos (1998), An overview of the impact of the January 10–11 1997 magnetic cloud on the magnetosphere via global MHD simulation, *Geophys. Res. Lett., 25*(14), 2537-2540, doi.org/10.1029/98GL01159.

Hain, K. (1987), The partial donor method, *J. Comput. Phys*, *73*, 131.

Hairston, M. R., R. A. Heelis, and F. J. Rich (1998), Analysis of the ionospheric cross polar cap potential drop using DMSP data during the National Space Weather Program study period, *J. Geophys. Res.*, *103*(A11), 26337–26347, doi:10.1029/97JA03241.

Harvey, K. L., and O. R. White (1999), What is solar cycle minimum?, *J. Geophys. Res.*, *104*(A9), 19759–19764, doi: 10.1029/1999JA900211.

Hughes, W.J. (2016), "The Magnetosphere – Structure and Dynamics", Lecture, CISM Summer School, Boulder, Colorado, July 18, 2016.

Jang, M., T.N. Woods, S. Hong, and G.S. Choe (2016), Coronal Dynamic Activities in the Declining Phase of a Solar Cycle, *The Astrophysical Journal Letters*, *833*(1), L11.

Kamide, Y., and A. D. Richmond (1982), Ionospheric conductivity dependence of electric fields and currents estimated from ground magnetic observations, *J. Geophys. Res.*, *87*(A10), 8331–8337, doi:10.1029/JA087iA10p08331.

Kivelson, M. G., C. T. Russell (editors) (1995), *Introduction to Space Physics*, Cambridge University Press, Cambridge.

Krieger, A. S., A.F. Timothy, and E. Roelof (1973), A coronal hole and its identification as the source of a high velocity solar wind stream, *Solar Physics*, *29*(2), 505-525.

Le, G., J. A. Slavin, and R. J. Strangeway (2010), Space Technology 5 observations of the imbalance of regions 1 and 2 field-aligned currents and its implication to the cross-polar cap Pedersen currents, *J. Geophys. Res.*, *115*, A07202, doi: 10.1029/2009JA014979.

Lilensten, J., P. L. Blelly, W. Kofman, and D. Alcayde (1996), Auroral ionospheric conductivities: a comparison between experiment and modeling, and theoretical f10.7-dependent model for EISCAT and ESR, *Ann. Geophys., 14*, 1297-1304.

Lin, R. L., X. X. Zhang, S. Q. Liu, Y. L. Wang, and J. C. Gong (2010), A three-dimensional asymmetric magnetopause model, *J. Geophys. Res.*, *115,* A04207, doi: 10.1029/2009JA014235.

Lopez, R.E., M. Wiltberger, J.G. Lyon, C.C Goodrich, and K. Papadopoulos (1999), MHD simulations of the response of high-latitude potential patterns and polar cap boundaries to sudden southward turnings of the interplanetary magnetic field, *Geophys. Res. Lett., 26* (7), 967–970, doi.org/10.1029/ 1999GL900113.

Lopez, R. E., S. Hernandez, M. Wiltberger, C.L. Huang, E.L. Kepko, H. Spence, C.C. Goodrich, and J.G. Lyon (2007), Predicting magnetopause crossings at geosynchronous orbit during the Halloween storms, *Space Weather*, *5*(1).

Lopez, R. E., R. Bruntz, E. J. Mitchell, M. Wiltberger, J. G. Lyon, and V. G. Merkin (2010), Role of magnetosheath force balance in regulating the dayside reconnection potential, *J. Geophys. Res.*, *115*, A12216, doi:10.1029/2009JA014597.

Lopez, R. E., R. Bruntz, and K. Pham (2014), Linear separation of orthogonal merging component and viscous interactions in solar wind-geospace coupling, *J. Geophys. Res. Space Physics*, *119*, 7566–7576, doi: 10.1002/2014JA020153.

Lu, J. Y., Z.-Q. Liu, K. Kabin, H. Jing, M. X. Zhao, and Y. Wang (2013), The IMF dependence of the magnetopause from global MHD simulations, *J. Geophys. Res. Space Physics*, 118, 3113–3125, doi:10.1002/jgra.50324.

Lyon, J.G., R.E. Lopez, C.C. Goodrich, M. Wiltberger, and K. Papadopoulos (1998), Simulation of the March 9, 1995 substorm: Auroral brightening and the onset of lobe reconnection, *Geophys. Res. Lett., 25*(15), 3039-3042, doi.org/10.1029/98GL00662.

Lyon, J. G., J. A. Fedder, and C. M. Mobarry (2004), The Lyon-Fedder-Mobarry (LFM) global MHD magnetospheric simulation code, *J. Atmos. Sol. Terr. Phys.*, *66*, 1333– 1350, doi:10.1016/j.jastp.2004.03.020.

Maezawa, K. (1974), Dependence of the magnetopause position on the southward interplanetary magnetic field, *Planetary and Space Science*, *22*(10), 1443-1453.

Maltsev, Y. P., and W.B. Lyatsky (1975), Field-aligned currents and erosion of the dayside magnetosphere, *Planetary and Space Science*, *23*(9), 1257-1260.

Maltsev, Y. P., A. A. Arykov, E. G. Belova, B. B. Gvozdevsky, and V. V. Safargaleev (1996), Magnetic flux redistribution in the storm time magnetosphere, *J. Geophys. Res.*, *101*(A4), 7697–7704, doi:10.1029/95JA03709.

Martyn, D.F. (1951), The theory of magnetic storms and auroras, *Nature*, *167*, 92-94.

Masters, A., M. Fujimoto, H. Hasegawa, C. T. Russell, A. J. Coates, and M. K. Dougherty (2014), Can magnetopause reconnection drive Saturn's magnetosphere?, *Geophys. Res. Lett.*, *41*, 1862–1868, doi:10.1002/2014GL059288.

Merkin, V. G., and J. G. Lyon (2010), Effects of the low-latitude ionospheric boundary condition on the global magnetosphere, *J. Geophys. Res.*, *115*, A10202, doi:10.1029/2010JA015461.

Merkine, V. G., K. Papadopoulos, G. Milikh, A. S. Sharma, X. Shao, J. Lyon, and C. Goodrich (2003), Effects of the solar wind electric field and ionospheric conductance on the cross polar cap potential: Results of global MHD modeling, *Geophys. Res. Lett.*, *30*, 2180, doi: 10.1029/2003GL017903, 23.

Models and Regions of Geospace in the Satellite Situation Center Software, V. 2.2 (Hitchhiker's Guide to the SSC Geospace) (n.d.), Retrieved from https://sscweb.gsfc.nasa.gov/users_guide/ssc_reg_doc.html.

National Science and Technology Council (2015a), *National Space Weather Action Plan*, 83 FR, 688.

National Science and Technology Council (2015b), *National Space Weather Strategy*, 80 FR 24296.

Newell, P. T., T. Sotirelis, K. Liou, and F. J. Rich (2008), Pairs of solar wind-magnetosphere coupling functions: Combining a merging term with a viscous term works best, *J. Geophys. Res.*, *113*, A04218, doi:10.1029/2007JA012825.

Palmroth, M., P. Janhunen, T. I. Pulkkinen, and W. K. Peterson (2001), Cusp and magnetopause locations in global MHD simulation, *J. Geophys. Res.*, *106*(A12), 29435–29450, doi:10.1029/2001JA900132.

Parker, E. N. (1958), Interaction of the solar wind with the geomagnetic field. *The Physics of Fluids*, *1*(3), 171-187.

Pembroke, A., F. Toffoletto, S. Sazykin, M. Wiltberger, J. Lyon, V. Merkin, and P. Schmitt (2012), Initial results from a dynamic coupled magnetosphere-ionosphere-ring current model, *J. Geophys. Res.*, *117*, A02211, doi: 10.1029/2011JA016979.

Petrinec, S. M., and C.T. Russell (1993), External and internal influences on the size of the dayside terrestrial magnetosphere. *Geophys. Res. Lett.*, *20*(5), 339-342, doi.org/10.1029/93GL00085.

Petrinec, S. M., and C. T. Russell (1996), Near-Earth magnetotail shape and size as determined from the magnetopause flaring angle, *J. Geophys. Res.*, *101*(A1), 137–152, doi: 10.1029/95JA02834.

Powell, K., P. Roe, T. Linde, T. Gombosi, and D.L. De Zeeuw (1999), A solution-adaptive upwind scheme for ideal magnetohydrodynamics, *J. Comp. Phys., 154*, 284-309.

Raab, W., G. Branduardi-Raymont, C. Wang, L. Dai, E. Donovan, G. Enno, ... and L. Li (2016), SMILE: a joint ESA/CAS mission to investigate the interaction between the solar wind and Earth's magnetosphere, In *Space Telescopes and Instrumentation 2016: Ultraviolet to Gamma Ray* , *9905*, p. 990502, International Society for Optics and Photonics.

Raeder, J., J. Berchem, and M. Ashour-Abdalla (1998), The Geospace Environment Modeling Grand Challenge: Results from a Global Geospace Circulation Model, *J. Geophys. Res.*, 103(A7), 14787–14797, doi: 10.1029/98JA00014.

Raeder, J. (2003), Global magnetohydrodynamics—A tutorial, In *Space Plasma Simulation* (pp. 212-246). Springer, Berlin.

Reiff, P., R. Spiro, and T. Hill (1981), Dependence of Polar Cap Potential Drop on Interplanetary Parameters, *J. Geophys. Res., 86*(A9), 7639-7648, doi:10.1029/JA086iA09p07639.

Ridley, A. J., and E. A. Kihn (2004), Polar cap index comparisons with AMIE cross polar cap potential, electric field, and polar cap area, *Geophys. Res. Lett., 31*, L07801, doi:10.1029/2003GL019113.

Rijnbeek, R. P., S.W. Cowley, D.J. Southwood, and C.T. Russell (2013), Recent Investigations Op Flux Transfer Events Observed at the Dayside Magnetopause. In *Magnetic Reconnection in Space and Laboratory Plasmas*, E. W. Hones (Ed.). doi:10.1029/GM030p0139.

Roelof, E. C., and D. G. Sibeck (1993), Magnetopause shape as a bivariate function of interplanetary magnetic field B_z and solar wind dynamic pressure, *J. Geophys. Res.*, *98*(A12), 21421–21450, doi:10.1029/93JA02362.

Rufenach, C. L., R. F. Martin Jr., and H. H. Sauer (1989), A study of geosynchronous magnetopause crossings, *J. Geophys. Res.*, *94*(A11), 15125–15134, doi: 10.1029/JA094iA11p15125.

Ryden, B. S., and B.M Peterson (2010), *Foundations of Astrophysics*, Addison-Wesley, Boston.

Sheeley, N. R., J.W. Harvey, and W.C. Feldman (1976), Coronal holes, solar wind streams, and recurrent geomagnetic disturbances: 1973–1976, *Solar Physics*, *49*(2), 271-278.

Shepherd, S. G., J. M. Ruohoniemi, and R. A. Greenwald (2003), Testing the Hill model of transpolar potential with Super Dual Auroral Radar Network observations, *Geophys. Res. Lett.*, *30*(1), 1002, doi:10.1029/2002GL015426, 2003.

Shepherd, S. G., and J. M. Ruohoniemi (2000), Electrostatic potential patterns in the high-latitude ionosphere constrained by SuperDARN measurements, *J. Geophys. Res.*, *105*(A10), 23005–23014, doi:10.1029/2000JA000171.

Shepherd, S. G. (2007), Polar cap potential saturation: Observations, theory, and modeling, *J. Atmos. Sol. Terr. Phys*, *69*(3), 234-248.

Shue, J.-H., J. K. Chao, H. C. Fu, C. T. Russell, P. Song, K. K. Khurana, and H. J. Singer (1997), A new functional form to study the solar wind control of the magnetopause size and shape, *J. Geophys. Res.*, *102*(A5), 9497–9511, doi: 10.1029/97JA00196.

Shue, J.-H., P. Song, C.T. Russell. J.T. Steinberg, J.K. Chao, G. Zastenker, O.L. Vaisberg, S. Kokubun, H.J. Singer, T.R. Detman, and H. Kawano (1998), Magnetopause location under extreme solar wind conditions, *J. Geophys. Res.*, *103*(A8), 17691–17700, doi: 10.1029/98JA01103.

Shue, J.-H., P. Song, C. T. Russell, M. F. Thomsen, and S. M. Petrinec (2001), Dependence of magnetopause erosion on southward interplanetary magnetic field, *J. Geophys. Res.*, *106*(A9), 18777–18788, doi: 10.1029/2001JA900039.

Sibeck, D. G., R. E. Lopez, and E. C. Roelof (1991), Solar wind control of the magnetopause shape, location, and motion, *J. Geophys. Res.*, *96*(A4), 5489–5495, doi: 10.1029/90JA02464.

Sibeck, D. G., & Angelopoulos, V. (2008), THEMIS science objectives and mission phases, *Space Science Reviews*, *141*(1-4), 35-59.

Sweetser, T. H., Broschart, S. B., Angelopoulos, V., Whiffen, G. J., Folta, D. C., Chung, M. K., ... & Woodard, M. A. (2011), ARTEMIS mission design, *Space Science Reviews*, *165*(1-4), 27-57.

Tapping, K. F. (2013), The 10.7 cm solar radio flux (F10. 7), *Space Weather*, *11*(7), 394-406.

Tascione, T. F. (2010), *Introduction to the Space Environment*, Krieger Publishing Co., Malabar.

Toffoletto, F., S. Sazykin, R. Spiro, and R. Wolf (2003), Inner magnetospheric modeling with the Rice Convection Model, *Space Science Reviews*, *107*(1-2), 175-196.

Tsurutani, B. T., and W.D Gonzalez (1987), The cause of high-intensity long-duration continuous AE activity (HILDCAAs): Interplanetary Alfvén wave trains, *Planetary and Space Science*, *35*(4), 405-412.

Vasyliunas, V. M. (1970), Mathematical models of magnetospheric convection and its coupling to the ionosphere, In *Particles and Fields in the Magnetosphere* (pp. 60-71). Springer, Dordrecht.

Vasyliunas, V. M. (2001), Electric field and plasma flow: What drives what?, *Geophys. Res. Lett., 28*(11), 2177–2180, doi:10.1029/2001GL013014.

Vickrey, J. F., R. R. Vondrak, and S. J. Matthews (1981), The diurnal and latitudinal variation of auroral zone ionospheric conductivity, *J. Geophys. Res.*, *86*(A1), 65–75, doi: 10.1029/JA086iA01p00065.

Wang, Y., D. G. Sibeck, J. Merka, S. A. Boardsen, H. Karimabadi, T. B. Sipes, J. Šafránková, K. Jelínek, and R. Lin (2013), A new three-dimensional magnetopause model with a support vector regression machine and a large database of multiple spacecraft observations, *J. Geophys. Res. Space Physics*, *118*, 2173–2184, doi: 10.1002/jgra.50226.

Watanabe, M., K. Kabin, G. J. Sofko, R. Rankin, T. I. Gombosi, and A. J. Ridley (2010), pole tilt effects on the magnetosphere-ionosphere convection system during interplanetary magnetic field B_Y-dominated periods: MHD modeling, *J. Geophys. Res., 115*, A07218, doi:10.1029/2009JA014910.

Welling, D. T., V. K. Jordanova, A. Glocer, G. Toth, M. W. Liemohn, and D. R. Weimer (2015), The two-way relationship between ionospheric outflow and the ring

current. *J. Geophys. Res. Space Physics*, *120*, 4338–4353. doi: 10.1002/2015JA021231.

Wiltberger, M., T. Pulkkinen, J. Lyon, and C. Goodrich (2000), MHD simulation of the magnetotail during the December 10, 1996, substorm, *J. Geophys. Res., 105*(A12), 27649-27663, doi:10.1029/1999JA000251.

Wiltberger, M., R. E. Lopez, and J. G. Lyon (2003), Magnetopause erosion: A global view from MHD simulation, *J. Geophys. Res.*, *108*, 1235, doi: 10.1029/2002JA009564, A6.

Wiltberger, M., W. Lotko, J. G. Lyon, P. Damiano, and V. Merkin (2010), Influence of cusp O^+ outflow on magnetotail dynamics in a multifluid MHD model of the magnetosphere, *J. Geophys. Res.*, 115, A00J05, doi: 10.1029/2010JA015579.

Wiltberger, M., L. Qain, C. -L. Huang, W. Wang, R. E. Lopez, A. G. Burns, S. C. Solomon, Y. Deng, Y. Huang (2012), CMIT study of CR2060 and 2068 comparing L1 and MAS solar wind drivers, *J. Atmos. Sol. Terr. Phys.*, *83,* 39-50, doi:10.1016/j.jastp.2012.01.005.

Wiltberger, M. (2016), “Introduction to Magnetohydrodynamic Modeling of the Magnetosphere”, Lecture, CISM Summer School, Boulder, Colorado, July 18, 2016.

Wolf, R. A. (1983) The quasi-static (slow-flow) region of the magnetosphere In *Solar-terrestrial physics* (pp. 303-368), Springer, Dordrecht.

Yee, K. (1966), Numerical solution of initial boundary value problems involving Maxwell's equations in isotropic media, *IEEE Transactions on antennas and propagation*, *14*(3), 302-307.

Biographical Information

Richard E.F. Bonde received three Bachelor of Science degrees in physics (Hons.), mathematics (Hons.), and aerospace engineering from Wichita State University in 2012. He also minored in chemistry. During his time at Wichita State, he worked with Professor Elizabeth Behrman in the area of quantum computing. He completed an honors thesis titled, “Comparisons of Quantum Entanglement Witnesses.” This work was eventually used in the following publication: “On the correction of anomalous phase oscillation in entanglement witnesses using quantum neural networks” in *IEEE Transactions on Neural Networks and Learning Systems*.

Richard started graduate school at the University of Texas at Arlington in 2012 and started working with the high energy physics group. He spent 2015 at CERN working on calibrating the ATLAS experiment’s gap/crack scintillator in the central section of the hadronic tile calorimeter. In 2015, he received a Master of Science degree in physics. In 2016, Richard switched to the space physics group under the supervision of Ramon E. Lopez for his PhD research. During his time here, he was able to work with several undergraduates on their research projects. Richard successfully defended his dissertation and earned a PhD in physics in May 2018.

Richard hopes to earn a postdoc position, preferably still in magnetospheric physics. His interests are to study the magnetospheres of other planets. Eventually, Richard hopes to become a professor of physics.